High Resolution Through-the-Wall and Subsurface Imaging Using Small Number of Transceivers on Moving Robotic Platforms

by

Behzad Yektakhah

A dissertation submitted in partial fulfillment
of the requirements for the degree of
Doctor of Philosophy
(Electrical Engineering)
in the University of Michigan
2019

Doctoral Committee:

Professor Kamal Sarabandi, Chair
Professor Jerome P. Lynch
Professor Amir Mortazawi
Associate Research Scientist Adib Nashashibi

Behzad Yektakhah

byekta@umich.edu

ORCID iD: 0000-0002-4788-2616

To my beloved family

Acknowledgements

I would first like to sincerely thank my research advisor, Professor Kamal Sarabandi, for giving me the opportunity to continue my graduate study at the Radiation Laboratory and his continuous guidance, support, and encouragement throughout my Ph.D.

I would also like to thank my dissertation committee members, Professor Jerome P. Lynch, Professor Amir Mortazawi, and Dr. Adib Nashashibi, for their invaluable feedback on my research.

I would like to acknowledge all faculty members at the Radiation Laboratory, specifically Professor Ehsan Afshari, Professor Anthony Grbic, and Professor Fawwaz Ulaby.

I would like to thank all former and current staff members in Radiation Laboratory.

I would like to sincerely thank all my friends at the University of Michigan, specifically Dr. Fatemeh Akbar, for their invaluable friendship and all the memorable experiences we have made together.

Last but not least, I would like to thank my parents and my brother for their constant love and continuous support.

Table of Contents

Dedication ..... **ii**

Acknowledgements ..... **iii**

List of Figures ..... **viii**

List of Tables ..... **xvi**

List of Appendices ..... **xvii**

Abstract ..... **xviii**

Chapter 1 Introduction **1**

1.1. Background 1

1.2. Motivation and Objectives 4

1.3. Dissertation Overview 7

Chapter 2 All-Directions Through-the-Wall Imaging Using a Small Number of Moving Transceivers **11**

2.1. Introduction 11

2.2. Description of the Proposed Imaging Method 14

2.3. Improving the Image Quality Using Orthogonal Circular Polarizations 20

2.4. Performance Evaluation of the Proposed Imaging Method in Complex Scenarios 27

2.5. Conclusion 30

Chapter 3 Wideband Circularly Polarized Omnidirectional Antenna for All-Directions Through-the-Wall Imaging **32**

3.1. Introduction 32

3.2. Far-Field Electric Field Generated by Excitation of Circular TE_{21} Mode 35

3.3. Excitation of Circular TE_{21} Modes in Free Space for Circular Polarization Operation... 39

3.4. Circularly Polarized Omnidirectional Antenna Using an Array of Eight Monopole SLAs 42

3.5. Wideband Circularly Polarized Omnidirectional Antenna Using an Array of 16 Monopole SLAs 49

3.6. Fabrication and Measurement Results for the 16-Element CP Antenna..... 52

3.7. Conclusion 63

Chapter 4 All-Directions Through-the-Wall Imaging Using a Small Number of Moving Omnidirectional Bi-static FMCW Transceivers..... 65

4.1. Introduction..... 65

4.2. Image Formation Technique Compatible with Bi-Static FMCW Radar Architecture 66

4.2.1. Bi-static FMCW Signal Model and Correction for Errors in Synchronization and Delays in Circuits 66

4.2.2. Image Formation 71

4.3. Bi-static FMCW Radar System Realizing All-Directions Through-the-Wall Imaging73

4.4. Measurement Results 80

4.5. Conclusion 88

Chapter 5 Methods for Imaging Enhancement in Through-the-Wall SAR Imaging..... 90

5.1. Introduction..... 90

5.2. Background Noise Reduction and Range Resolution Enhancement in Through-the-Wall SAR Imaging..... 91

5.3. A Method for Detection of Flat Walls in Through-the-Wall SAR Imaging..... 98

5.3.1. Image of Walls in Through-the-Wall SAR Imaging..... 99

5.3.2. Method for Detection of Walls and Large Flat Surfaces 101

5.3.3. Applying the Proposed Wall Detection Method to the Measured Data..... 106

5.4. Conclusion 108

Chapter 6 High Resolution Imaging of Buried Targets Using Distributed Robotic Sensors 110

6.1. Introduction 110

6.2. Image Formation Technique 112

6.3. Frequency of Operation 114

6.4. Applying the Imaging Method to the Simulated Data 116

6.5. Evaluation of the Imaging Method in a Real Scenario 117

6.6. Conclusion 118

Chapter 7 Low Profile, Low Frequency, UWB Antenna for Imaging of Deeply Buried Targets 120

7.1. Introduction 120

7.2. Antenna Structure 121

7.3. Coupled Modified ENVELOP Antennas 123

7.4. Antenna Fabrication and Measurement Results 125

7.5. Conclusion 133

Chapter 8 Radar System Realizing High Resolution Subsurface Imaging Using Distributed Robotic Sensors 134

8.1. Introduction 134

8.2. Imaging System Employing Multiple Transmitters 135

8.3. Received Signal Model 136

8.4. Evaluation of the System Performance 140

8.5. Conclusion 141

Chapter 9 Conclusion and Recommendations for Future Work 143

9.1. Research Summary 143

9.2. Contributions 144

9.2.1. Development of All-Directions Through-the-Wall Imaging Method 144

9.2.2. Design of a New Wideband Omnidirectional Circularly Polarized Antenna for All-Directions Through-the-Wall Imaging 145

9.2.3. Development of an Image Formation Technique for All-Directions Through-the-Wall Imaging Using Bi-Static FMCW Transceivers 146

9.2.4. Development of a Method for Background Noise Reduction and Range-Resolution Enhancement in Through-the-Wall Imaging 146

9.2.5. Development of a Method for Detection of Walls in High-Resolution Through-the-Wall SAR Imaging 147

9.2.6. Development of a New High Resolution Subsurface Imaging Method Using Small Number of Robotic Transmitters and Receivers 148

9.2.7. Design of a Low Frequency, Low Profile, Wideband Antenna for High Resolution Imaging of Deeply Buried Targets or Targets Buried in Soil with High Losses 148

9.3. Future Work 149

9.3.1. Applying the Method Presented for Detection of Reflecting Points in Through-the-Wall Imaging to Subsurface Imaging 149

9.3.2. Design of a Wideband Circularly Polarized Antenna for Subsurface Imaging Applications 150

9.3.3. Fabrication of the Radar System with Multiple Transmitters and Evaluation of Performance of the Proposed Subsurface Imaging Method in Presence of Different Objects with Different Shapes and Orientations 152

Appendices 154

Bibliography 161

List of Figures

Figure 1.1. Large antenna array mounted on a vehicle for through-the-wall imaging from outside of the building (www.eurekaaerospace.com). 5

Figure 1.2. Through-the-wall imaging using robotic omnidirectional transmitters and receivers [14]..... 6

Figure 1.3. (a) Monostatic transceiver in conventional GPR systems. Buried objects are imaged as parabola. (b) Collecting samples on a uniform grid within the imaging area. 7

Figure 1.4. New subsurface imaging method based on SAR imaging using robotic bi-static transmitters and receivers. 7

Figure 1.5. Overview of the topics that are covered in this dissertation..... 8

Figure 2.1. Transmitter (Tx) and receiver (Rx) arrangement in the proposed method and conventional methods for through-the-wall radar imaging. Dashed lines and x's indicate movement path of receiving robots and sampling points, respectively [13]. 12

Figure 2.2. Geometry of a simple through-the-wall radar imaging problem [13]. 15

Figure 2.3. Normalized PSF calculated using uniform array coefficients for two point targets located at (r, ϕ) = (5 m, 90°) and (5 m, 45°) [13]. (a) Sampling points on a line. (b) Sampling points on a circle. (square is the Tx position, circles represent point targets positions, dots are sampling points positions) 16

Figure 2.4. (a) Projection of sampling points on the line perpendicular to the observation direction to find an's. O denotes the center of the coordinate system [13]. (b) A sample of assigning cosine-squared coefficients to the receivers according to the observation direction. Color of each receiver indicates the value of an (in the range 0−1). 17

Figure 2.5. Normalized PSF calculated for the same configuration as Figure 2.3(b) [13]. (a) Image calculated using cosine-squared coefficients. (b) Multiplication of Figure 2.3(b) and Figure 2.5(a). (square shows the Tx position, circles represent point target positions, dots are sampling points positions)..... 19

Figure 2.6. Unwanted signals received by omnidirectional antennas in all-directions through-the-wall imaging. 21

Figure 2.7. (a) Geometry of the problem where the wall boundary is shown by solid square, Tx position is shown by a small square, target position is shown by a small circle, and sampling points are shown by dots. Also shown is the normalized image (dB) for Tx and Rx antennas with vertical polarization. (b) Normalized image (dB) for Tx and Rx antennas with horizontal polarization. (c) Normalized image (dB) for orthogonal circular polarizations (LHCP for transmitter and RHCP for receiver). (d) Normalized image (dB) for the co-polarized LHCP for transmitter and receiver [13]. 22

Figure 2.8. The same configuration as Figure 2.7 except that the wall permittivity is increased to 6. (a) Normalized image (dB) for Tx and Rx antennas with vertical polarization. (b) Normalized image (dB) for orthogonal circular polarizations (LHCP for transmitter and RHCP for receiver) [13]..... 25

Figure 2.9. The same configuration as Figure 2.7 except that the target is located at (3.0875 m, 90°). (a) Normalized image (dB) for Tx and Rx antennas with vertical polarization. (b) Normalized image (dB) for orthogonal circular polarizations (LHCP for transmitter and RHCP for receiver) [13]..... 25

Figure 2.10. The same configuration as Figure 2.7 except that the homogeneous wall is replaced by a wall with a periodic structure. Relative permittivity of wall is 3. (a) Periodic structure of the wall and normalized image (dB) for Tx and Rx antennas with vertical polarization. (b) Normalized image (dB) for Tx and Rx antennas with horizontal polarization. (c) Normalized image (dB) for orthogonal circular polarizations (LHCP for transmitter and RHCP for receiver) [13]..... 26

Figure 2.11. A large and complex three-dimensional building model for evaluation of the proposed imaging method (the ceiling and the floor are not shown). The dot at the center indicates the location of the transmitter and the three concentric circles indicate the location of receivers (sampling points) [13]. 28

Figure 2.12. Imaging results for the model shown in Figure 2.11 [13]. (a) Image formed by (2.1) with uniform coefficients (only the pixels with image values greater than -20 dB are shown). (b) The image same as (a) except that the image with pixel values greater than -30 dB is shown. (c) The image formed by multiplication of two images calculated separately by applying uniform and cosine-squared array coefficients (only the pixels with the values greater than -30 dB are shown). 29

Figure 3.1. (a) Geometry of the aperture. (b) Electric field distribution of circular TE_{21} mode [16]. 36

Figure 3.2. HFSS simulation result for far-field electric field of an aperture excited by circular TE_{21} mode [16]. 39

Figure 3.3. (a) Topology of SLA. (b) Topology of a monopole SLA element over a circular ground plane [16]. 40

Figure 3.4. Structures for excitation of circular TE_{21} modes and circular polarization and the required excitation amplitudes and phases of the elements [16]. (a) Near-field electric

field due to excitation of one element in an array of four monopole SLAs. (b) Excitation of elements to obtain circular TE_{21} in the near-field of the array. (c) Far-field electric field of the excitation in (b). (d) Structure of the CP antenna formed by eight monopole SLAs and excitation phases and amplitudes for RHCP operation. . 41

Figure 3.5. Simulation result for the maximum of AR at θ = 90° versus frequency for the antenna with eight monopole SLAs [16]. 43

Figure 3.6. Simulation results for RHCP gain at θ = 90° and at 1.28 GHz (solid line), 1.42 GHz (dotted line), and 1.55 GHz (dashed line) [16]. 43

Figure 3.7. Reflection coefficient and total efficiency for the antenna in Figure 3.4(d) [16]..... 44

Figure 3.8. Magnitude (a) and phase (b) of the total coupled signal at different ports of the antenna with eight SLAs. 45

Figure 3.9. Coupling between SLAs. 46

Figure 3.10. Maximum of AR in horizontal plane for different (a) $X = rg = r1 = r2$ + 40 mm, (b) $r1$, and (c) $r3$ [16]. 48

Figure 3.11. Structure of the CP antenna with 16 monopole SLAs. Excitation phases and amplitudes are for RHCP operation. RO4003 dielectric material is indicated by gray color [16]. 49

Figure 3.12. Simulation results for the antenna with 16 monopole SLAs shown in Figure 3.11 (solid lines) and Figure 3.13(b) (dashed lines) [16]. (a) Maximum of AR (dB) and minimum of RHCP gain (dBi) in horizontal plane. (b) Reflection coefficient (dB) and total efficiency. 50

Figure 3.13. (a) Topology of modified monopole SLA. (b) Final structure of wideband CP omnidirectional antenna [16]. 51

Figure 3.14. Reflection coefficient for the antenna in Figure 3.13(b) for different, (a) h and (b) $r6$ [16]..... 52

Figure 3.15. Fabricated CP antenna, the ground plane includes red solder mask [16]..... 53

Figure 3.16. (a) Fabricated feed network (with red solder mask). (b) Block diagram of the feed network. (c) Measurement results for the 45° phase shifter. (d) Measurement results for the fabricated feed network [16]. 55

Figure 3.17. Maximum of AR over horizontal plane among 1000 different runs at (a) 1.3 GHz, (b) 1.7 GHz, and (c) 2 GHz. (d) Histogram plot of maximum of AR over horizontal plane for 1000 runs at 1.7 GHz and for maximum phase difference error of 6° and maximum amplitude error of 0.4 dB..... 57

Figure 3.18. Measured reflection coefficient and total efficiency [16]. 59

Figure 3.19. (a) Average and maximum of the measured and simulated AR over horizontal plane versus frequency [16]. (b) Measured AR in horizontal plane (θ = 90°) (white color indicates AR > 3 dB). 59

Figure 3.20. Measured and simulated average of realized RHCP and LHCP gains over horizontal plane [16]. 60

Figure 3.21. Axial ratio: measured (solid line) and simulated (dashed line without feed network) at θ = 90° and at 1.2 GHz (a), 1.6 GHz (b), and 2 GHz (c). Note that the AR is consistently below 3 dB and dissimilarity between the measured and simulated results are due to the feed network which is not included in the simulations. Also shown at (d) simulated AR at ϕ = 0° and at 1.2 GHz (solid line), 1.6 GHz (dotted line), and 2 GHz (dashed line) [16]. 61

Figure 3.22. Gain pattern: Measured (solid line) and simulated (dashed line without feed network) realized CP gains at θ = 90° and at 1.2 GHz (a), 1.6 GHz (b), and at 2 GHz (c). Also shown are the simulated realized CP gains at ϕ = 0° and at 1.2 GHz (solid line), 1.6 GHz (dotted line), and 2 GHz (dashed line) [16]. 62

Figure 4.1. Transmitter and nth sampling point for image formation at point R [14]..... 67

Figure 4.2. A sample of IF signal before and after correction. Setting reference point A at the transmitter location, the first peak which is due to the signal received from point A (direct signal from the transmitter to the receiver), is shifted to zero frequency in the corrected signal [14]. 72

Figure 4.3. Block diagram of the fabricated radar [14]. (a) Chirp generator and transmitter. (b) Receiver. 74

Figure 4.4. Block diagram of the synchronization circuit at (a) transmitter and (b) receiver [14]. 75

Figure 4.5. Fabricated radar system [14]. (a) Chirp generator/FMCW transmitter. (b) Frequency mixer and synchronization board in receiver. (c) A/D module. (d) Wideband CP and LP antennas. 77

Figure 4.6. Monostatic measurement results inside the anechoic chamber. (a) Metallic sphere (target) inside the chamber. (b) Fabricated radar (FFT of the IF signal). (b) VNA (IFFT of 801 frequency samples over the band 1.2–2 GHz). 78

Figure 4.7. Through-the-wall imaging using the fabricated radar and horn antennas. (a) Transmitting and receiving antennas configuration. (b) Wall and objects behind the wall (metallic sphere and cabinet). (c) Imaging result in presence of sphere. (d) Imaging result while the sphere is removed. 80

Figure 4.8. Range and cross-range resolution performance evaluation of the fabricated system and imaging method [14]. Transmitter is at (x, y) = (0, 0). 180 sampling points are on the white circles. (a) Measurement setup and a metallic pipe as the target. (b)

Measurement setup and a trihedral reflector as the target. (c) Image formed for (a). (d) Image formed for (b). Dashed lines show the range and cross-range directions. Measured image for the pipe and trihedral reflector and simulated image (considering ideal system and point targets at the location of the pipe and trihedral reflector) along the range direction (e) and along the cross-range direction (f) (images are centered at the targets' locations). 82

Figure 4.9. Range and cross-range resolution simulation results considering ideal imaging system and point targets and utilizing 180 sampling points distributed uniformly on a circle with radius of 0.8 m centered at the transmitter location [14]. (a) Range and cross-range resolution versus distance of the point target from the transmitter. The operation bandwidth is 768 MHz. (b) Range and cross-range resolution with respect to the operation bandwidth for a point target at the distance of 2.3 m from the transmitter. The center frequency is at 1.584 GHz. 84

Figure 4.10. (a) Geometry of the fabricated room and objects. (b) Photo of the room and objects. Normalized image (in dB) using LP antennas (c) and CP antennas (d). Transmitter is at (x, y) = (0, 0). Sampling points are on the white circle [14]. 86

Figure 4.11. (a) Walls and target arrangement for the second measurement. (b) Photo of the walls and metallic pipe (target). (c) Normalized image (in dB) using CP antennas. Transmitter is at (x, y) = (0, 0). Sampling points are on the white circle [14]..... 87

Figure 4.12. (a) Measurement setup in a real room. (b) Normalized image (in dB) using CP antennas. Solid lines show the position of sides of walls which are closer to the transmitter. Transmitter is at (x, y) = (0, 0). Sampling points are on the white curve around the transmitter [14]. 88

Figure 5.1. Received time domain signal at the sampling point (r, ϕ) = (2.25 m, 90°) in Figure 2.7(c) and detected centers and amplitudes of the copies of the transmitted signal by GPOF [13]. 93

Figure 5.2. Detection of reflecting points (square represents the transmitter, circles indicate sampling point) [13]. (a) Meshing and initialization of pixels in the imaging area. (b) Possible loci of a reflecting point obtained by a detected delay from a sampling point (solid line is the actual possible loci of the reflecting point and the nearby pixels satisfy the criteria $dm - dp < \delta$). (c) The reflecting point detected by three sampling points. 95

Figure 5.3. (a) The value of pixels (in dB) after applying the imaging method based on GPOF to the same configuration as Figure 2.7(c). (b) The same image as Figure 2.7(c) except that it is calculated only at the pixels in (a) with the values greater than -8 dB. (c) The image after applying the imaging method based on GPOF to the same configuration as Figure 2.8(b). (d) The image after applying the imaging method based on GPOF to the same configuration as Figure 2.10(c) [13]. 97

Figure 5.4. PSF calculated by uniform array coefficients for the same configuration for transmitter and sampling points as Figure 2.3(b), circles indicate the location of point targets. (a) Imaging results for two point targets located at (r, ϕ) = (5 m, 90°) and ((5 m + 0.6ΔR), 90°), SNR = 15 dB. (b) Applying the imaging method based on GPOF for improving the range resolution to the image in (a), SNR = 15 dB. (c) Applying the method for improving the range resolution to the image of two point targets located at (r, ϕ) = (5 m, 90°) and ((5 m + 0.65ΔR), 90°), SNR = 10 dB [13]. 97

Figure 5.5. (a) Image (in dB) calculated using the sampling points located at x>0 in the measurement setup shown in Figure 4.10(a) using CP antennas. (b) Image calculated using the sampling points located at x<0. (c) Image formed using all the sampling points. Sampling points are indicated by white dots [17]. 100

Figure 5.6. Reflection and scattering from a wall surface and a small size object [17]. 101

Figure 5.7. Specular reflections from a flat wall surface in (a) bi-static SAR and (b) monostatic SAR [17]. 102

Figure 5.8. Defining a wall surface and mirroring transmitter with respect to the wall surface for wall detection using specular reflections and back-projection [17]. 103

Figure 5.9. (a) Geometry of the simulated through-the-wall SAR imaging scenario. The wall located at the top is a cinder block wall. (b) Imaging using standard back-projection. (c) Result of applying the wall detection method (solid lines indicate actual walls and dashed lines indicate detected walls) [17]. 105

Figure 5.10. Wall detection result for the measurement setup shown in Figure 4.10. Result of applying the wall detection method to the measured data with 18 dB polarization isolation between transmitter and receiver (CP antennas) (a) and no polarization isolation between transmitter and receiver (LP antennas) (b). Solid lines show real locations of walls and dashed lines show location of the detected walls [17]. 107

Figure 5.11. (a) Measurement setup for monostatic SAR imaging. (b) Image (in dB) obtained by applying back-projection (Sampling points are indicated by gray dots). (c) Result of applying the wall detection method to the measured data. Solid line shows real location of the wall and dashed line shows location of the detected wall [17]. 107

Figure 6.1. Arrangement of transmitter and receiver in the proposed subsurface imaging method. 113

Figure 6.2. Transmission at air-lossy ground interface. 114

Figure 6.3. Attenuation in one-layer soil at depth of 1 m for different values of real and imaginary parts of soil permittivity. (a) At 100 MHz. (b) At 500 MHz. 115

Figure 6.4. Simulation results for two metallic spheres with centers at (0, 0.5 m, -0.9 m) and (0, -0.75 m, -0.9 m). (a) Imaging result (in dB) using one transmitter. (b) Imaging result using four different locations for the transmitter. 116

Figure 6.5. Field measurement. (a) Metallic sphere with diameter of 36 cm buried at the depth of 0.9 m. (b) Imaging result (in dB). (c) Peak to average value of the image in the range -0.5 m $< x <$ 0.5 m and -1 m $< z <$ -0.3 m at y = 0 plane versus real and imaginary part of the soil permittivity. 118

Figure 7.1. Signal penetration depth versus frequency for signal attenuation of 35 dB in wet soil with constant complex permittivity of $16.4-j2.4$. Source is a Hertzian dipole located at the height of 0.2 m above the air-ground interface [18]. 121

Figure 7.2. Modified ENVELOP antenna structure (optimized for maximum -10 dB impedance bandwidth) [18]. The exponential tapered section is approximated by 10 linear sections with equal lengths along y. 122

Figure 7.3. Simulation results for the antenna in Figure 7.2 (solid line) and Figure 7.4 (dotted line) [18]. (a) Reflection coefficient (dB). (b) Realized gain (dBi) in yz-plane at 300 MHz. 124

Figure 7.4. Coupled modified ENVELOP antennas [18]. 124

Figure 7.5. Reflection coefficient and realized gain (at θ = 0°) for the antenna in Figure 7.4 for different values of (a) Bx, (b) Bz, (c) L, (d) H, (e) W, (f) Cx, (g) s, and (h) g [18]. 126

Figure 7.6. (a) CAD model of the final antenna and the feed, RO4003 dielectric materials is indicated by gray color. (b) Fabricated antenna [18]. 128

Figure 7.7. (a) Simulation and measurement results for the antenna in free space. (b) Antenna placed on wet soil covered by sand for reflection coefficient measurements. (c) Measurement results for the antenna placed on the ground [18]. 129

Figure 7.8. Simulated and measured realized gain of the fabricated antenna [18]. 130

Figure 7.9. Measured and simulated realized gain pattern (dBi) in xz and yz-planes at (a) 200 MHz, (b) 300 MHz, and (b) 400 MHz (solid line: measured in free space, dotted line: simulated for the antenna placed at the height of 10 cm from dry soil) [18]. 130

Figure 7.10. Evaluation of performance of the antenna in a GPR application [18]. (a) Configuration of the antennas and buried metallic plate in wet soil. (b) Imaging result (time delay is shifted such that the delay for the direct signal is zero) for all positions along the scan direction. (c) Image at the location of the plate along the dashed line shown in (b). (d) Ray-tracing result for different signals received at the receiver. 132

Figure 8.1. Block diagram of the imaging system with N transmitters. 136

Figure 8.2. Flow chart of the error correction and image formation using an imaging system with N transmitters and M frequency steps. 139

Figure 8.3. A sample of signal at the receiver input (no noise) in a system with 4 transmitters. (a) Signal in time domain. (b) Signal in frequency domain. (c) Actual and retrieved phases and amplitudes of signals due to each transmitter. 140

Figure 8.4. A sample of signal at the receiver input (SNR = 3 dB, noise power is measured in the range 149−154 MHz) in a system with 4 transmitters. (a) Signal in time domain. (b) Signal in frequency domain. (c) Actual and retrieved phases and amplitudes of signals due to each transmitter. 141

Figure 9.1. Wideband polarization-reconfigurable antenna with directive radiation pattern. (a) Excitation for CP operation. (b) Excitation for LP operation (green arrows show the generated linear polarized electric fields and blue arrows show the excited currents). 151

Figure 9.2. Reflection coefficient of the antenna in Figure 9.1 for CP and LP operation. 152

Figure 9.3. Simulated gain for LP operation (a) and CP operation (b) (black line is the gain for the excited polarization and the red line is the gain for cross-polarization)..... 152

Figure 9.4. Co- (red line) and cross-polarization (black line) gain radiation pattern (in dBi) at 1.6 GHz for the antenna in Figure 9.1 for CP operation (a) and LP operation (b). 152

List of Tables

Table 2.1. Comparison of the proposed method and conventional methods for through-the-wall radar imaging 13

Table 3.1. Performance comparison of wideband CP omnidirectional antennas. 63

Table 4.1. Phase noise of the fabricated radar 74

List of Appendices

Appendix A: MATLAB Code for All-Directions Through-the-Wall Imaging Using Bi-Static FMCW Transceivers 155

Appendix B: MATLAB Code for Detection of Walls and Large Flat Surfaces in Through-the-Wall Imaging Using Bi-Static FMCW Transceivers..... 159

Abstract

Imaging of visually obscured objects within buildings or buried under ground using low frequency EM waves have many military, security, civilian, and industrial applications. In imaging systems, range and cross-range resolution are important parameters that determine the ability of the system to resolve closely spaced objects. Range resolution generally depends on the signal bandwidth while the cross-range resolution depends on the antenna aperture size. In certain application such as through-the-wall imaging and detection of buried land mines and pipelines where the objects are closely spaced and/or located at far distance from the transmitter and receiver, the imaging system must have high cross-range resolution. Typically, this is achieved by using a large array of directive antennas with limited field of view and low mobility.

In this research, new imaging methods based on synthetic aperture processing are presented to address low cross-range resolution, limited field of view, and low mobility of currently available imaging systems. For through-the-wall imaging applications, the large array of directive antennas used in current systems is replaced by a small number of omnidirectional transceivers mounted on moving robots. One or more receivers move and sample the scattered signal at different locations within the imaging area. By applying back-projection technique to the obtained samples, a large 2-D array is synthesized for high resolution imaging. Using omnidirectional antennas, images with a 360° field of view are generated in a short period of time.

To suppress the effect of direct coupling between the transmitter and receiver and multiple reflections in the image, orthogonal circular polarizations are used for the transmitting and receiving antennas. In this research, a novel wideband circularly polarized omnidirectional antenna is presented for through-the-wall imaging applications. The antenna operates based on excitation of orthogonal field distributions similar to a circular waveguide TE_{21} mode.

A bi-static FMCW radar system realizing the presented through-the-wall imaging method is designed and fabricated. The system is configured to account and completely compensate for the delays inherent to the circuits and errors in transmitter/receiver synchronization completely. Performance of the method is evaluated in different real-world scenarios using the fabricated radar system and the associated algorithms.

Two new methods for image enhancement in through-the-wall imaging are developed. The first method enhances the range resolution and reduces the background noise in the image by detecting the locations of the reflections and forming the image only at those points. The second method discriminates wall surfaces from small size objects and detects the location and orientation of all wall surfaces within the imaging area.

The second part of the dissertation describes a new method for subsurface imaging using the general idea developed for the through-the-wall imaging. The method utilizes bi-static ground looking transmitters and receivers mounted on moving robots to sample scattered fields at different locations. The samples are processed coherently to form a large 2-D synthetic array which provides high cross-range resolution 3-D images of the subsurface in a short period of time. This cannot be achieved using conventional ground penetrating radars.

A new low profile wideband antenna is designed for the imaging of deeply buried targets or targets buried in soil with high losses. Performance of the designed antenna and the proposed

imaging method have been tested through field measurements. The imaging results show high resolution 3-D imaging capability of the method.

Chapter 1 Introduction

1.1. Background

Detection and localization of visually obscured targets either hidden behind walls or buried underground has many military, security, civilian, and industrial applications. The target may be an underground tunnel, a buried land mine or pipe, or human subjects inside a building. Most materials are a heterogenous mixture of particles densely packed and when the scale of the heterogeneity is comparable or larger than a wavelength, the constituent particles scatter the incident wave in different directions and absorb the wave. In this case, the material appears opaque to the incident wave. For example, the majority of manmade or natural materials are opaque in the visible part of the electromagnetic (EM) spectrum and as a result, the human eye, as a visible light sensor, cannot see through them. In contrast to visible light spectrum, EM waves with frequency up to 2 GHz can efficiently penetrate through construction materials and into the ground with different soil types since the wavelength is much larger than the scale of constituent particles of most materials. In this band of spectrum, the attenuation is mainly dominated by the imaginary part of the effective dielectric constant of the materials and not due to scattering loss. Hence, these waves can provide information about visually hidden objects, albeit different phenomena including propagation loss, reflection, and scattering from other large inhomogeneities can complicate detection and localization.

Ground penetrating radar (GPR) is the current technology that employs EM waves for the detection of underground features (e.g. underground tunnels, archeological sites, and soil and ice

layers) and buried targets (e.g. land mines, cables, and pipelines). GPR has widespread use in infrastructure development, mining, town planning, archaeology, construction, industry, and ecology. Using EM waves to detect subsurface features dates back to the 1950s, when radio echo sounding systems were utilized to investigate ice sheets. Later, the application was extended to the investigation of soil and rock and coal mine exploration in the 1960s [1], [2]. In the early 1970s, NASA employed a pulsed radar in Apollo 17 to investigate the moon surface from orbit. Between 1980 and 1985, GPR systems for applications other than geological survey such as road investigation and utility mapping were developed. In the late 1990s, the rapid development of computer systems enabled 3D EM numerical simulations for better understanding of wave propagation and interaction in ground media. In addition, digital data acquisition, higher processing power, and 3D visualization capability of new computer systems enabled the advent of 3D GPR systems. Now, GPR is a well-developed technology and a powerful nondestructive investigation tool that is widely used by scientists and engineers [3]. Current research on GPR systems are focused on signal processing, target classification, and the application of GPR in various fields including sedimentology, hydrology, glaciology, and civil engineering [4].

Detection and localization of visually obscured targets hidden behind walls is a relatively new and challenging topic in remote sensing encompassing different research topics including forward and inverse problems, wave propagation in complex media, signal processing, and radar technology. Through-the-wall imaging and sensing is an extension of GPR applications to inspect buildings and targets (e.g. people and objects) inside [5]. However, there are major differences between GPR and through-the-wall imaging systems. In GPR systems, the volume under investigation is embedded in the ground (propagation medium) and the only significant discontinuity is the air-ground interface. In through-the-wall imaging and sensing, the propagation

medium is a combination of air, walls, and building interior that introduce multiple discontinuities (air-material interface) resulting in the appearance of spurious targets. In GPR, the sensors are placed very closed to the ground for efficient coupling of power to the ground. In through-the-wall imaging, it is not necessary to place sensors close to the wall providing great flexibility in the placing of sensors. Due to the large attenuation of EM waves in the ground, GPR systems usually operate at frequencies less than 1 GHz. In through-the-wall imaging and sensing, wave attenuation only happens in the construction materials and, as a result, the frequency of operation can be increased up to 2 GHz to increase the operational bandwidth and to enhance the imaging resolution.

Systems realizing through-the-wall imaging and sensing were presented in the late 1990s [6]–[8]. Application of through-the-wall imaging and sensing falls within two major categories:

1. Through-the-wall imaging: In this application, the building interior and objects hidden inside the buildings are imaged. The radar systems are ultra-wideband (UWB) systems that resolve targets inside and utilize beam-forming techniques along with a large 1-D or 2-D real or synthetic aperture to provide 1-D or 2-D angular resolution resulting in 2-D [9] or 3-D images [10], respectively. In these systems, the range and cross-range resolution are inversely proportional to the transmitted signal bandwidth and antenna aperture (real or synthetic) size, respectively;
2. Through-the-wall motion detection and sensing: In this application, sensors are utilized to detect any motion inside the area under investigation (e.g. a room) from behind the walls. The motion detection includes breath detection that has many applications in surveillance and rescue operations [11]. The systems realizing this application are continuous wave (CW) Doppler radars or UWB radars with high range resolution [12]. The system may employ spatial beam-forming to resolve different sources of motion.

1.2. Motivation and Objectives

Radars considered for through-the-wall imaging applications make use of UWB signal waveforms that typically fall in the frequency range 0.5–2 GHz to provide the required range resolution. This frequency band is low enough to allow for signal penetration through typical walls and high enough to allow for physically small and efficient antennas for the system. To obtain high cross-range resolution, a large aperture must be formed. To achieve this, two different approaches may be pursued: 1) using a large array of transmitting and receiving antennas (real aperture) and 2) using a moving transmitter and receiver pair to realize a large synthetic aperture. To achieve a fine spatial resolution, the use of large real aperture antennas is impractical, especially inside the buildings, due to low mobility. Also, performance of the standard drive by synthetic aperture systems are limited due to the limited field of view of such systems. Systems for mapping buildings from outside (Figure 1.1) can usually provide an image of the first floor of the building and their imaging capability decreases as the complexity of the buildings' interiors increase. The directional antennas that are used in both approaches provide only an image of the area in front of the antennas and therefore current imaging systems require multiple scans from different directions, if possible, to provide a 360° view of the buildings' interiors [13].

In this dissertation, a new approach for through-the-wall radar imaging from within buildings is proposed. The method provides high resolution images while maintaining high mobility for the system within confined space. In addition, the method provides a complete view of the building interior in a short period of time. In the new approach, an array of directive antennas is replaced by one transmitting and at least one receiving omnidirectional antenna mounted on robots, as shown in Figure 1.2. The transmitting robot sends signals in all directions and the

Figure 1.1. Large antenna array mounted on a vehicle for through-the-wall imaging from outside of the building (www.eurekaaerospace.com).

receiving robots move inside the room and sample the reflected signal from the building's interiors and hidden objects at different positions. By applying an appropriate beam-forming technique to the received signals, a large and dense 2-D array with a full 360° field of view can be synthesized resulting in a very high cross-range resolution for the image and high processing gain. This new idea in through-the-wall imaging can be extended to the application of subsurface imaging to propose a high lateral (cross-range) resolution subsurface imaging method and system.

Current systems for subsurface imaging are based on GPR. GPR systems utilize a monostatic transceiver (Figure 1.3(a)), to acquire data in a uniform grid of sampling points within the imaging area [15], as shown in Figure 1.3(b). However, not all these points provide independent information about the subsurface environment and they are not processed coherently. As a result, imaging using GPR systems is slow and does not provide enough lateral resolution for many applications including detection of deeply buried targets such as pipelines. As a result of low lateral resolution of GPR systems, a buried object is imaged as a parabola larger than the object size as shown in Figure 1.3(a). Large antenna arrays with a narrow beam can be utilized to enhance lateral resolution. However, the low frequency of operation of GPR systems requires large size antenna arrays which in turn limit system mobility.

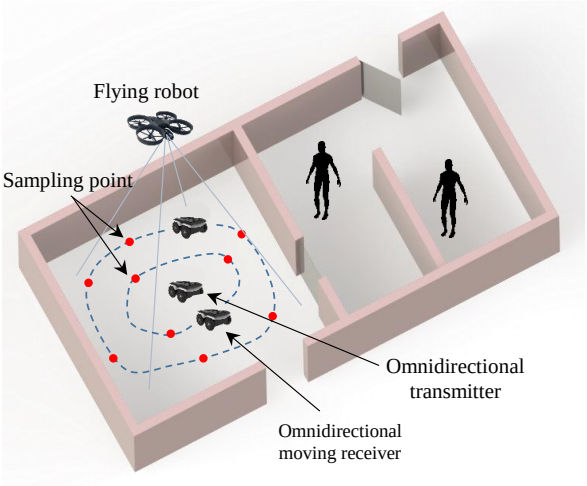

Figure 1.2. Through-the-wall imaging using robotic omnidirectional transmitters and receivers [14].

To address time-consuming data collection process, low lateral resolution, and low mobility in GPR systems, a new subsurface imaging technique based on synthetic aperture (SAR) processing is introduced in this dissertation. In the new method, SAR processing is applied to a limited number of scattered signal samples to form a large 2-D synthetic aperture that provides high resolution 3-D images of subsurface features and buried objects. The method requires at least a pair of a stationary transmitter and a moving receiver equipped with wide beamwidth antennas and arranged in a bi-static configuration to sample scattered fields near the ground as shown in Figure 1.4. Measurement and simulation results show that the obtained samples on a circle are enough for subsurface image formation within the entire circular area. This eliminates the need for sampling on a grid and makes the data collection and imaging formation fast. In addition, eliminating the need for employing large antennas enhances the system mobility, and as a result the transmitter and receivers can be mounted on ground robots or drones for autonomous data collection (specifically in hazardous areas such as mine fields).

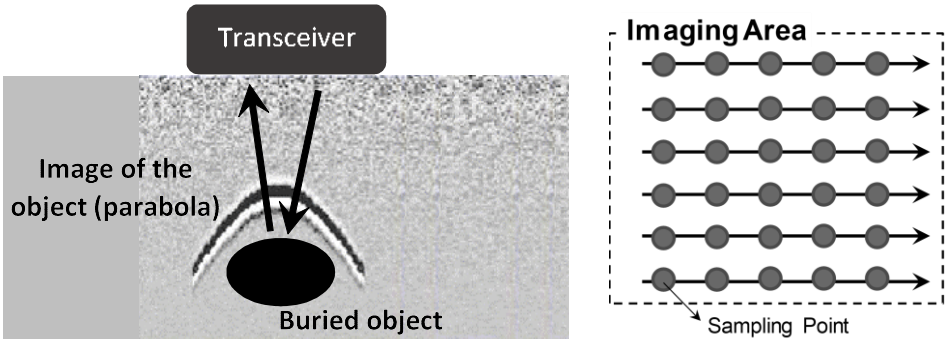

(a) (b)

Figure 1.3. (a) Monostatic transceiver in conventional GPR systems. Buried objects are imaged as parabola. (b) Collecting samples on a uniform grid within the imaging area.

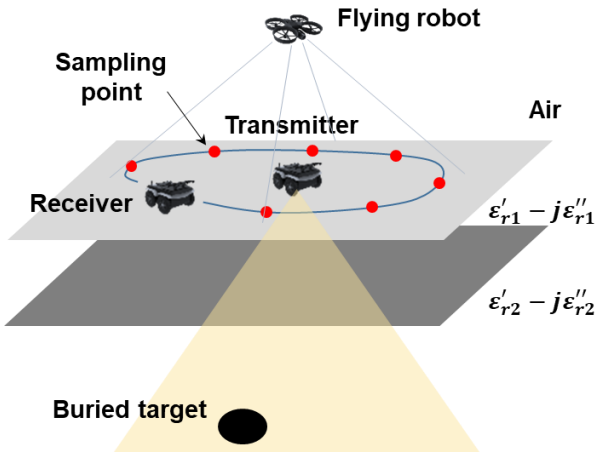

Figure 1.4. New subsurface imaging method based on SAR imaging using robotic bi-static transmitters and receivers.

1.3. Dissertation Overview

Figure 1.5 shows an overview of the topics that are covered in this dissertation. This dissertation consists of 9 chapters. In Chapter 2, all-directions through-the-wall imaging method in introduced. The new method employs small number of omnidirectional transmitters and receivers mounted on small robots to sample scattered fields within the imaging area. Based on SAR processing, it provides 360° view of the imaging area with a high resolution in a short period of time. The method utilizes orthogonal circular polarizations for wideband omnidirectional antennas in transmitter and receiver to reduce the effect of the direct signal from transmitter and the scattered signals experiencing double reflections. Performance of the imaging method is evaluated through simulations of different scenarios both simple and complex [13].

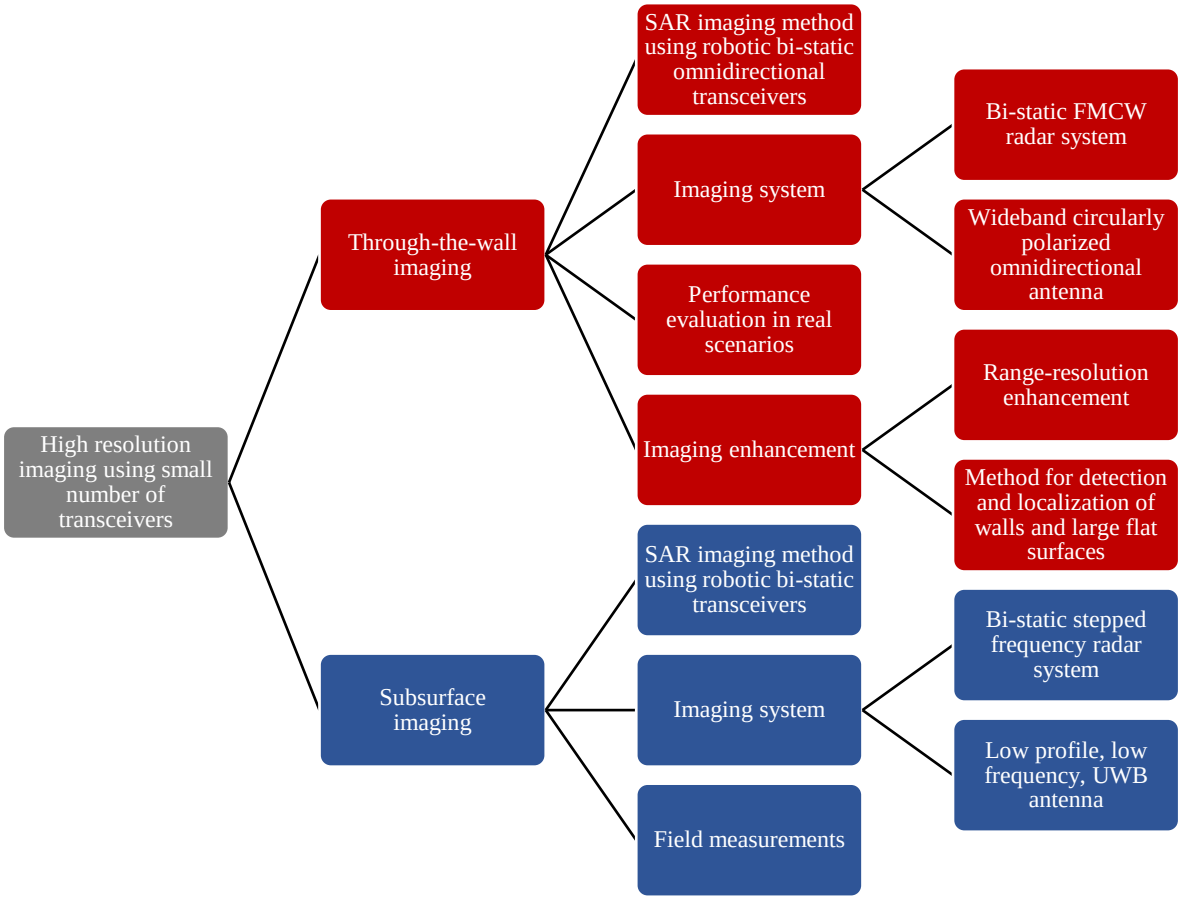

Figure 1.5. Overview of the topics that are covered in this dissertation.

Implementation of a radar system realizing all-directions through-the-wall imaging is discussed in Chapter 3 and 4. In Chapter 3, a novel wideband circularly polarized omnidirectional antenna is introduced to realize the antennas required for all-directions through-the-wall imaging [16]. In Chapter 4, a radar system is developed to realize all-directions through-the-wall imaging. Although the imaging method introduced in Chapter 2 is based on the stepped frequency continuous wave (SFCW) radar architecture, in Chapter 4, a radar system is designed based on a frequency modulated continuous wave (FMCW) radar architecture which makes the synchronization process of bi-static transmitter and receivers simpler. In this chapter, the image formation technique is modified based on the new radar architecture. The new technique takes into account and compensates for synchronization errors and deterministic and random delays in the

circuits. Performance of the imaging method and system is evaluated through different laboratory and field measurements [14].

In Chapter 5, two methods for imaging enhancement in through-the-wall SAR imaging are introduced. The first method is based on spectral analyses and enhances the range resolution in through-the-wall SAR imaging. The method is applicable to the data obtained by a stepped frequency radar. Performance of the method is evaluated through simulations [13].

Unlike point targets, walls and large flat surfaces that are extended along a plane do not present single phase center. As a result, in high cross-range resolution SAR systems where a large aperture is used for image formation, walls are imaged as a few discrete points instead of a solid line. In this case, without prior knowledge about the presence of the walls, they may be interpreted as discrete closely separated objects. In Chapter 5, a simple and effective method is proposed to discriminate walls and large flat surfaces from small size objects. The method detects the location and orientation of the walls and is applicable to both monostatic and bi-static scenarios [17].

In Chapter 6, a new subsurface imaging technique based on SAR processing is introduced to address the time-consuming data collection process, low lateral resolution, and low mobility of conventional GPR systems. The method utilizes distributed bi-static transmitters and receivers mounted on high-mobility robots or drones to sample the scattered fields from the subsurface features and buried targets and form a large 2-D synthetic aperture for high resolution 3-D imaging. Performance of the proposed imaging technique is evaluated through numerical simulations and a field measurement. According to numerical simulations, using multiple transmitters or one transmitter at different locations reduces the spurious images and improves the subsurface image contrast.

In subsurface imaging systems, obtaining high range resolution images requires a wide operation bandwidth for the system and the antennas. The center frequency of operation can be increased to simplify the design of wideband systems and reduce physical size of the antennas. However, for deeply buried targets, increasing the frequency of operation will adversely affect detection because of high signal attenuation of high frequency signals in soil. In subsurface imaging systems, wideband operation at low frequencies and constraints on the size and weight of the antennas for mobility, make the antenna design a challenge specifically for subsurface imaging systems intended for imaging of deeply buried targets. In Chapter 7, a low profile UWB antenna operating at frequencies below 500 MHz is introduced that can be utilized for high resolution subsurface imaging systems for detection of deeply buried targets or target buried in soil with high losses. The antenna performance is evaluated through a field measurement on wet and dense soil with high losses [18].

In Chapter 8, a bi-static imaging system employing multiple transmitters is introduced. To reduce the time required for data collection, the idea of orthogonal frequency division multiplexing (OFDM) is used in the system to separate signals received from different transmitters while all the transmitters are operating simultaneously. Performance of the system including its noise performance is evaluated through numerical simulations. A method for correction of errors in synchronization of bi-static transceivers is also introduced.

Chapter 9 provides conclusion and recommendations for future work.

Chapter 2 All-Directions Through-the-Wall Imaging Using a Small Number of Moving Transceivers

2.1. Introduction

Trough-the-wall radar imaging using EM waves are intended for mapping buildings' interiors and detecting static and moving objects hidden behind walls and other optically opaque obstacles [19]–[24]. This capability has found many applications in rescue, military, and law enforcement operations. Several techniques have been devised for through-the-wall imaging including synthetic aperture radar (SAR) imaging [25]–[29], linear inversion [30]–[32], high resolution imaging using spectral methods [33], and compressed sensing [34], [35]. To enhance the image quality of such mapping systems, techniques for enhancing cross-range resolution, methods for compensating the effect of walls, and several techniques for beam-forming and synthetic aperture formation have been proposed [29], [36]–[38]. However, the quality and applicability of the proposed methods have not yet met the desired specifications. Also the localization and classification of hidden objects still require further research [39].

As illustrated in Figure 2.1, current high resolution imaging systems utilize large arrays of directive antennas to form a large real aperture, thereby providing images with high cross-range resolution [40]. However, the requirements for the cost and mobility of the array impose limitations on the size of the array and achievable resolution. In current imaging systems, directional antennas limit the field of view, and as a result, multiple scans from different directions are required to form a complete image of building's interiors. In practical systems, the large

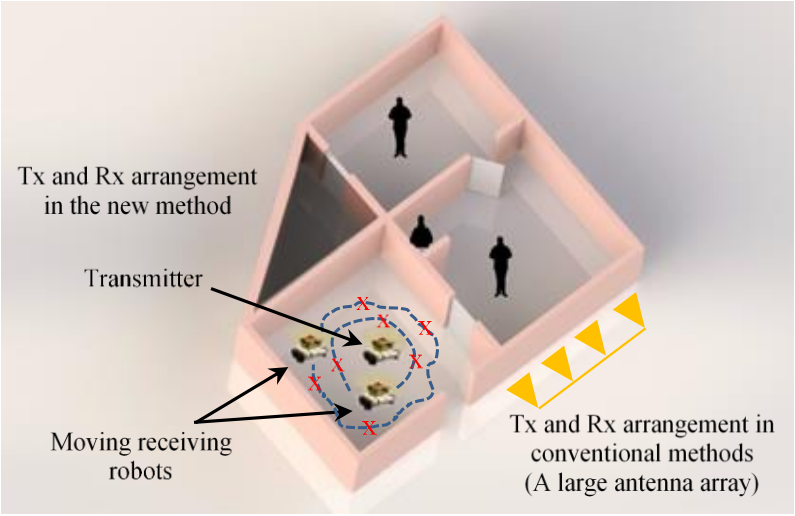

Figure 2.1. Transmitter (Tx) and receiver (Rx) arrangement in the proposed method and conventional methods for through-the-wall radar imaging. Dashed lines and x's indicate movement path of receiving robots and sampling points, respectively [13].

antenna array is mounted on a vehicle and as a result the imaging is performed from outside of the building and is limited to the first floor as shown in Figure 1.1. The imaging capability of such systems decreases as the complexity of the buildings' interiors increases.

In this chapter, a new approach for through-the-wall radar imaging from within buildings is proposed. The proposed method allows for improved mobility within confined space without increasing complexity and provides a complete view of the building interiors in a short period of time. The main idea is to replace the array of directive antennas moved on a linear path with a limited number of small moving robotic transceivers with omnidirectional antennas as illustrated in Figure 2.1. In this method, one robot acts as transmitter and the rest act as receivers. Receiving robots move inside the room and sample the reflected signal from the building's interiors and hidden objects at different positions (sampling points). Utilizing multiple receiving robots enables obtaining a large number of samples in a short time. Using omnidirectional transmitting and receiving antennas and applying an appropriate beam-forming technique to the received signals, a large and dense 2-D array can be synthesized to form a 360° view of the imaging area with a very high cross-range resolution and high processing gain.

Table 2.1. Comparison of the proposed method and conventional methods for through-the-wall radar imaging

Proposed Method	Conventional Methods
Utilizes a limited number of moving transceivers to create a 2-D large synthetic aperture	Utilizing a large array of directional antennas
High mobility	Low mobility
Provides a 360° view of the imaging area using omnidirectional antennas	Directional antennas only provide an image of the area in front of the array
Performs imaging from the inside of the buildings	Imaging is performed from the outside of the buildings and limited to the first floor
Imaging is fast.	Require multiple number of scans in different directions to provide a complete image of the building
The imaging capability is not significantly affected by the complexity of the buildings' interiors	Complexity of the buildings' interiors adversely affects the imaging capability of the system
Bi-static transmitter and receiver must be synchronized.	No synchronization is required.
The effect of multiple reflections is higher in the image.	Directive antennas reduce the effect of multiple reflections on the final image.

Table 2.1 presents a comparison of the proposed method and conventional methods for through-the-wall radar imaging.

With omnidirectional antennas, receivers are exposed to direct transmitter illumination that is relatively high compared to the reflected and scattered signals from the surrounding environment. This relatively high-power direct signal can reduce the receiver sensitivity and mask low power received signals from weak scatterers. In addition, with omnidirectional antennas, receivers will collect multiple interactions of the transmitted signal with building's interiors (specifically double reflections from the corners and multiple reflections from parallel walls) from all directions. This results in appearance of spurious images and substantial increase in the background noise in the final image. To reduce the adverse effects of employing omnidirectional antennas, two orthogonal polarizations for transmitting (Tx) and receiving (Rx) antennas are proposed. With this technique, the level of the direct signal from transmitter and signals that experience even number of reflections are reduced by a factor equal to the polarization isolation between the transmitting and receiving antennas.

2.2. Description of the Proposed Imaging Method

Figure 2.2 shows the geometry of a simple through-the-wall radar imaging problem and configuration of transmitter and receivers according to the proposed method. According to Figure 2.2, one stationary transmitter and one or more moving receivers are placed within a room with dielectric walls. Utilizing omnidirectional antennas, the transmitter sends a signal in all directions. Receivers move inside the room and sample the reflected signal from the building's walls and hidden objects as well as the direct signal from the transmitter at different positions. Sampling the signal at a rate proportional to the maximum speed of the rovers, a large number of samples with a prespecified spatial intervals are collected. Each sampling spot corresponds to an antenna element of a large synthetic array. To determine the relative locations of the transmitter and moving receivers, a LIDAR mounted on the transmitting robot or a flying robot equipped with a high resolution camera and perched at a location that can view the scene is used. Applying an appropriate beam-forming technique to the samples of the received signal, a 360° view of the imaging area can be obtained with a high cross-range resolution.

To form the image, the standard back-projection (back-propagation) technique is applied to the samples of the received signal. Considering N_f frequency samples and N_s sampling points, the image at position $\bar{r}$ (denoted by $S(\bar{r})$) is calculated by

$$S(\bar{r}) = \frac{1}{N_f N_s} \sum_{m=1}^{N_f} \sum_{n=1}^{N_s} a_n S_{mn}^r R_{tp} R_{pn} e^{jk_m(R_{tp}+R_{pn})} \tag{2.1}$$

where, S_{mn}^r is the received signal at mth frequency sample and nth sampling point, R_{tp} is the distance between the transmitter and the imaging point at position $\bar{r}$, R_{pn} is the distance between the imaging point at position $\bar{r}$ and nth sampling point (Figure 2.2), and k_m is the free space

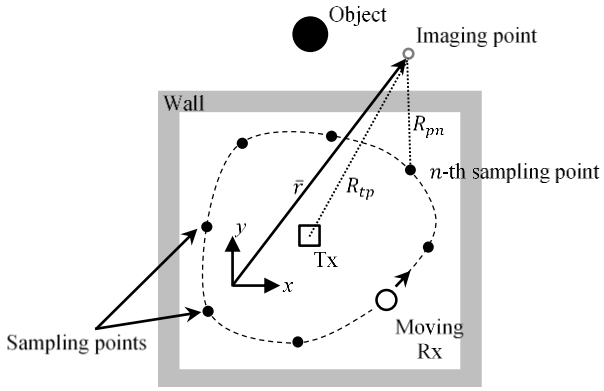

Figure 2.2. Geometry of a simple through-the-wall radar imaging problem [13].

propagation constant at mth frequency. a_n is the array weight factor for beam-forming. It is noted that in (2-1), a time dependence of $e^{j\omega t}$ is assumed.

In the proposed method, the sampling points locations must be carefully chosen to avoid ambiguity in the detection of objects' positions and to maintain a uniform cross-range resolution in all directions. Figure 2.3(a) shows an arrangement of sampling points on a line and the resulting point spread function (PSF) calculated by (2.1) with a_n = 1 for two point targets located at (r, ϕ) = (5 m, 90°) and (5 m, 45°) in free space. It is noted that the direct signal from the transmitter to receivers is not included in the simulation results presented in this section. Transmitter is located at the center of the room (the center of the coordinate system). The frequency samples are over the band 1.2−2 GHz with 10 MHz steps. Number of samples is chosen to be 65 with the spacing of $\lambda_{min}/2$ (λ_{min} is the minimum wavelength). It can be observed that this configuration for sampling points results different cross-range resolutions for different observation directions since the effective length of the array along the direction perpendicular to the observation direction varies for different observation directions. As shown in Figure 2.4(a), the effective length of the array for each observation direction is defined as the length of the array formed by projection of the sampling points to a line perpendicular to the observation direction. In Figure 2.3(a), the effective

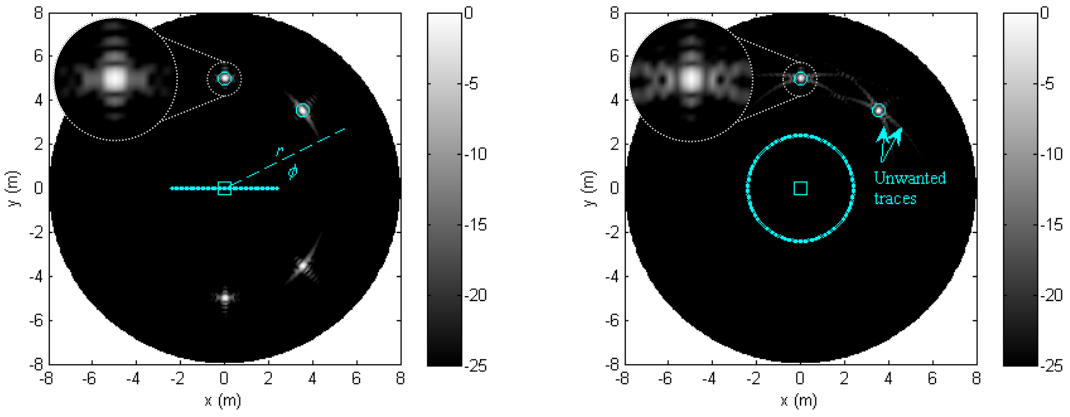

(a) (b)

Figure 2.3. Normalized PSF calculated using uniform array coefficients for two point targets located at (r, ϕ) = (5 m, 90°) and (5 m, 45°) [13]. (a) Sampling points on a line. (b) Sampling points on a circle. (square is the Tx position, circles represent point targets positions, dots are sampling points positions)

length of the array for the observation direction along ϕ = 90° is equal to the length of the array but for the observation direction along ϕ = 45°, the effective length is $1/\sqrt{2}$ of the actual length of the array and therefore, the image has worse cross-range resolution for the object located at (5 m, 45°). The cross-range resolution for each observation direction is measured along $\hat{\phi}$ direction which is equal to $r\lambda_c/(2L)$ where r is the range, λ_c is the wavelength at the center frequency and L is the effective length of the array for each observation direction.

It can be also observed in Figure 2.3(a) that the images of objects are mirrored with respect to the array. This is due to the omnidirectional radiation pattern of the transmitting and receiving antennas which cannot discriminate between the signals received from the top or bottom. These mirrored images result in serious ambiguity in detection of the real locations of the objects.

Simulation of multiple sampling geometries indicate that sampling configurations close to concentric circles (receivers are moving on concentric circular paths) and the transmitter is located at the center provides the best results. This configuration can provide uniform cross-range resolution in all directions since the effective length of the array is the same for all observation

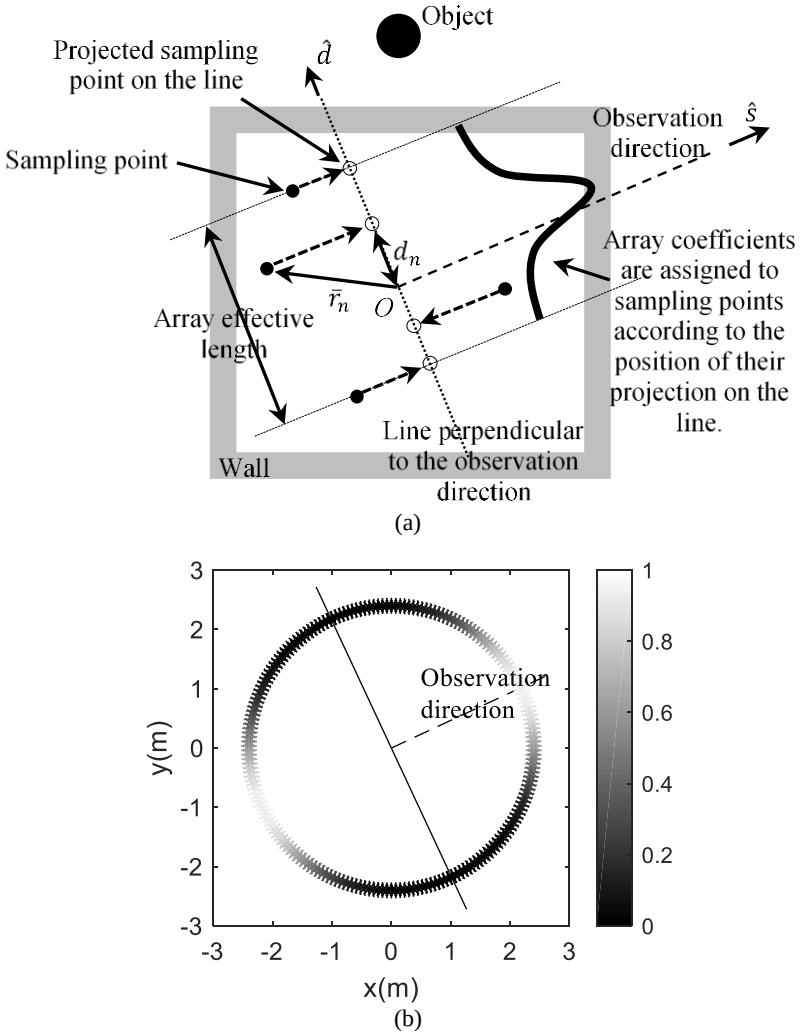

Figure 2.4. (a) Projection of sampling points on the line perpendicular to the observation direction to find a_n's. O denotes the center of the coordinate system [13]. (b) A sample of assigning cosine-squared coefficients to the receivers according to the observation direction. Color of each receiver indicates the value of a_n (in the range 0−1).

directions. In practice, due to presence of possible obstacles on the movement path of the receivers, the sampling points may be located on deformed circular curves as shown in Figure 2.1. This results in small variations in the cross-range resolution in different directions. With the selected sampling configuration, also the ambiguity issue related to the detection of the objects positions is removed since each array element mirrors the image of each object at different position and therefore the final mirrored image points are not coherently added. Figure 2.3(b) shows the PSF for the two point objects mentioned before calculated by 202 sampling points located on a circle

with radius of 2.4 m. This configuration produces the same length for the array as the previous configuration. The spacing for sampling points is $\lambda_{min}/2$. It is observed that both objects have been imaged with the same cross-range resolution and no ambiguity is observed.

Uniform array coefficients, i.e. a_ns = 1 in (2.1), are used to form the images in Figure 2.3. Among all conventional arrays, uniform array distribution yields the narrowest PSF [41]. Another important characteristic of the array's PSF is sidelobe level which produces background noise and unwanted traces around the imaged objects as shown in Figure 2.3(b). To reduce the sidelobe level, non-uniform array coefficients can be used at the expense of wider beamwidth and lower cross-range resolution. To eliminate the sidelobes, cosine-squared array coefficients are used. To determine what coefficient should be applied to each array element in (2.1), first, the sampling points are projected to a line passing from the origin and perpendicular to the observation direction as follows

$$\hat{s} = cos(\phi)\hat{x} + sin(\phi)\hat{y}, \tag{2.2a}$$

$$\hat{d} = -sin(\phi)\hat{x} + cos(\phi)\hat{y}, \tag{2.2b}$$

$$d_n = \bar{r}_n \cdot \hat{d} = -x_n sin(\phi) + y_n cos(\phi), \tag{2.2c}$$

where, according to Figure 2.4(a), $\hat{s}$ is the unit vector along the line passing the origin and image point, indicating the observation direction. $\hat{d}$ is the unit vector perpendicular to the observation direction and along the line which the sampling points are projected, $\bar{r}_n$ is the position of the nth smapliung point, and d_n is the position of the projected nth sampling point on the line perpendicular to the observation direction. ϕ is the angle between the observation direction and the x axis according to Figure 2.3(a). The cosine-squared coefficients are assigned according to the location of the projected points as illustrated in Figure 2.4(a). The cosine-squared coefficients are assigned according to the formula

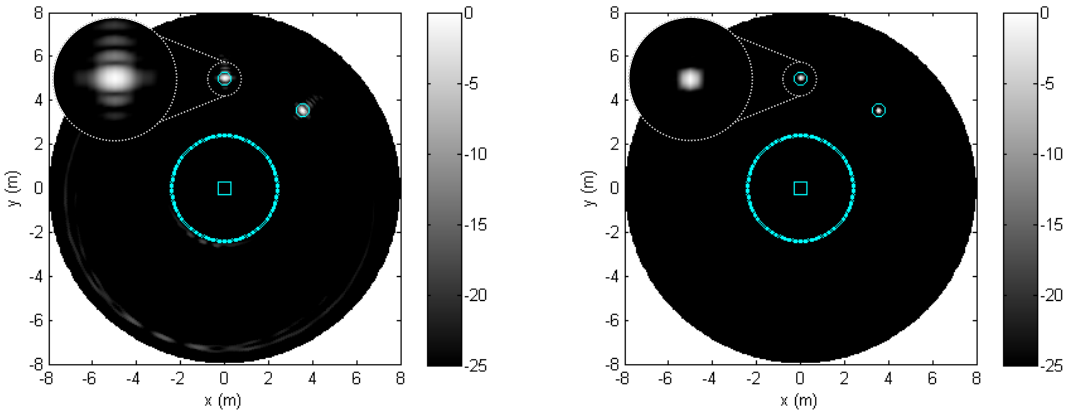

Figure 2.5. Normalized PSF calculated for the same configuration as Figure 2.3(b) [13]. (a) Image calculated using cosine-squared coefficients. (b) Multiplication of Figure 2.3(b) and Figure 2.5(a). (square shows the Tx position, circles represent point target positions, dots are sampling points positions)

$$a_n(d_n) = \cos^2\left(\pi\left(\frac{d_n - d_{min}}{d_{max} - d_{min}}\right) - \frac{\pi}{2}\right), \tag{2.3}$$

where d_{min} and d_{max} are minimum and maximum of d_ns, respectively. Figure 2.4(b) shows a sample of assigning cosine-squared coefficient to receivers for a specific observation direction. In this figure, color of each receiver indicates the value of assigned a_n in the range 0–1.

To obtain a 360° view of the imaging area, the observation direction (angle) is changed from 0° to 360° and for each observation direction different coefficients are assigned to sampling points according to the procedure mentioned above. Figure 2.5(a) shows the PSF for the same scene as in Figure 2.3(b) but using cosine-squared weighting factor. In this case, the unwanted traces around the imaged objects have been removed while the cross-range resolution has been decreased in all directions. To maintain the fine cross-range resolution of the uniform array and the low sidelobe level of the cosine-squared array in the final image, the two images in Figure 2.3(b) and Figure 2.5(a) can be multiplied. The result is shown in Figure 2.5(b) where it is shown that the background noise and unwanted traces are reduced while the cross-range resolution is approximately the same as the Figure 2.3(b).

2.3. Improving the Image Quality Using Orthogonal Circular Polarizations

With omnidirectional transmitting and receiving antennas utilized in the proposed method, the receivers are exposed to the direct signal from the transmitter. The direct signal with higher power than the signals received from wall reflections or point scatterers can adversely affect the system performance in two ways: 1) it can saturate the sensitive receivers and reduce receiver dynamic range necessary for detecting small objects, and 2) it produces strong response at the transmitter location with large sidelobes in the final image. As mentioned before, due to the finite length for the array, sidelobes generate unwanted traces around the imaged objects. For high power direct signal from the transmitter, these sidelobes have a large magnitude that can mask the image of the weak scatterers close to the transmitter in the final image.

Another drawback of utilizing omnidirectional antennas is reception of direct signal from transmitter to receiver as well as multiple reflections of the transmitted signal from building's interiors at sampling points (illustrated in Figure 2.6), which produces spurious images and increases the background noise in the final image. The spurious images are mainly produced by double reflection from the corners and other multiple reflections from the parallel walls. The background noise is mainly generated by sidelobes of these spurious images.

To show the effect of direct signal from the transmitter to receivers and also multiple reflections on the final image, the configuration shown in Figure 2.7(a) is considered. According to Figure 2.7(a), the imaging area is a room with interior dimensions of 5 m × 5 m. The thickness, relative permittivity, and conductivity of the walls are 0.2 m, 3, and zero, respectively. There exists a PEC cylinder behind the walls at (r, ϕ) = (5 m, 90°) with the radius of 0.2 m. Number of sampling points (location of receivers) is chosen to be 441 which are located on three concentric circles with the radii of 1.25, 1.75, and 2.25 m. The transmitter is located at the center of the circles and also

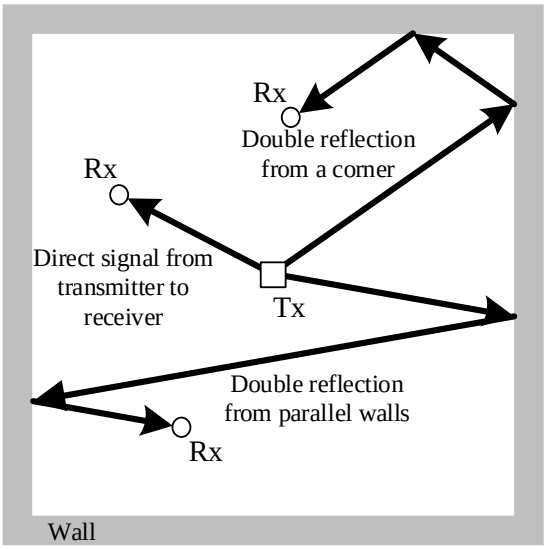

Figure 2.6. Unwanted signals received by omnidirectional antennas in all-directions through-the-wall imaging.

the origin of the coordinate system. As before, the sampling points spacing is $\lambda_{min}/2$. To obtain the frequency response at the sampling points, 2-D COMSOL simulations for vertical and horizontal polarizations have been performed separately over the band 1.2–2 GHz with 10 MHz steps. Vertical polarization and horizontal polarization have been generated using line current and magnetic current sources, respectively. All the images in this section are obtained using (2.1) with uniform coefficients. Figure 2.7(a) and Figure 2.7(b) show the simulated radar image for Tx and Rx antennas vertical polarization and Tx and Rx antennas horizontal polarization, respectively. In both images, the peak at the center is due to the direct signal from the transmitter to receivers. The four spurious peaks at the corners of the walls in Figure 2.7(a) are due to the double reflections from the corners. These peaks are not observed in Figure 2.7(b) since the reflection coefficient of the horizontal polarization is smaller than vertical polarization at oblique angles close to 45°. As a case in point, the horizontally polarized wave experiences far less reflection than vertically polarized wave at angles near the Brewster angle (i.e. the Brewster angle only happens for

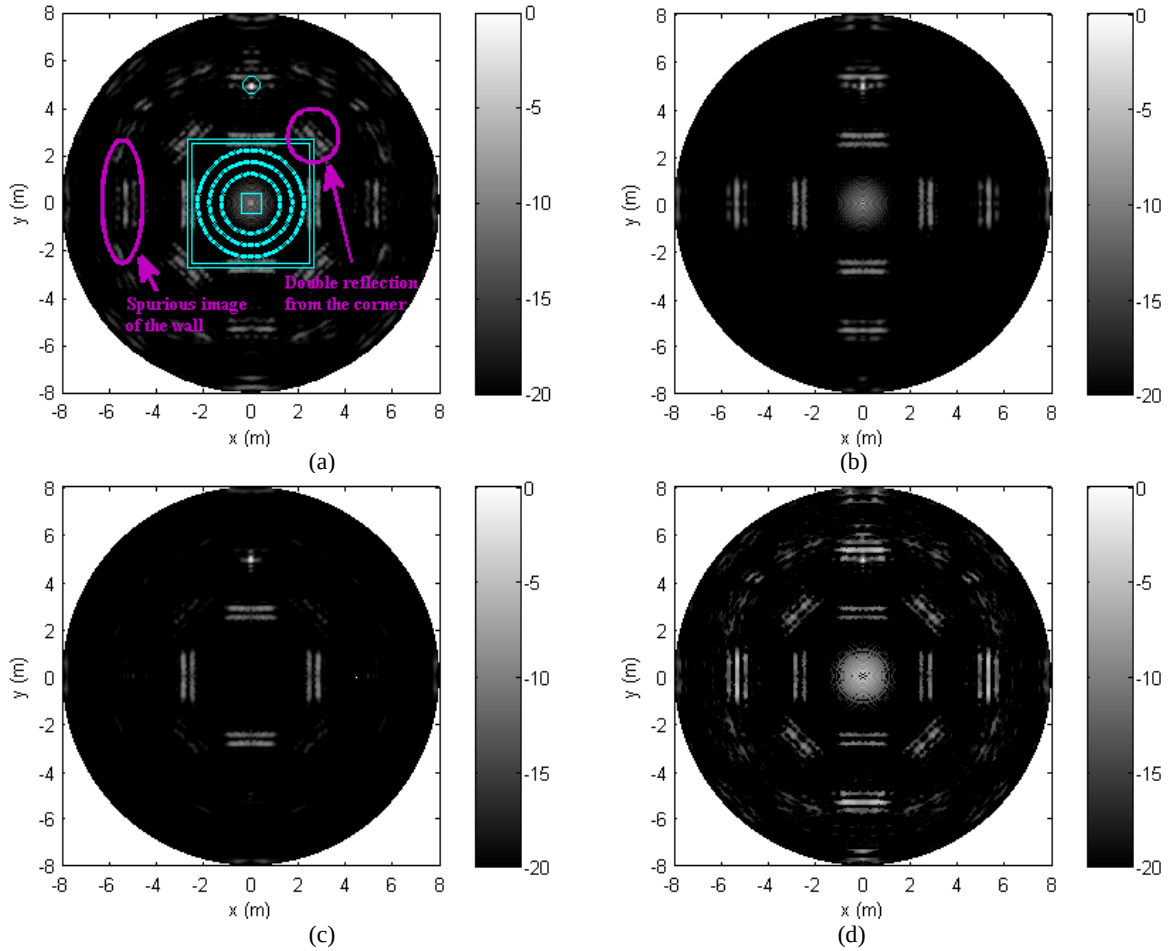

Figure 2.7. (a) Geometry of the problem where the wall boundary is shown by solid square, Tx position is shown by a small square, target position is shown by a small circle, and sampling points are shown by dots. Also shown is the normalized image (dB) for Tx and Rx antennas with vertical polarization. (b) Normalized image (dB) for Tx and Rx antennas with horizontal polarization. (c) Normalized image (dB) for orthogonal circular polarizations (LHCP for transmitter and RHCP for receiver). (d) Normalized image (dB) for the co-polarized LHCP for transmitter and receiver [13].

horizontal polarization with respect to the ground). In both figures, the four spurious images of the walls are due to the double reflections from the parallel walls.

To mitigate the adverse effects of utilizing omnidirectional antennas, orthogonal polarizations are used for transmitting and receiving antennas. In the proposed imaging method, left-handed circular polarization (LHCP) and right-handed circular polarization (RHCP) are used for transmitter and receivers, respectively. With orthogonal circular polarizations, the polarization isolation between the antennas attenuates the direct signal from transmitter to receiver as well as the received signals that experienced even number of reflections (including double reflections) in

their path from transmitter to receivers. At each reflection, the handedness of the reflected signal flips and as a result signals arriving at receivers with even number of reflections will have polarization mismatch with the receiver antenna [42]. Figure 2.7(c) shows the capability of the imaging system with orthogonal circular polarizations in reducing of the direct signal and contribution from scattering points produced by even number of reflections. In this figure, the polarization of the transmitted signal and received signal is LHCP and RHCP respectively. It is shown that the effect of direct signal at the center is completely removed and also the wall boundaries and the object are imaged with a higher intensity. In addition, the spurious images at the corners due to double reflections are significantly reduced but not completely removed. The reason is due to the fact that the responses of the wall boundaries to vertical and horizontal polarizations (two components of circular polarization) are not the same at oblique angles which can also be discerned from Figure 2.7(a) and Figure 2.7(b). In Figure 2.7(c) the spurious images of the walls (due to double reflections) are also significantly reduced. This is important since one of these spurious images is located at the object position according to Figure 2.7(a). It is noted that for all imaging results reported in this section, the location of the image of target is the location of the point on the boundary of target which is closest to sampling points. For the cylindrical target mentioned above (with radius of 0.2 m), this point is located at (4.8 m, 90°). In Figure 2.7(c) the location of this point is detected at (4.92 m, 90°). The 0.12 m error in the detected range is due to the fact that the excess delay through the wall is not compensated in this imaging method. For the wall with thickness and relative permittivity of t_W and $\varepsilon_{r,W}$, the range error due to the wall excess delay is $t_W(\sqrt{\varepsilon_{r,W}} - 1)$ for normal incidence with respect to the wall boundary. For the wall in Figure 2.7(c) with t_W = 0.2 m and $\varepsilon_{r,W}$ = 3, this error is calculated 0.146 m which is close to the detected error.

Figure 2.7(d) shows the imaging results when the transmitter and receiver have the same circularly polarized (LHCP) antennas. In this case, image points with dominant single-bounce scattering mechanisms are reduced or completely eliminated. This image enhances the response of imaging points with even-bounce scattering mechanism. It is noted here that the thin cylindrical object is still imaged since the responses to vertical and horizontal polarizations are different. The LHCP and RHCP responses are obtained by combining COMSOL simulations of vertical and horizontal polarizations and applying the required ±90° phase difference between the two linear polarizations.

Figure 2.8 shows the imaging result for the same configuration as Figure 2.7 except that the wall relative permittivity has been increased to 6. Figure 2.8(a) shows the simulated radar image for Tx and Rx antennas vertical polarization. In this figure, due to high reflectivity of the walls, the magnitude and number of spurious images due to the multiple reflections are increased compared to Figure 2.7(a). Figure 2.8(b) shows the imaging result for LHCP transmitted signal and RHCP received signal. In this figure, although utilizing orthogonal circular polarizations reduces spurious images due to even number of reflections and also the effect of the direct signal from transmitter but there still exist images due to multiple reflections that must be removed. In Chapter 5, a method for improving the image quality is presented and applied to Figure 2.8(b) to reduce the spurious images. In Figure 2.8(b), the target is detected at 5.045 m which is equal to 0.245 m error in detection of the object position. The calculated error for the wall with t_W = 0.2 m and $\varepsilon_{r,W}$ = 6 is 0.29 m which is close to the detected error.

To investigate the performance of the proposed method in imaging of the objects close to the wall, the same configuration as Figure 2.7 expect that the target is located at (3.0875 m, 90°) is simulated in COMSOL. With this configuration, the minimum distance between the outer

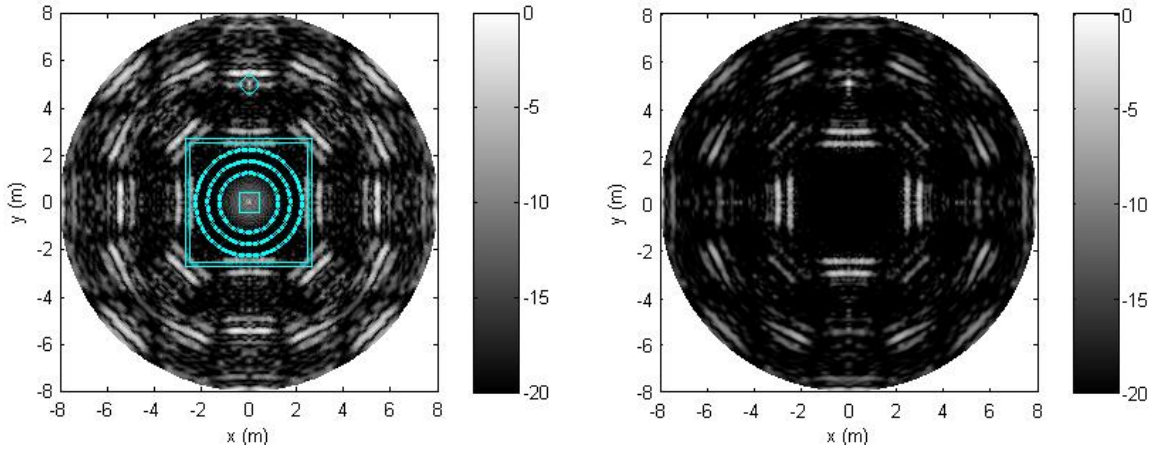

Figure 2.8. The same configuration as Figure 2.7 except that the wall permittivity is increased to 6. (a) Normalized image (dB) for Tx and Rx antennas with vertical polarization. (b) Normalized image (dB) for orthogonal circular polarizations (LHCP for transmitter and RHCP for receiver) [13].

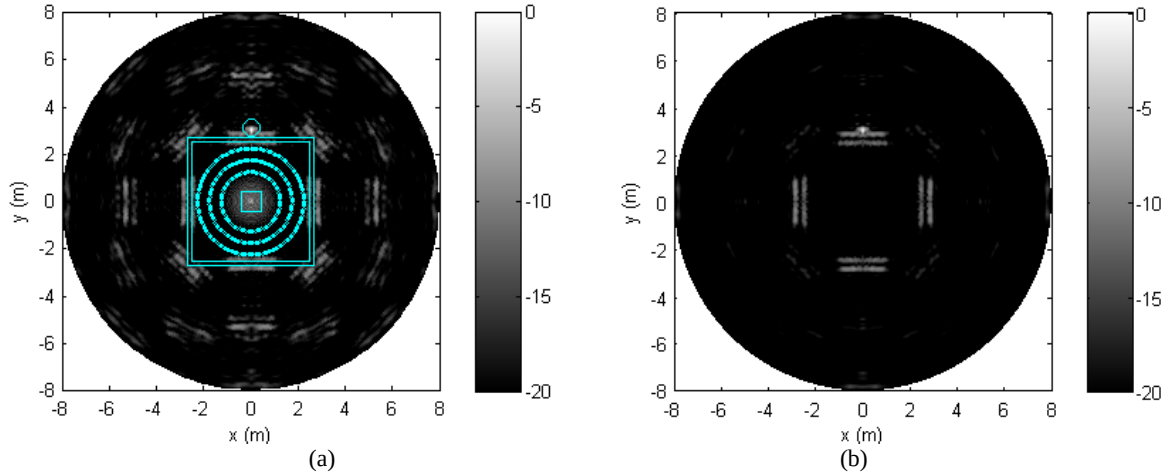

Figure 2.9. The same configuration as Figure 2.7 except that the target is located at (3.0875 m, 90°). (a) Normalized image (dB) for Tx and Rx antennas with vertical polarization. (b) Normalized image (dB) for orthogonal circular polarizations (LHCP for transmitter and RHCP for receiver) [13].

boundary of the wall and the target boundary is 0.1875 m which is equal to the range resolution obtained by 800 MHz bandwidth. Figure 2.9(a) shows the imaging result for vertical polarization transmission and reception and Figure 2.9(b) shows the result for LHCP transmission and RHCP reception. In both figures, the target is clearly imaged. Similar to previous cases, using orthogonal circular polarization reduces the spurious images. In Figure 2.9(b), the target is detected at 3 m which is equal to 0.1125 m error in detection of the object position.

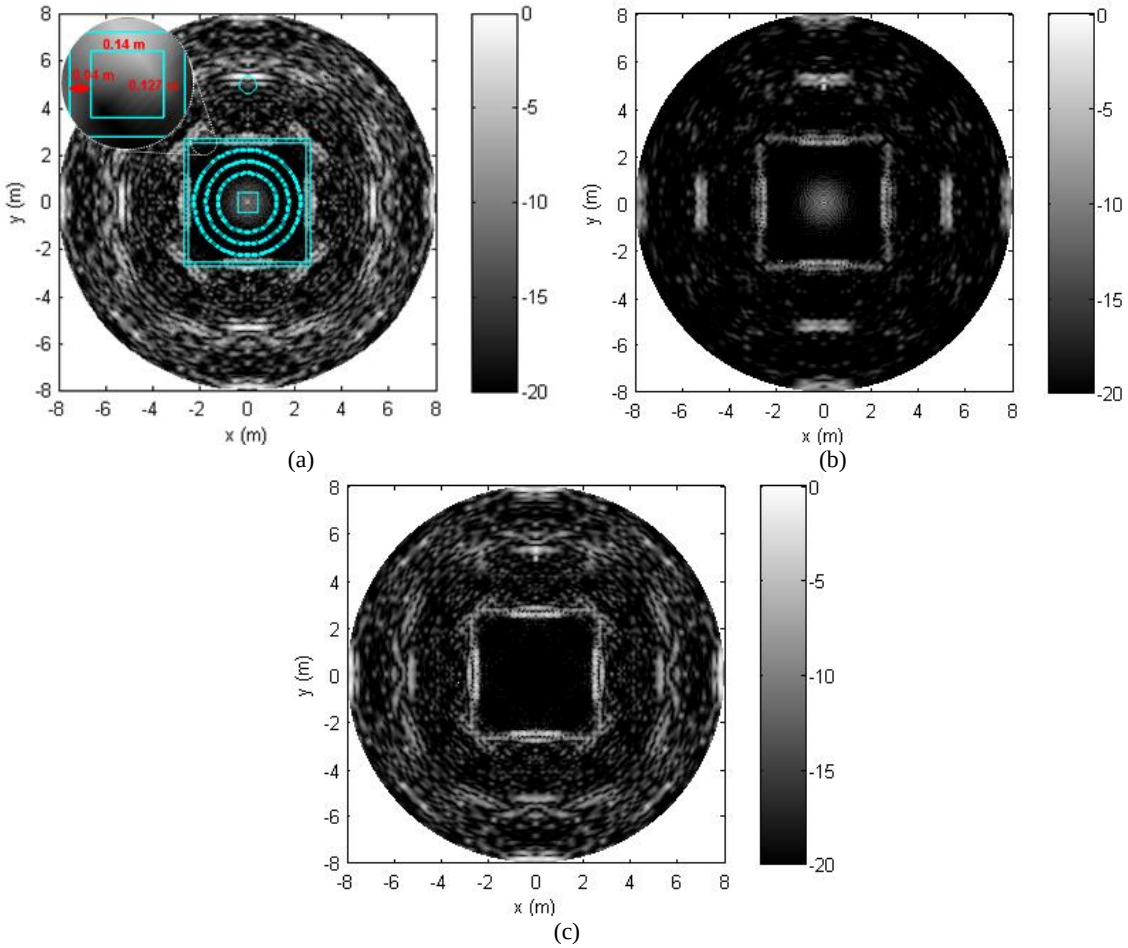

Figure 2.10. The same configuration as Figure 2.7 except that the homogeneous wall is replaced by a wall with a periodic structure. Relative permittivity of wall is 3. (a) Periodic structure of the wall and normalized image (dB) for Tx and Rx antennas with vertical polarization. (b) Normalized image (dB) for Tx and Rx antennas with horizontal polarization. (c) Normalized image (dB) for orthogonal circular polarizations (LHCP for transmitter and RHCP for receiver) [13].

To evaluate the performance of the imaging method in the presence of walls with periodic structure such as cinder block, the same configuration as Figure 2.7 is considered while the homogenous wall is replaced by a wall with periodic structure representing cinder block as shown in Figure 2.10(a). The thickness and relative permittivity of the wall are 0.2 m and 3 respectively. Figure 2.10(a) and Figure 2.10(b) show the imaging result for vertical and horizontal polarization transmission and reception respectively and Figure 2.10(c) shows the result for LHCP transmission and RHCP reception. Comparing Figure 2.10(a) and Figure 2.10(b), it is shown that the response of the wall with periodic structure to horizontal polarization is significantly different from its

response to vertical polarization. As a result, using circular polarization does not significantly improve the image quality. In Chapter 5, the proposed method for improving image quality is applied to Figure 2.10(c) to eliminate the spurious images. In Figure 2.10(c), the target is detected at 4.91 m which is equal to 0.11 m error in detection of the object position.

2.4. Performance Evaluation of the Proposed Imaging Method in Complex Scenarios

To evaluate the performance of the proposed imaging method in complex environments, a large three-dimensional structure with detailed interior is considered. The building model is shown in Figure 2.11. The overall dimensions of this model is 23.93 m × 24.10 m × 2.97 m. In addition to interior walls, the model also contains a flat floor and ceiling which are not shown in Figure 2.11. The wall and ceiling thickness, relative permittivity, and conductivity are 20 cm, 3, and 0.001 S/m respectively. The floor's dielectric and conductivity values are chosen the same as the walls. In Figure 2.11, the location of the transmitter is indicated by a red dot at the center and locations of receivers (sampling points) are indicated by blue circles. The origin of the coordinate system is at the location of the transmitter. In this case, the upper right corner of the model is located at (x, y) = (11.58 m, 13.56 m). The transmitter and receiver's height measured from the floor surface is 0.5 m. The transmitting source is a vertically oriented short dipole with total length of 15 mm and excitation current amplitude of 1 A. The receivers are all isotropic receivers. The number of receivers are chosen to be 1269 which are located on three concentric circles with the centers located at the transmitter position and radii of 3 m, 5 m, and 7 m. The spacing between the receivers are 75 mm which is equal to half wavelength at 2 GHz. To calculate the received signal at receivers, the wave propagation and scattering in the building of Figure 2.11 is simulated in the EM.Terrano module of EM.CUBE software [43] which is a high fidelity ray tracing solver based on the

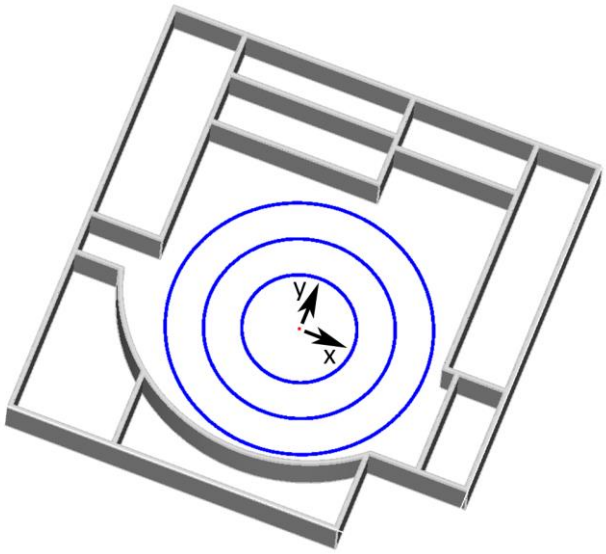

Figure 2.11. A large and complex three-dimensional building model for evaluation of the proposed imaging method (the ceiling and the floor are not shown). The dot at the center indicates the location of the transmitter and the three concentric circles indicate the location of receivers (sampling points) [13].

shooting-and-bouncing-rays (SBR) method. In this simulation, the maximum number of ray interactions is set to 11 and minimum power for tracing the rays is set to -80 dBm. The model is simulated over the frequency band 1.2−2 GHz with frequency step (Δf) of 5 MHz (161 steps). This results in an alias-free (unambiguous) range of 30 m (= $c_0/(2\Delta f)$). In this simulation the received signal used to form the image is the z-component (vertical component) of the electric field. Here, received signal at each receiver includes the direct signal from the transmitter to the receiver (polarization matched condition).

Figure 2.12(a) shows the image calculated by (2.1) with uniform array coefficients. In this image, dashed lines indicate one of the two boundaries of each wall in the model which is closer to the transmitter. It can be observed that the parts of the walls that are reflecting the transmitted signal to receivers (specular points) are imaged. The imaged walls include the curved wall at the bottom of the building model and three walls at the center top which indicate the capability of the imaging method in detecting complex features of the buildings' interiors. In this image, some walls which do not contain specular points are missed in the radar image (e.g. the wall along y-direction

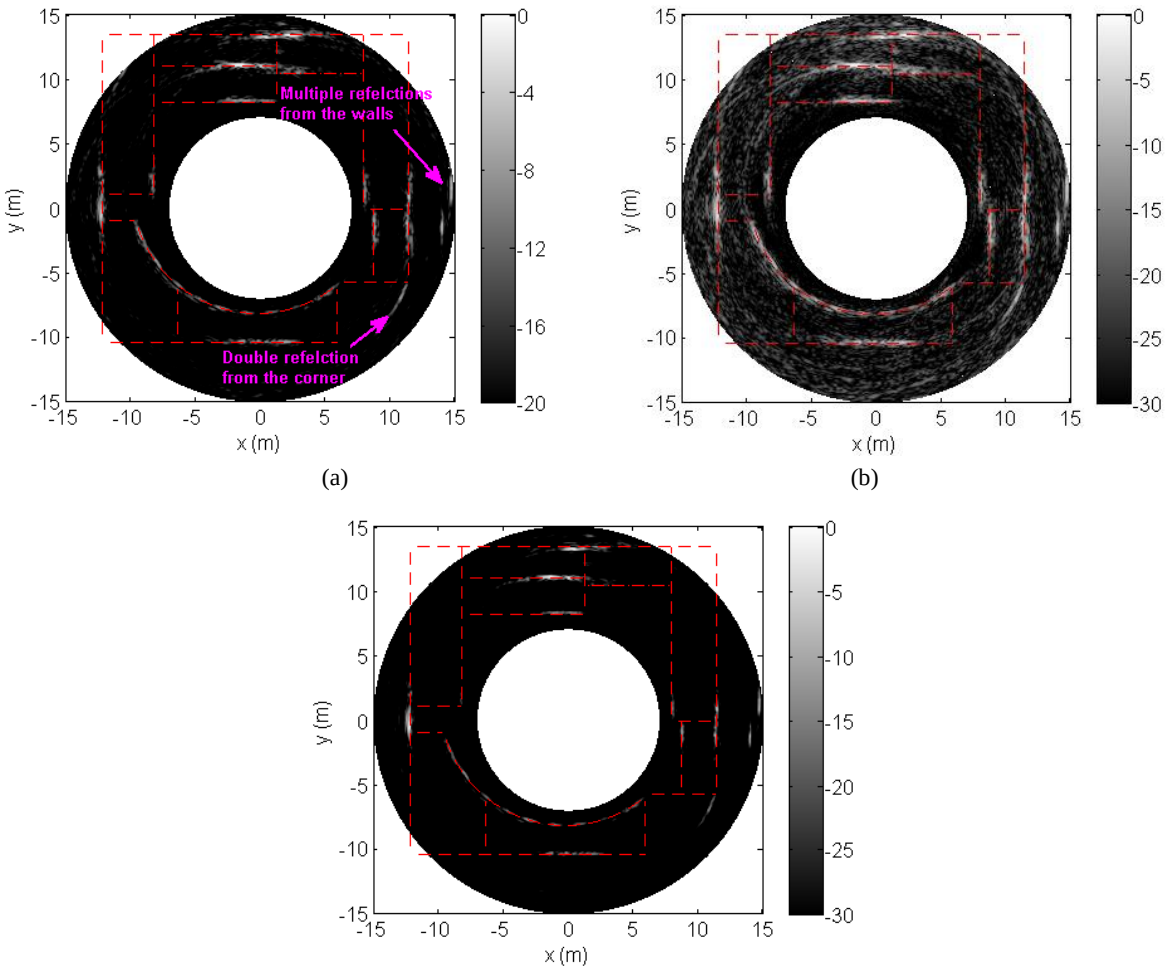

Figure 2.12. Imaging results for the model shown in Figure 2.11 [13]. (a) Image formed by (2.1) with uniform coefficients (only the pixels with image values greater than -20 dB are shown). (b) The image same as (a) except that the image with pixel values greater than -30 dB is shown. (c) The image formed by multiplication of two images calculated separately by applying uniform and cosine-squared array coefficients (only the pixels with the values greater than -30 dB are shown).

at the center top of the building). This limitation is not specific to the proposed imaging method since in conventional imaging methods, a linear array of antennas along x-direction cannot detect walls along y-direction either. In the proposed method, adding extra sampling points at different locations and/or changing the position of transmitter can solve this problem in some cases. As an example, moving the transmitter slightly to an upper location in Figure 2.12 can result better imaging of the walls along y-direction at upper left and upper right of the building. Since this simulation, considers co-polarized transmitter and receivers, the double bounce reflections from

the corners and multiple reflections (even) from the parallel walls appear in the image. These spurious images are indicated in Figure 2.12(a).

Figure 2.12(a) shows only the image with the value greater than -20 dB. To image the weak scatterers in the imaging area, this threshold must be decreased. Figure 2.12(b) shows the same image while the threshold is set to -30 dB in which higher background noise is observed. To reduce the background noise, the same method as described in Section 2.2 is applied to Figure 2.12(b). Figure 2.12(c) shows the image formed by multiplying two images calculated separately by applying uniform and cosine-squared array coefficients. In this figure, the background noise is significantly reduced while the majority of the imaged boundaries remained in the new image.

2.5. Conclusion

A new method for through-the-wall radar imaging is proposed. Unlike conventional methods that work in backscatter direction, the proposed approach is based on multi-static radar configuration. In image formation, a 2-D synthetic dense array is used within the imaging area instead of a real or synthetic large linear array. Instead of directive antennas with limited field of view, transmitting and receiving antennas are omnidirectional that allow for all-directions (360° view) imaging of building's interior. Using few robotic rovers, one stationary robot transmitting an ultra-wideband signal and the rest moving and receiving the scattered signals, the required data is collected quickly. A high resolution camera that views the scene of the rovers determines the relative locations of the transmitter and receivers.

Direct signal from transmitter to receivers and multiple interaction of the transmitted signal with walls and buildings' interiors are received by omnidirectional antenna and degrade the final image. To mitigate the effect of these unwanted signals, antennas with orthogonal circular

polarizations are used for transmitter and receivers. It is shown that using a beam-forming technique, the image quality can be further improved.

Using FEM for simple scenarios and a high-fidelity ray tracing wave propagation model for a complex indoor environment, it is shown that accurate radar images with 360° field of view and high resolution can be generated using the proposed through-the-wall imaging method.

Chapter 3 Wideband Circularly Polarized Omnidirectional Antenna for All-Directions Through-the-Wall Imaging

3.1. Introduction

Circularly polarized (CP) antennas used for radar applications are capable of reducing multipath fading due to multiple reflections from building walls and other scatterers. Also in wireless communications, CP antennas can eliminate the need for precise alignment of the transmitting and receiving antennas. The latter is important in satellite communication systems where precise alignment of the transmitting and receiving antennas is difficult. To provide a large signal coverage and support different wireless standards, CP antennas with omnidirectional radiation pattern and wide bandwidth are more desirable.

Several designs have been proposed for CP omnidirectional antennas with conical-beam radiation pattern [44]−[59]. In general, two different approaches are pursued to generate circular polarization. The first approach is using two different structures to simultaneously excite vertically and horizontally polarized waves with 90° phase difference. The designs based on this approach are typically low-profile and utilize circular patch for vertical polarization and curved stubs connected to the patch to form a loop for horizontal polarization. To increase the bandwidth of vertical polarization radiation, shorting vias are added to the circular patch. With this technique, the TM_{01} mode of the circular patch is excited in addition to the basic TM_{02} mode and thus the bandwidth is improved [44], [47], [50]. In [47], this structure is modeled and analyzed by epsilon negative transmission lines. To improve the bandwidth for horizontal polarization, the

curved stubs can be coupled to the patch instead of direct connection [50]. The variant of the mentioned structure is also used. In [52], the horizontal polarization is obtained by slits asymmetrically placed on top and bottom planes. Including PIN diodes in the structure to switch the direction of rotation of the formed loop for horizontal polarization, enables polarization reconfigurability [51], [53]. Although the designs utilizing circular patch and curved stubs are low-profile and can be easily fabricated using PCB technology, their axial-ratio (AR) bandwidth is typically less than 20%. To improve the bandwidth, in [55], vortex slots and shorting vias are used to include one more mode of operation to the structure for vertical polarization (in addition to conventional circular patch TM_{01} and TM_{02} modes). This design achieves 57.9% of 3-dB AR bandwidth. Another structure based on the mentioned approach is proposed in [48]. In this structure, a dielectric resonator excited by an axial probe generates vertical polarization and an Alford loop coupled to the dielectric resonator generates horizontal polarization. In [56], a broadband omnidirectional circularly polarized antenna is proposed using a combination of broadband omnidirectional vertically and horizontally polarized antennas. The design has 49.7% of 3-dB AR bandwidth.

The second approach for obtaining circular polarization is using a linearly polarized radiator surrounded by wave polarizers to excite orthogonal quadrature waves. In [46], dielectric polarizers are placed around a simple monopole antenna in a bird nest like structure to convert linear vertical polarization to circular polarization. This design has 54.9% of 3-dB AR bandwidth. A rectangular dielectric resonator with inclined slots and metallic cylinders is proposed in [45] for CP operation. In the proposed structure, rectangular dielectric resonator generates linear vertical polarization and slots and metallic cylinders act as polarizers. This design achieves 25.4% of AR bandwidth.

There are few designs for wideband CP omnidirectional antennas with more than 40% 3-dB AR and 10-dB impedance bandwidth [46], [55]−[57]. In this chapter, a novel wideband CP omnidirectional antenna is introduced. The antenna utilizes an approach for obtaining circular polarization different from the two approaches mentioned above. The antenna operates based on excitation of a field distribution similar to circular waveguide TE_{21} mode in free space and in the near-field region of the antenna. It is shown that this field distribution generates a far-field linearly polarized electric field whose polarization tilt angle varies in azimuthal directions. Due to the symmetry in the field distribution of the mode, the direction of the linearly polarized electric field varies by 90° if azimuth angle increases by 45°, i.e. if in the azimuth angle ϕ the electric field is horizontally polarized, at $\phi \pm 45°$, it is vertically polarized. This suggests that if two field distributions similar to circular TE_{21} mode are excited in free space simultaneously such that one mode is spatially rotated by 45° with respect to the other mode, then in the far-field region, two orthogonal linearly polarized electric fields are generated. In this case, omnidirectional circularly polarized radiation can be obtained by exciting the two modes by 90° phase difference.

To excite each circular TE_{21} like field distributions in free space over a wide bandwidth, an array of four monopole sectorial loop antennas (SLA) [60], [61] radially placed over a circular ground plane is used. The CP antenna is formed by eight monopole SLAs (for excitation of two TE_{21} modes) mounted on a circular ground plane. It is shown that increasing the number of elements to 16, increases the 3-dB AR bandwidth. The final antenna with 16 monopole SLA elements is fabricated and measured. To excite each element with the required excitation amplitude and phase, a feed network including Wilkinson power dividers and low-pass/high-pass (LP/HP) phase shifters is designed and fabricated. The measurement results show 63% of 3-dB AR bandwidth and 58% of operation bandwidth (3-dB AR and 10-dB impedance bandwidth) with the

center frequency at 1.565 GHz. Comparing to the previous works, the proposed antenna has the highest 3-dB AR and operation bandwidth. The maximum height of the antenna (excluding the connector) is 47 mm.

The antenna is designed for the proposed all-directions through-the-wall imaging method to reduce the direct line-of-sight transmitter to receiver signal and alleviate the negative effects of double reflections in the final image. For this application, the performance of the antenna in horizontal plane is important and thus all measurements are performed in the horizontal plane.

In Section 3.2, the far-field radiation characteristics of circular TE_{21} mode are investigated. In Section 3.3, using an array of four monopole SLAs mounted on a ground plane, a field distribution similar to circular TE_{21} mode is excited in free space. In Section 3.4, a CP antenna structure with eight monopole SLAs is presented. In section 3.5, to increase the 3-dB AR bandwidth of the antenna, the number of elements is increased to 16 elements. Measurement and simulation results for the antenna with 16 monopole SLAs and the feed network structure are given in Section 3.6.

3.2. Far-Field Electric Field Generated by Excitation of Circular TE_{21} Mode

In the proposed method, the circular polarization is obtained by exciting the field distribution similar to circular TE_{21} mode in free space. To study the characteristics of the electric field radiated by circular TE_{21} mode, a circular aperture with radius of a located at z = 0 is considered according to Figure 3.1(a). It is assumed that circular TE_{21} field distribution is excited over the fictitious aperture. In this case, the field distribution at the aperture S (E_a) is

$$E_a(\rho,\phi) = \frac{2}{\rho} J_2\left(\frac{\chi'_{21}\rho}{a}\right)\sin(2\phi)\,\hat{\rho} + \frac{\chi'_{21}}{a} J'_2\left(\frac{\chi'_{21}\rho}{a}\right)\cos(2\phi)\,\hat{\phi} \tag{3.1}$$

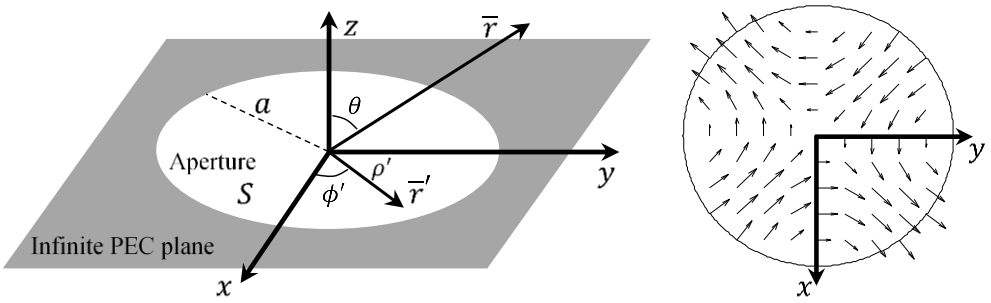

(a) (b)

Figure 3.1. (a) Geometry of the aperture. (b) Electric field distribution of circular TE_{21} mode [16].

where, J_ν is the Bessel function of the first kind of order ν and χ'_{21} is the first zero of $J'_2(x)$ and equals 3.054. The electric field distribution of circular TE_{21} mode is shown in Figure 3.1(b). To calculate the radiated fields at $z > 0$, equivalence principle is used to calculate the tangential magnetic and electric current sources on the aperture. Since the aperture is surrounded by infinite PEC plane at $z = 0$, the only current that is required for calculation of fields is the magnetic current ($\bar{J}_m$) given by

$$\bar{j}_m(\rho,\phi) = -\hat{n} \times \bar{E}_a = -\frac{2}{\rho} J_2\left(\frac{\chi'_{21}\rho}{a}\right)\sin(2\phi)\,\hat{\phi} + \frac{\chi'_{21}}{a} J'_2\left(\frac{\chi'_{21}\rho}{a}\right)\cos(2\phi)\,\hat{\rho} \quad (3.2)$$

where, $\hat{n}$ is a unit vector normal to the aperture and is equal to $\hat{z}$ according to Figure 3.1. Using the image theory, the far-field electric field ($\overline{E}_{ff}$) due to the magnetic current distribution $\bar{j}_m$ given by (3.2) is obtained from

$$\overline{E}_{ff} = -\frac{jke^{-jkr}}{4\pi r}\int_S \left(2\bar{j}_m(\rho',\phi') \times \hat{r}\right) e^{jkr'.\hat{r}}\, ds' \quad (3.3)$$

where, the coefficient 2 in the integrand is for the image theory and S is the aperture surface in Figure 3.1(a). After some manipulations, the $\hat{\theta}$ and $\hat{\phi}$ components of $\overline{E}_{ff}$ are obtained by

$$E_{ff,\theta} = -\frac{jke^{-jkr}}{2\pi r}\left(A\cos(\phi) + B\sin(\phi)\right) \quad (3.4a)$$

$$E_{ff,\phi} = -\frac{jke^{-jkr}}{2\pi r}\cos(\theta)\,(-A\sin(\phi) + B\cos(\phi)). \tag{3.4b}$$

In (3.4), A and B are defined as

$$A(\theta,\phi) = \int_{-\pi}^{\pi}\int_{0}^{a}\left(-\frac{2}{\rho'}J_2\left(\frac{\chi'_{21}\rho'}{a}\right)\sin(2\phi')\cos(\phi') + \frac{\chi'_{21}}{a}J'_2\left(\frac{\chi'_{21}\rho'}{a}\right)\cos(2\phi')\sin(\phi')\right)$$

$$\times e^{ik\rho'\cos(\phi'-\phi)\sin\theta}\rho' d\rho' d\phi' \tag{3.5a}$$

$$B(\theta,\phi) = \int_{-\pi}^{\pi}\int_{0}^{a}\left(-\frac{2}{\rho'}J_2\left(\frac{\chi'_{21}\rho'}{a}\right)\sin(2\phi')\sin(\phi') - \frac{\chi'_{21}}{a}J'_2\left(\frac{\chi'_{21}\rho'}{a}\right)\cos(2\phi')\cos(\phi')\right)$$

$$\times e^{ik\rho'\cos(\phi'-\phi)\sin\theta}\rho' d\rho' d\phi'. \tag{3.5b}$$

Using the trigonometric identities and identities for derivative of Bessel functions, A and B can be simplified to

$$A(\theta,\phi) = -\left(\frac{\chi'_{21}}{2a}\right)\int_{-\pi}^{\pi}\int_{0}^{a}\left(J_3\left(\frac{\chi'_{21}\rho'}{a}\right)\sin(3\phi') + J_1\left(\frac{\chi'_{21}\rho'}{a}\right)\sin(\phi')\right)$$

$$\times e^{ik\rho'\cos(\phi'-\phi)\sin\theta}\rho' d\rho' d\phi'. \tag{3.6a}$$

$$B(\theta,\phi) = -\left(\frac{\chi'_{21}}{2a}\right)\int_{-\pi}^{\pi}\int_{0}^{a}\left(-J_3\left(\frac{\chi'_{21}\rho'}{a}\right)\cos(3\phi') + J_1\left(\frac{\chi'_{21}\rho'}{a}\right)\cos(\phi')\right)$$

$$\times e^{ik\rho'\cos(\phi'-\phi)\sin\theta}\rho' d\rho' d\phi'. \tag{3.6b}$$

Using the identity

$$J_n(x) = \frac{1}{2\pi}\int_{-\pi}^{\pi} e^{j(n\tau - x\sin(\tau))}d\tau\,, \tag{3.7}$$

in (3.6), the integrals with respect to ϕ' can be calculated and the result is

$$A(\theta,\phi) = \left(\frac{j\pi\chi'_{21}}{a}\right)\int_{0}^{a}\left(J_3\left(\frac{\chi'_{21}\rho'}{a}\right)J_3(k\rho'\sin(\theta))\sin(3\phi)\right.$$

$$-J_1\left(\frac{\chi'_{21}\rho'}{a}\right)J_1(k\rho'\sin(\theta))\sin(\phi)\Bigg)\rho' d\rho' \tag{3.8a}$$

$$B(\theta,\phi) = \left(\frac{j\pi\chi'_{21}}{a}\right)\int_0^a \Bigg(-J_3\left(\frac{\chi'_{21}\rho'}{a}\right)J_3(k\rho'\sin(\theta))\cos(3\phi)$$

$$+J_1\left(\frac{\chi'_{21}\rho'}{a}\right)J_1(k\rho'\sin(\theta))\cos(\phi)\Bigg)\rho' d\rho'. \tag{3.8b}$$

Substituting (3.8) in (3.4) results

$$E_{ff,\theta} = -\frac{jke^{-jkr}}{2\pi r}\sin(2\phi)\,(-I_1 + I_3) \tag{3.9a}$$

$$E_{ff,\phi} = \frac{jke^{-jkr}}{2\pi r}\cos(\theta)\cos(2\phi)\,(I_1 + I_3). \tag{3.9b}$$

where, I_n is:

$$I_n = \left(\frac{j\pi\chi'_{21}}{a}\right)\int_0^a J_n\left(\frac{\chi'_{21}\rho'}{a}\right)J_n(k\rho'\sin(\theta))\rho' d\rho' \tag{3.10}$$

Far-field electric field expressions given by (3.9), for $\hat{\theta}$ and $\hat{\phi}$ components of far-field electric field, indicate that:

1. The components are periodic with period 180°.
2. If one component is zero at $\phi = \phi_0$, the derivative of the other component with respect to ϕ is zero at $\phi = \phi_0$, i.e., the other components has its maximum absolute value at $\phi = \phi_0$.
3. If one component has its maximum absolute value at $\phi = \phi_0$, the other component has its maximum absolute value at $\phi = \phi_0 + 45°$.
4. According to (3.9b), $E_{ff,\phi}$ is zero at $\theta = 90°$. This is due to the infinite ground plane around the aperture.

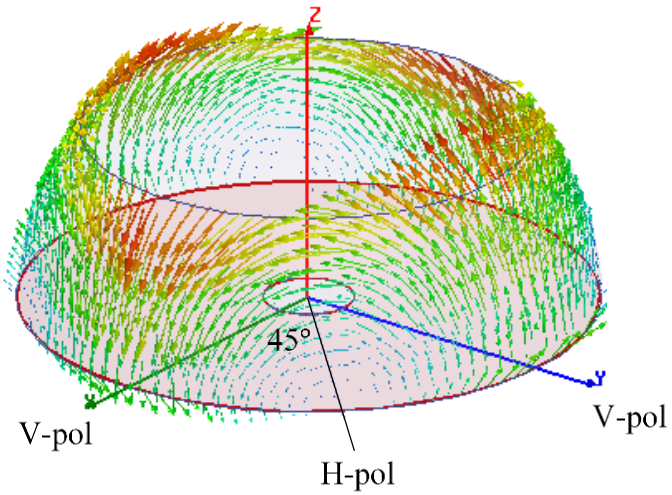

Figure 3.2. HFSS simulation result for far-field electric field of an aperture excited by circular TE_{21} mode [16].

These characteristics show that at each angle ϕ the far-field electric field is linearly polarized but its direction (polarization tilt angle) rotates as ϕ varies. As a case in point, if at $\phi = \phi_0$ the electric field is vertically polarized, at $\phi = \phi_0 + 45°$ it is horizontally polarized. To illustrate the characteristics of the radiated fields, an aperture with radius of 125 mm and excited by circular waveguide TE_{21} mode at 1.6 GHz is simulated in HFSS. Figure 3.2 shows the model and the electric field at the far-field of the aperture. It can be observed that at $\phi = 0°$, 90°, 180°, and 270°, the field is vertically polarized and at $\phi = 45°$, 135°, 225°, and 315°, it is horizontally polarized. It can be also observed that the horizontal component of the electric field (ϕ-component) is zero at $\theta = 90°$ as predicted by (3.9b).

3.3. Excitation of Circular TE_{21} Modes in Free Space for Circular Polarization Operation

A few waveguide structures have been proposed for excitation of circular TE_{21} mode [62], [63]. However, these structures are narrow band and design of a wideband antenna with these structures is not feasible. Here, instead of a waveguide structure, an array of monopole SLAs is utilized to excite a field distribution similar to circular TE_{21} mode in free space. SLA has been

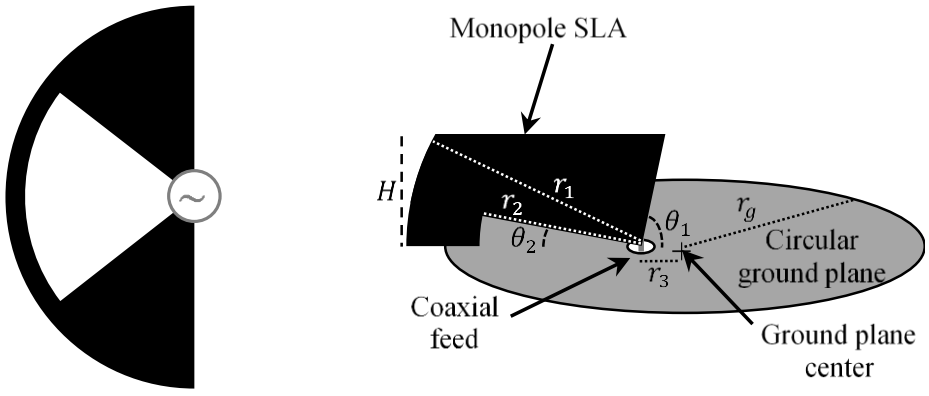

(a) (b)

Figure 3.3. (a) Topology of SLA. (b) Topology of a monopole SLA element over a circular ground plane [16].

previously used for design of wideband linearly polarized antennas [60], [61]. As shown in Figure 3.3(a), SLA is composed of two sectors connected by an arc. In the antenna, monopole SLA is used as a single element. Monopole SLA is composed of a sector and an arc which connects the end of the sector to the ground plane as shown in Figure 3.3(b). In Figure 3.3(b), top of the sector is cut to reduce the overall height of the element. The ground plane is circular with the radius of r_g.

To excite a circular TE_{21} mode, an array of four monopole SLAs radially placed over a circular ground plane is utilized as shown in Figure 3.4(a). The angle between each two adjacent elements is 90°. Excitation of each element produces a current distribution on the element's surface, which its horizontal component produces a horizontally polarized electric field along the excited element and on the top of the array according to Figure 3.4(a). It suggests that by exciting the elements with the same magnitude and phase difference of 180° between each two adjacent elements, a field distribution similar to circular TE_{21} mode can be obtained in free space. Figure 3.4(b) shows the near-field electric field on the top of the array for the mentioned excitation which is similar to circular TE_{21} mode. Figure 3.4(c) shows the far-field electric field resulted from the near-field field distribution in Figure 3.4(b) which is similar to Figure 3.2. Since SLA is inherently

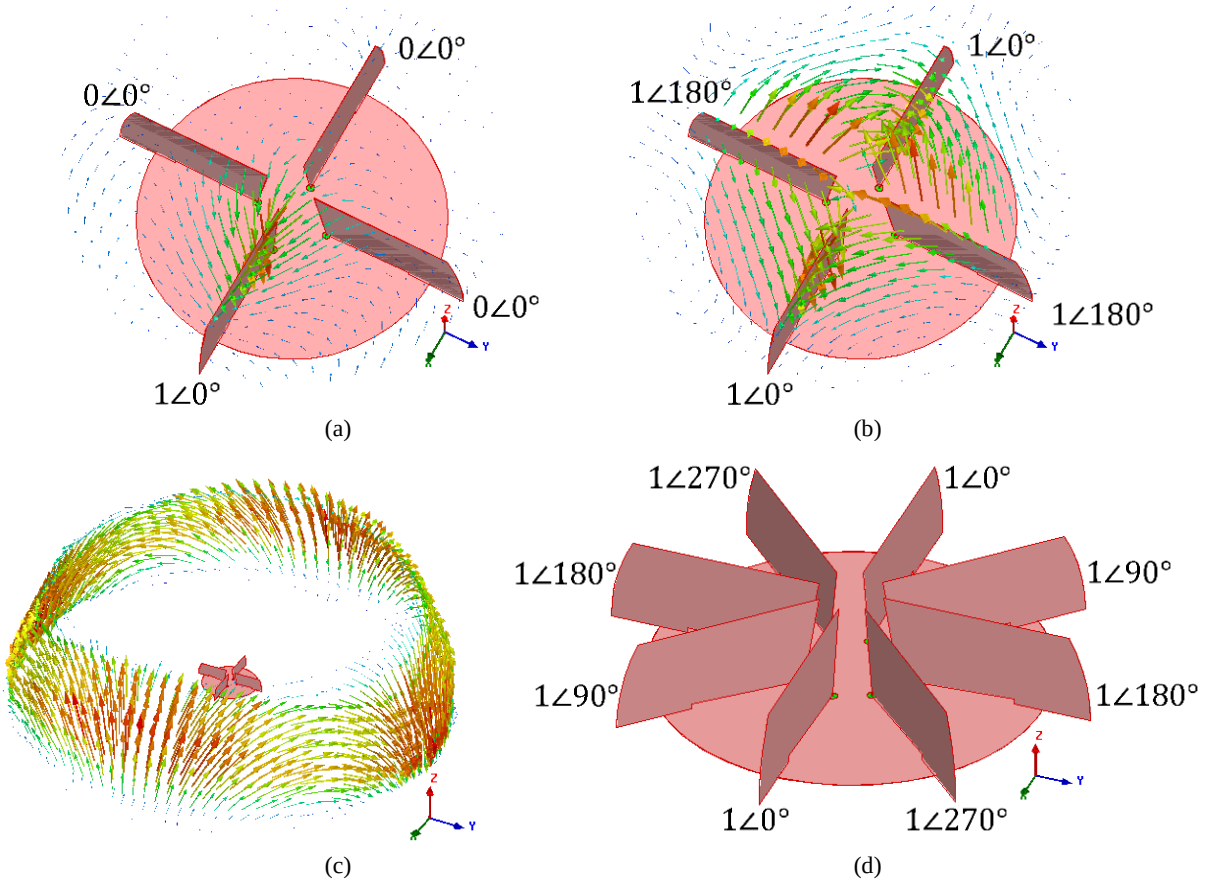

Figure 3.4. Structures for excitation of circular TE_{21} modes and circular polarization and the required excitation amplitudes and phases of the elements [16]. (a) Near-field electric field due to excitation of one element in an array of four monopole SLAs. (b) Excitation of elements to obtain circular TE_{21} in the near-field of the array. (c) Far-field electric field of the excitation in (b). (d) Structure of the CP antenna formed by eight monopole SLAs and excitation phases and amplitudes for RHCP operation.

a wideband structure, the resulting TE_{21} mode can be excited over a wide bandwidth. It is noted that in contrast to Figure 3.2, in Figure 3.4(c), the horizontal component of the electric field is not zero in horizontal plane and the structure shows significant horizontally polarized radiation at θ = 90°. This is due to the fact that the ground plane is finite in Figure 3.4.

To excite the second TE_{21} mode for circular polarization, another set of four monopole SLAs, which is spatially rotated by 45° with respect to the first set of monopole SLAs, is placed over the ground plane as shown in Figure 3.4(d). With this configuration, the final array is formed by eight monopole SLAs and the angle between each two adjacent element is 45°. The second array is excited with absolute phase difference of 90° with respect to the first array. In this case,

according to Figure 3.4(d), the phase difference between each two adjacent elements is 90°. Looking from the top, if the excitation phase decreases/increases in clockwise direction, the resulting circular polarization is left handed/right handed CP (LHCP/RHCP). The excitation phases of elements for RHCP operation are shown in Figure 3.4(d).

In the following section, the antenna formed by eight monopole SLAs is optimized for maximum AR bandwidth while maintaining a low height for monopole SLAs.

3.4. Circularly Polarized Omnidirectional Antenna Using an Array of Eight Monopole SLAs

The antenna structure with eight monopole SLAs is optimized for maximum AR bandwidth in the range 1.2−2 GHz. The optimized values for geometrical parameters in Figure 3.3(b) are: r_g = 100 mm, r_1 = 100 mm, r_2 = 60 mm, r_3 = 25 mm, H = 46 mm, θ_1 = 80°, and θ_2 = 3°. Figure 3.4(d) shows the structure of the optimized antenna. In all simulations reported here, the thickness for the monopole SLA elements and the ground plane is chosen to be 18 um which is a typical value for copper thickness of PCB substrates.

Figure 3.5 shows the maximum of AR in horizontal plane versus frequency. It can be observed that the AR in horizontal plane is less than 3 dB over the band 1.28−1.55 GHz.

Figure 3.6 shows the RHCP gain in horizontal plane at different frequencies over the band 1.28−1.55 GHz which indicates omnidirectional radiation. In the range 1.28−1.55 GHz, the minimum RHCP gain in horizontal plane is 0.76 dBi.

In this antenna structure, due to the mutual coupling among monopole SLAs, all the accepted power at each port is not entirely radiated and a part of it is coupled to the other ports. Hence, the coupling can increase the total reflected power from each port. For the antenna structure shown in Figure 3.4(d), the strongest coupling is between the adjacent ports with the maximum

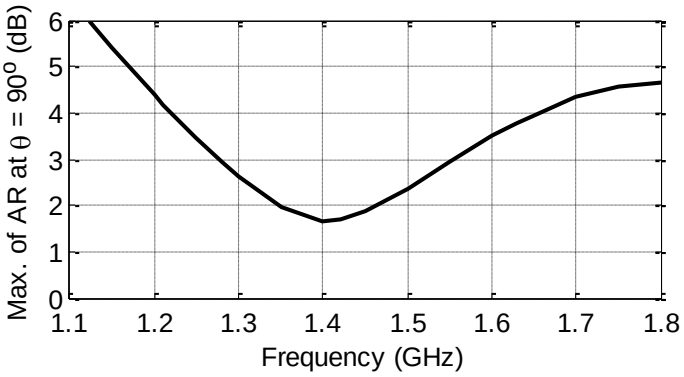

Figure 3.5. Simulation result for the maximum of AR at θ = 90° versus frequency for the antenna with eight monopole SLAs [16].

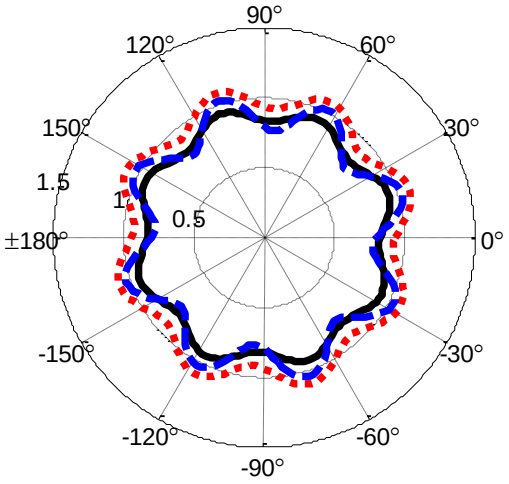

Figure 3.6. Simulation results for RHCP gain at θ = 90° and at 1.28 GHz (solid line), 1.42 GHz (dotted line), and 1.55 GHz (dashed line) [16].

level of -7.4 dB over the band 1.28−1.55 GHz. If the total reflected power at each port is low, then most of the accepted power at all the ports is radiated and thus the antenna is a good radiator with a high total radiation efficiency. In this chapter, the total radiation efficiency is defined as the ratio of the realized CP gain to CP directivity. The reflection coefficient seen from the jth port is defined as

$$\text{Reflection Coefficient (dB)} = 20\log_{10}\left(\left|\sum_{n=1}^{N} S_{jn}e^{j(\phi_{ex,j}-\phi_{ex,n})}\right|\right), \tag{3.11}$$

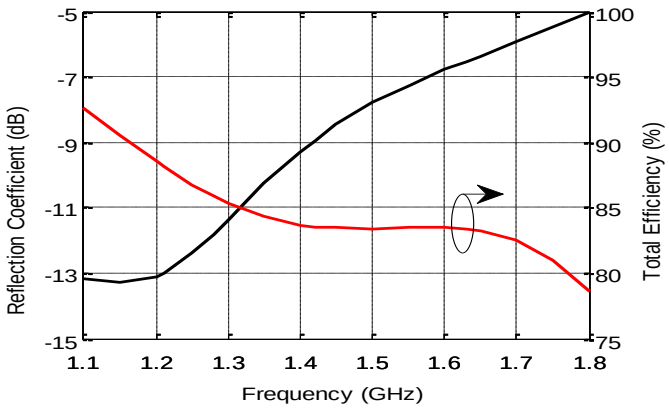

Figure 3.7. Reflection coefficient and total efficiency for the antenna in Figure 3.4(d) [16].

where, S_{jn} is the jth row and nth column of the scattering matrix modeling the antenna with N monopole SLAs as an N-port network and $(\phi_{ex,j} - \phi_{ex,n})$ is the excitation phase difference between the jth and nth ports. Due to the symmetry in the antenna structure, reflection coefficient (3.11) is the same for all the ports. Figure 3.7 shows the reflection coefficient for the antenna with eight elements which is shown to be less than -7 dB over 1.28−1.55 GHz band. Figure 3.7 also shows the total efficiency for the antenna with eight elements. It can be observed that over the1.28−1.55 GHz band, the total efficiency is more than 83%.

For good AR performance, the antenna with eight SLAs requires the phase difference of 90° between excitation signals of adjacent ports. S_{ij} shows the part of excitation signal that is not radiated and is coupled from port j to port i. It does not contribute to the radiated fields and AR. The coupled power (from one port to the other port) is dissipated in the feed network and degrades the total efficiency of the antenna. Thus, in the design of the antenna, the geometrical parameters are optimized to reduce the summation of all the couplings at each port to increase the realized gain and efficiency of the antenna.

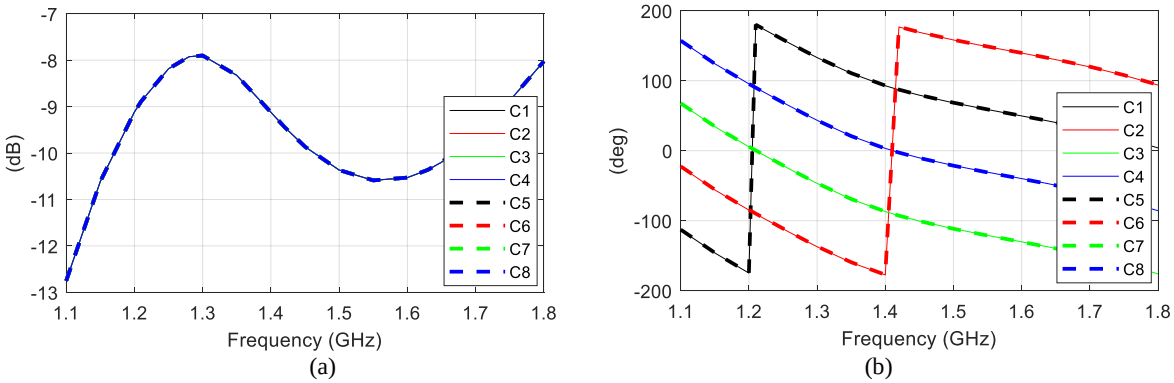

Figure 3.8. Magnitude (a) and phase (b) of the total coupled signal at different ports of the antenna with eight SLAs.

Due to the symmetry in the antenna structure and constant excitation phase difference of 90° between adjacent ports, sum of all couplings at each port has a constant phase difference of 90° between adjacent ports. The total coupling at port i (C_i) is defined as

$$C_i = \sum_{\substack{n=1 \\ n \neq i}}^{N} S_{in} e^{j\phi_{ex,n}} \tag{3.12}$$

where $\phi_{ex,n}$ is the excitation phase of nth SLA. Figure 3.8 shows the amplitude and phase of C_i (i = 1, 2, …, 8). It can be observed that all C_is have the same magnitude and the phase difference between adjacent ports is 90°.

Th effect of couplings between SLAs on the radiated field of the antenna are illustrated in Figure 3.9. The radiated fields can be divided to the zeroth order fields and higher order fields. A part of the incident signal to each port is reflected (described by S_{nn}) and the rest forms zeroth order current on each SLA. The zeroth order current forms zeroth order radiated fields (indicated by black vectors in Figure 3.9 and also contributes to the first order currents on other SLAs through coupling. The zeroth order fields are circularly polarized since they are originated from the excitation signals with the phase difference of 90° between adjacent ports.

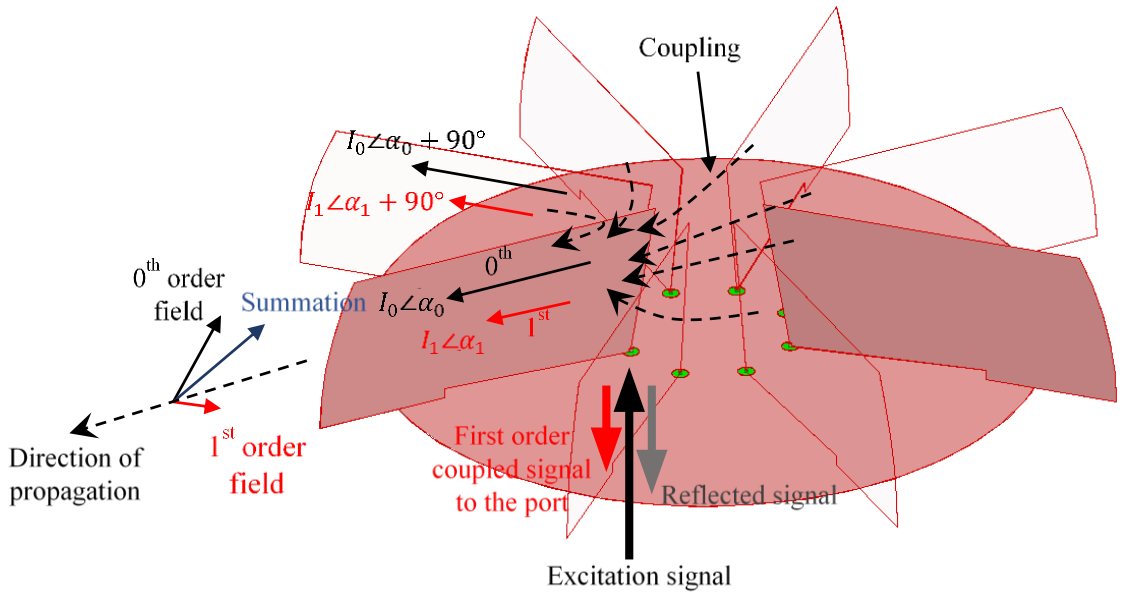

Figure 3.9. Coupling between SLAs.

The phase and amplitude of the coupled signals between each two SLAs vary by distance but due to the symmetry and phases and amplitudes of the excitation signals, the summation of all first order couplings on each SLA which forms the first order currents, has the same amplitude and phase difference of 90° between adjacent SLAs. However, the phase of the first order currents may not necessarily be the same as the phase of zeroth order currents (Figure 3.9). Considering jth SLA, a part of first order current is coupled to the other ports and contributes to $S_{ij}s$. A part of it is radiated and forms first order radiated fields and a part of it is coupled to other SLAs and forms second order currents. Since the first order currents on SLAs have the same amplitude and phase difference of 90° between adjacent SLAs, the first order radiated fields (indicated by red vectors in Figure 3.9) is circularly polarized with a phase difference with respect to the zeroth order fields. In this case, the summation of the zeroth and first order fields is also circularly polarized but its magnitude is less or more than zeroth order fields, depending of the phase difference between zeroth and first order fields. The same process is repeated for higher order fields. Finally, the total circularly polarized radiated fields (which are obtained from simulation or measurement) are

formed by the zeroth order circularly polarized field and infinite number of higher order circularly polarized fields (which are due to multiple couplings between SLAs).

For port i, each S_{ij} is formed by infinite number of couplings between ith and jth SLA. Since the coupling depends on distance between SLAs, S_{ij} is different for different pairs of SLAs. However, summation of all couplings at ports must have the same amplitude and phase difference of 90° between adjacent ports (as shown in Figure 3.8) since they are all originated from the currents with the same magnitude and phase difference of 90° as described above.

The same process holds for the antenna with 16 SLAs that is described in the next section, but the phase difference between excitation signals, coupled signals, and currents on SLAs is 45° for adjacent SLAs.

To investigate the effect of the geometrical parameters on the performance of the antenna, the parameters are varied around the chosen values and the resulting 3-dB AR bandwidth is studied. The results show that varying H, θ_1, and θ_2 around the chosen values in the range 42−50 mm for H, 75° −85° for θ_1, and 2°−5° for θ_2 has negligible effect on the performance of the antenna. Figure 3.10(a) shows the maximum of AR in horizontal plane versus frequency for the parameter $X = r_g = r_1 = r_2 + 40$ mm. In this case, the radius of the ground plane and the length of the monopole SLAs are changed simultaneously. It can be observed that increasing/decreasing both the radius of the ground plane and the length of the monopole SLAs, shifts the band of CP operation to lower/higher frequencies. Figure 3.10(b) shows that reducing r_1 (while the other parameters are kept constant) improves the AR bandwidth. However, reducing r_1 reduces the CP gain at low frequencies. Figure 3.10(c) shows that decreasing r_3 (i.e. moving the monopole SLAs to the center of the ground plane) increases the AR bandwidth while the lowest frequency in the AR bandwidth does not change. However, reducing r_3 makes it difficult to fabricate the antenna

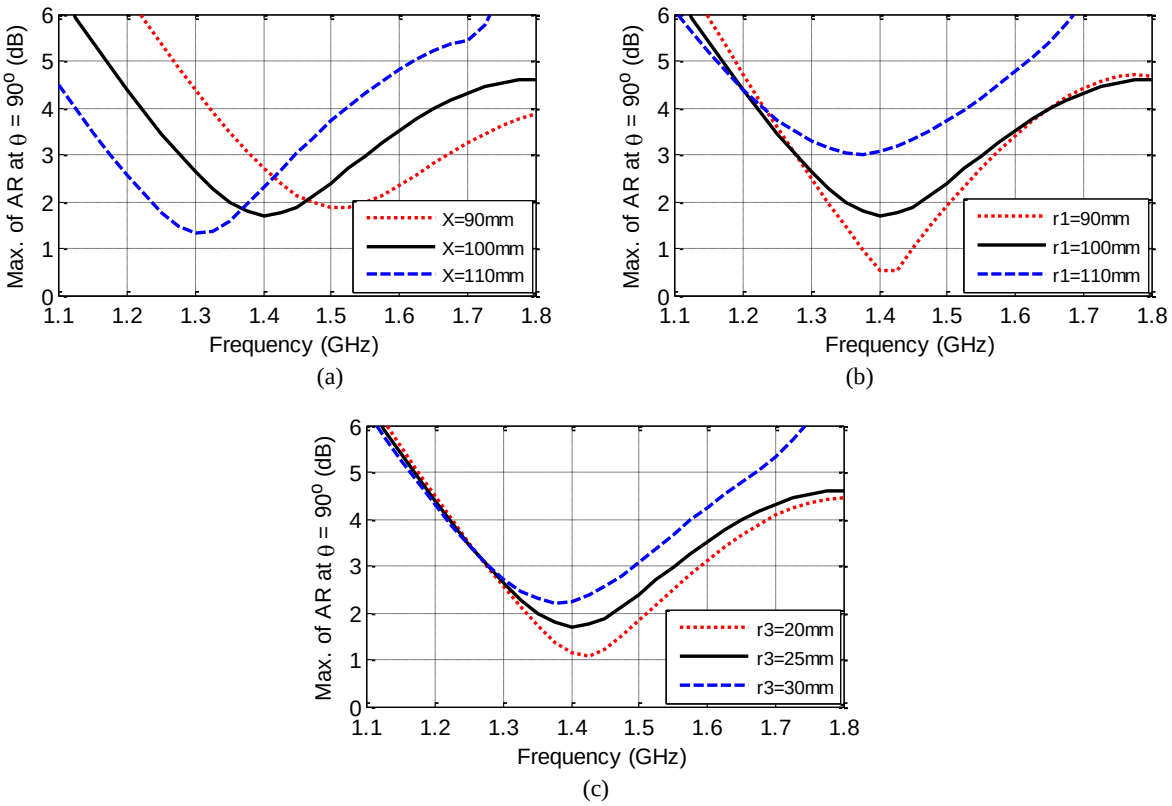

Figure 3.10. Maximum of AR in horizontal plane for different (a) $X = r_g = r_1 = r_2 + 40$ mm, (b) r_1, and (c) r_3 [16].

and the feed network. For a fixed value for r_3, increasing the frequency increases the electrical length between the adjacent monopole SLAs. In this case, study of the near-field electric field distribution shows that the excited field distribution deviates from the field distribution of the circular TE_{21} mode and thus degrades the AR at high frequencies. To excite circular TE_{21} mode in a wider bandwidth while keeping r_3 constant, in the next section, an additional monopole SLA is placed in between of each two adjacent SLAs in the original antenna with eight elements resulting a new structure with 16 monopole SLAs. With this structure, the distance between SLAs decreases and thus it can excite circular TE_{21} mode in a wider bandwidth.

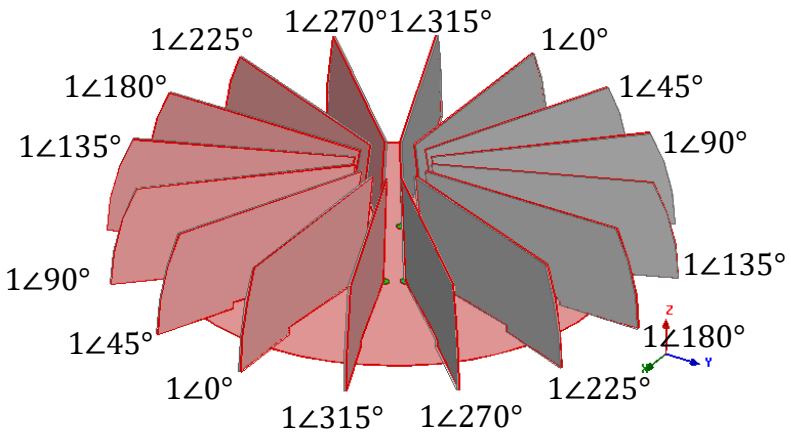

Figure 3.11. Structure of the CP antenna with 16 monopole SLAs. Excitation phases and amplitudes are for RHCP operation. RO4003 dielectric material is indicated by gray color [16].

3.5. Wideband Circularly Polarized Omnidirectional Antenna Using an Array of 16 Monopole SLAs

To increase the operation bandwidth of the proposed structure, another set of eight monopole SLAs is added to the antenna structure which is rotated by rotation angle of 22.5° with respect to the first eight monopole SLAs. As a result, the final structure is formed by 16 monopole SLAs. The angle between each two adjacent elements is 22.5°. All elements are coaxially fed by the same magnitude and the excitation phase increment of 45°. In this arrangement, the electrical length between elements decreases and the circular TE_{21} mode can be excited over a wider bandwidth. Figure 3.11 shows the structure of the antenna with 16 monopole SLAs. The geometry and dimensions of the ground plane and SLAs are the same as the previous section except that it is assumed that the ground plane and SLAs are realized by RO4003 substrate with the dielectric and copper thickness of 32 mil and 18 um, respectively. The copper on one side of the substrate forming monopole SLAs and the ground plane is completely removed. The excitation phases and amplitudes for RHCP operation are given in Figure 3.11.

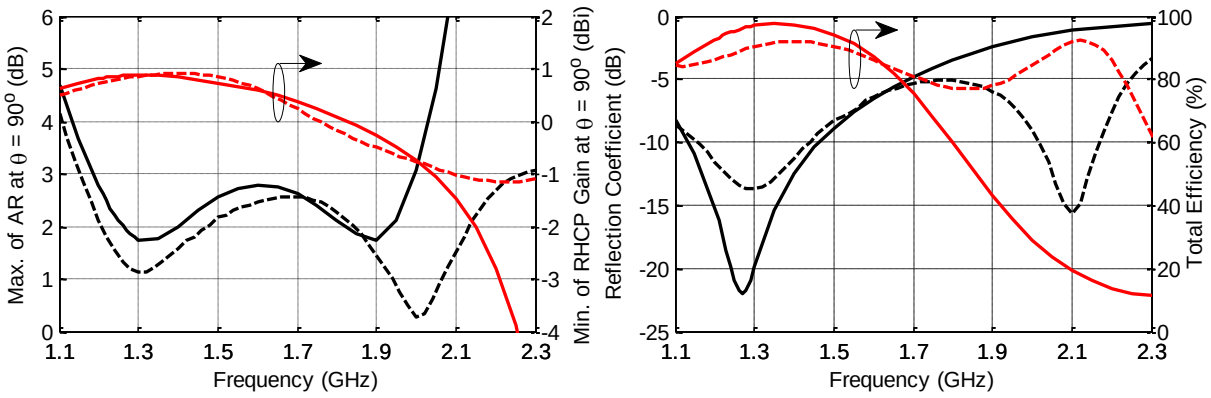

Figure 3.12. Simulation results for the antenna with 16 monopole SLAs shown in Figure 3.11 (solid lines) and Figure 3.13(b) (dashed lines) [16]. (a) Maximum of AR (dB) and minimum of RHCP gain (dBi) in horizontal plane. (b) Reflection coefficient (dB) and total efficiency.

Figure 3.12(a) shows the maximum value of AR and minimum of RHCP gain in the horizontal plane for the antenna in Figure 3.11. It is shown that the AR in less than 3 dB in the frequency range 1.2−2 GHz. Over the specified frequency range, the minimum RHCP gain in horizontal plane varies in the range -0.75−0.9 dBi. Figure 3.12(b) shows the reflection coefficient calculated by (3.11) and the total efficiency of the antenna. It can be observed that the reflection coefficient is less than -5 dB at frequencies larger than 1.7 GHz. This results in poor efficiency of the antenna at high frequencies. Simulation results show that variation of geometrical parameters does not have any significant effect on improvement of the reflection coefficient level at high frequencies and therefore, the monopole SLA structure must be modified. It is observed that reducing the height of the monopole SLA at the locations close to the feed can improve the reflection coefficient at high frequencies. Furthermore, introducing a gap to the monopole SLA structure, similar to the structure proposed in [61], can significantly improve the reflection coefficient. The modified structure for the monopole SLA is shown in Figure 3.13(a). In this figure, the location where SLA height is reduced is defined by r_4 and r_5 (measured from the center of the ground plane). The parameter h defines the amount that the height is reduced. The width and the

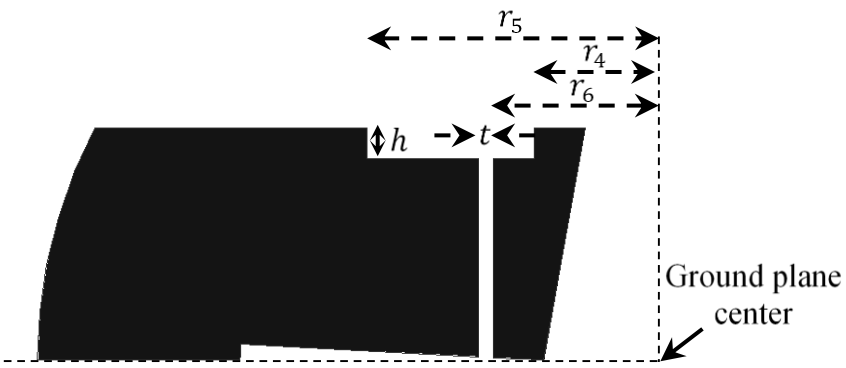

(a)

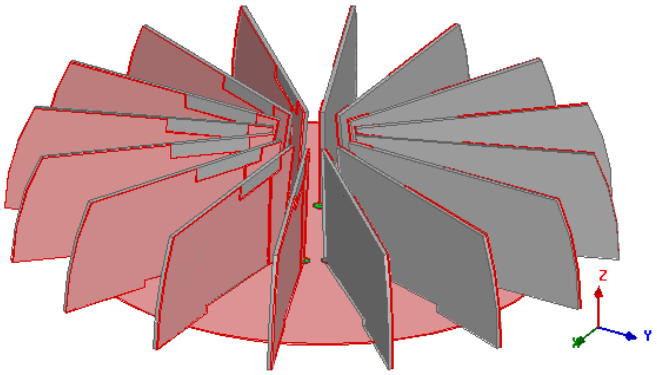

(b)

Figure 3.13. (a) Topology of modified monopole SLA. (b) Final structure of wideband CP omnidirectional antenna [16].

location of the gap are indicated by t and r_6, respectively. The chosen values for the parameters are: r_4 = 27 mm, r_5 = 60 mm, h = 6 mm, r_6 = 35 mm, and t = 0.5 mm. Other dimensions are the same as Figure 3.11. Figure 3.13(b) shows the final structure for the antenna. It is noted that in this structure, RO4003 dielectric has the same profile as Figure 3.11.

Simulation results for the new structure is presented in Figure 3.12 (indicated by dashed lines). It can be observed that the AR bandwidth and efficiency of the antenna are improved. According to Figure 3.12(a), in the range 1.15−2.24 GHz, AR is less than 3 dB and the minimum CP gain over horizontal plane varies in the range -1.16−0.9 dBi. Figure 3.12(b) shows improvement in reflection coefficient over the specified AR bandwidth. The minimum total efficiency over the AR bandwidth is 78%.

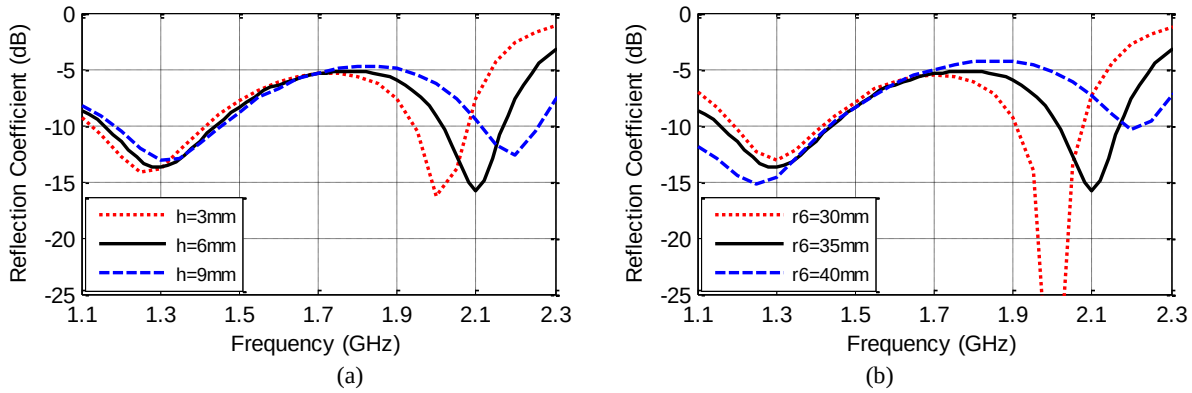

Figure 3.14. Reflection coefficient for the antenna in Figure 3.13(b) for different, (a) h and (b) r_6 [16].

For the antenna structure shown in Figure 3.13(b), the strongest coupling is between the adjacent ports with the maximum level of -7.1 dB over the band 1.11−2.17 GHz.

Parametric analyses show that the performance of the antenna is not sensitive to r_4, r_5, and t if they are varied in the range 24−30 mm, 50−70 mm, and 0.25−0.75 mm, respectively. Figure 3.14 shows that increasing h and r_6 improves the reflection coefficient at high frequencies. However, it degrades the reflection coefficient at the middle of the band.

3.6. Fabrication and Measurement Results for the 16-Element CP Antenna

An RHCP antenna with 16 modified monopole SLAs is fabricated and shown in Figure 3.15. The ground plane and monopole SLAs are fabricated using RO4003 substrate with dielectric and copper thickness of 32 mil and 18 um, respectively. To feed the monopole SLAs with the required amplitudes and phases, a feed network is designed and fabricated on the backside of the ground plane of SLAs as shown in Figure 3.16. Figure 3.16(b) shows the block diagram of the feed network which includes four stages of power dividers and 45° low-pass/high-pass (LP/HP) phase shifters. At the first stage, input power is divided by two using a Wilkinson power divider to feed the two identical sections on the right and left of the feed network in Figure 3.16(a). At the next stage, using a divider and four cascaded 45° phase shifters, the power is divided by two with

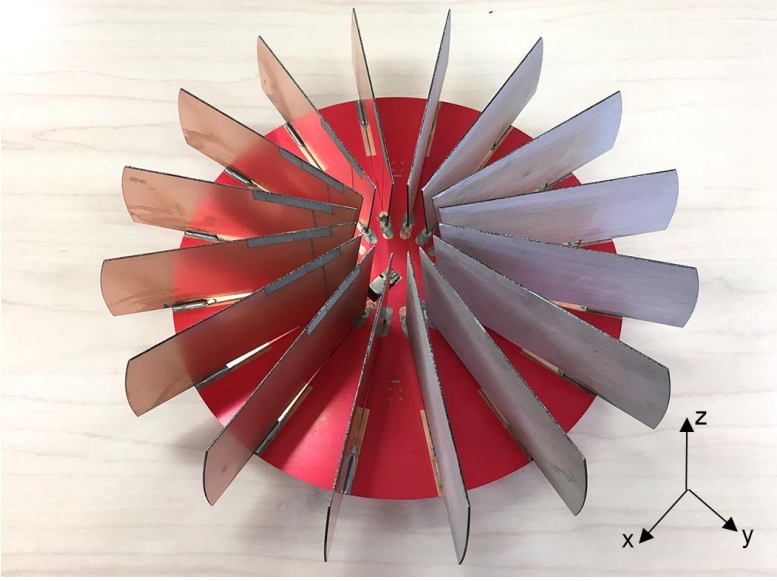

Figure 3.15. Fabricated CP antenna, the ground plane includes red solder mask [16].

180° phase difference between output signals. At the third stage, using a divider and two cascaded 45° phase shifters the power is divided by two with 90° phase difference between output signals. At this stage, the required signals for excitation of the antenna with eight monopole SLAs are obtained. At the final stage, the power is divided by two and then the output signals are applied to a 45° phase shifter. The output of the final stage is 16 signals that can be fed to the antenna with 16 monopole SLAs. The numbers at the output ports show the phases of the output signals assuming the phase of the first port from the bottom is 0°.

Each LP/HP phase shifter consists of two pi networks: 1) an LP network formed by one inductor (L_{LP}) and two identical capacitors (C_{LP}) and 2) an HP network formed by one capacitor (C_{HP}) and two identical inductors (L_{HP}). To design a 2ϕ (ϕ is a positive number) phase shifter matched to Z_0, the ABCD matrix of LP network is set equal to the ABCD matrix of a transmission line with characteristic impedance of Z_0 and phase of $-\phi$ at the center frequency of operation bandwidth (f_c) and the ABCD matrix of HP network is set equal to the ABCD matrix of a transmission line with characteristic impedance of Z_0 and phase of ϕ at f_c, resulting

$$L_{LP} = \frac{Z_0 \sin\phi}{2\pi f_c} \tag{3.13a}$$

$$C_{LP} = \frac{1 - \cos\phi}{2\pi f_c Z_0 \sin\phi} \tag{3.13b}$$

$$L_{HP} = \frac{Z_0 \sin\phi}{2\pi f_c (1 - \cos\phi)} \tag{3.13c}$$

$$C_{HP} = \frac{1}{2\pi f_c Z_0 \sin\phi} \tag{3.13d}$$

With values obtained by (3.13), the phase of the transmission coefficient at f_c for LP and HP networks is $-\phi$ and ϕ, respectively, resulting phase different of 2ϕ between the outputs of the two networks. Although the phase shifter is designed at f_c, the phase responses of LP and HP networks are linear and parallel around f_c, resulting approximately constant phase shift over a wide bandwidth.

For a 45° phase shifter matched to 50 Ω, setting ϕ = 22.5° in (3.13) at 1.6 GHz results L_{LP} = 1.9 nH, C_{LP} = 0.4 pF, L_{HP} = 25 nH, and C_{HP} = 5.2 pF. The phase shifter is fabricated using high self-resonant frequency inductors. With non-ideal inductors and capacitors, the obtained values for components must be tuned for best phase and insertion loss response within the operation bandwidth. In the fabricated feed network, L_{LP} = 1.8 nH (Coilcraft 0402CS-1N8XGLU), C_{LP} = 0.4 pF, L_{HP} = 24 nH (Coilcraft 0402HP-23NXGLU), and C_{HP} = 5.6 pF. Figure 3.16(c) shows the measured response of the 45° phase shifter. According to the results, maximum deviation of the phase shift (phase difference between the outputs of LP and HP networks) from 45° is 1.1° in the range 1.2−2 GHz. The insertion loss for both networks is less than 0.08 dB with the maximum difference of 0.02 dB over the band 1.2−2 GHz.

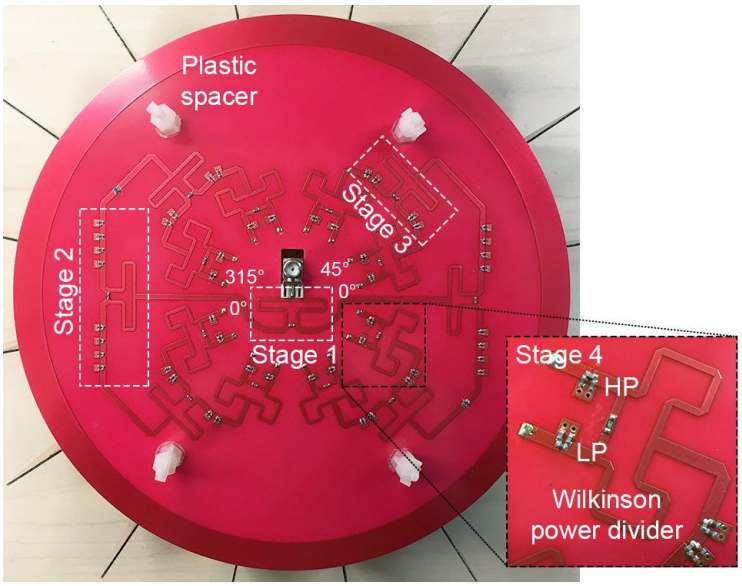

(a)

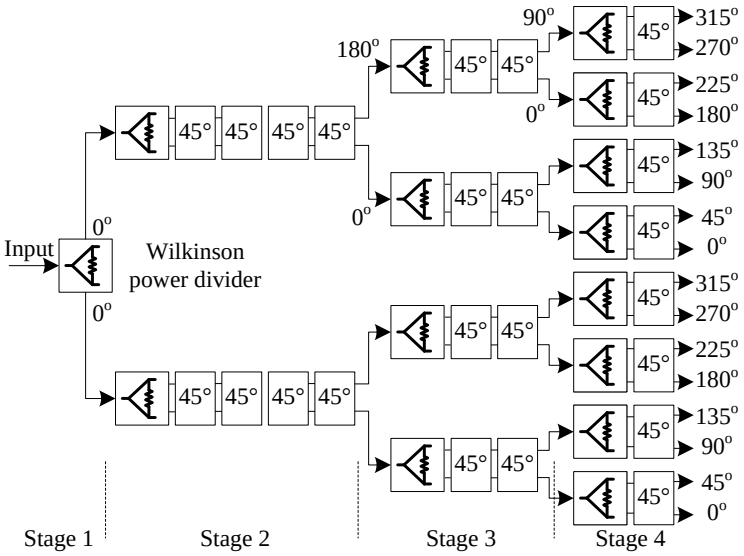

(b)

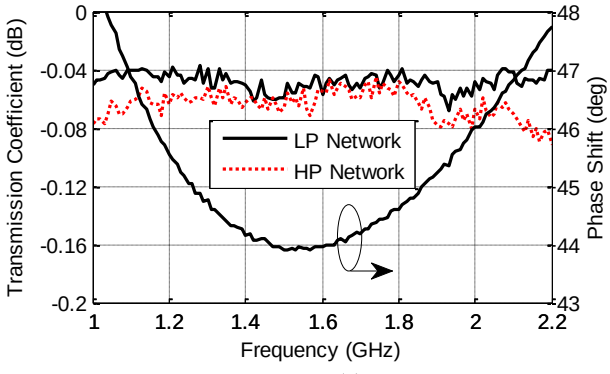

(c)

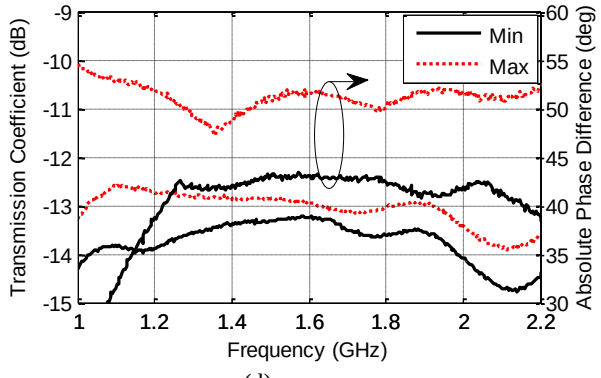

(d)

Figure 3.16. (a) Fabricated feed network (with red solder mask). (b) Block diagram of the feed network. (c) Measurement results for the 45° phase shifter. (d) Measurement results for the fabricated feed network [16].

The transmission coefficient between the input port and each of 16 output ports of the fabricated feed network is measured using a vector network analyzer while the other ports are terminated with 50 Ω load. Figure 3.16(d) shows the measured response of the feed network. According to the results, in the range 1.2−2 GHz, the variation range for the amplitude of the transmission coefficient is -14−-12.7 dB and the variation range for the absolute phase difference between adjacent ports is 38°−52°.

To show the effect of feed network phase and amplitude error on the AR performance of the antenna Monte Carlo simulations have be done at 1.7 GHz (where the antenna shown in Figure 3.13(b) has the highest AR according to the simulation results in Figure 3.12) and at 1.3 GHz and 2 GHz (where the antenna has low AR values). The results are shown in Figure 3.17. For each pair of maximum phase difference and maximum amplitude error, the ideal excitation signal for port n (n = 1, 2, …, 16) which is $P_n = 1\angle(n-1)45°$ is replaced by $P_n = \alpha_n\angle[(n-1)45°+\beta_n]$, where, α_n is a random value uniformly distributed in the range [0 maximum amplitude error] and β_n is a random value uniformly distributed in the range [-maximum phase difference/2 +maximum phase difference/2] resulting the maximum possible phase difference error of "maximum phase difference" between adjacent ports. At each point in Figure 3.17, AR is calculated over horizontal plane for 1000 set of randomly generated values for α_n and β_n and the maximum AR value is shown Figure 3.17. According to Figure 3.17(a) and Figure 3.17(c), the maximum of AR is less than 3 dB at 1.3 GHz and 2 GHz for maximum phase difference error in the range 0−10° and maximum amplitude error in the range 0−1 dB. According to Figure 3.17(b), for the maximum phase difference error = 6° and maximum amplitude error = 0.4 dB (the errors that the feed network shows at 1.7 GHz), the maximum AR is 3.1 dB. However, in the histogram plot of maximum values of AR over horizontal plane shown in Figure 3.17(d), it can be observed that in majority of

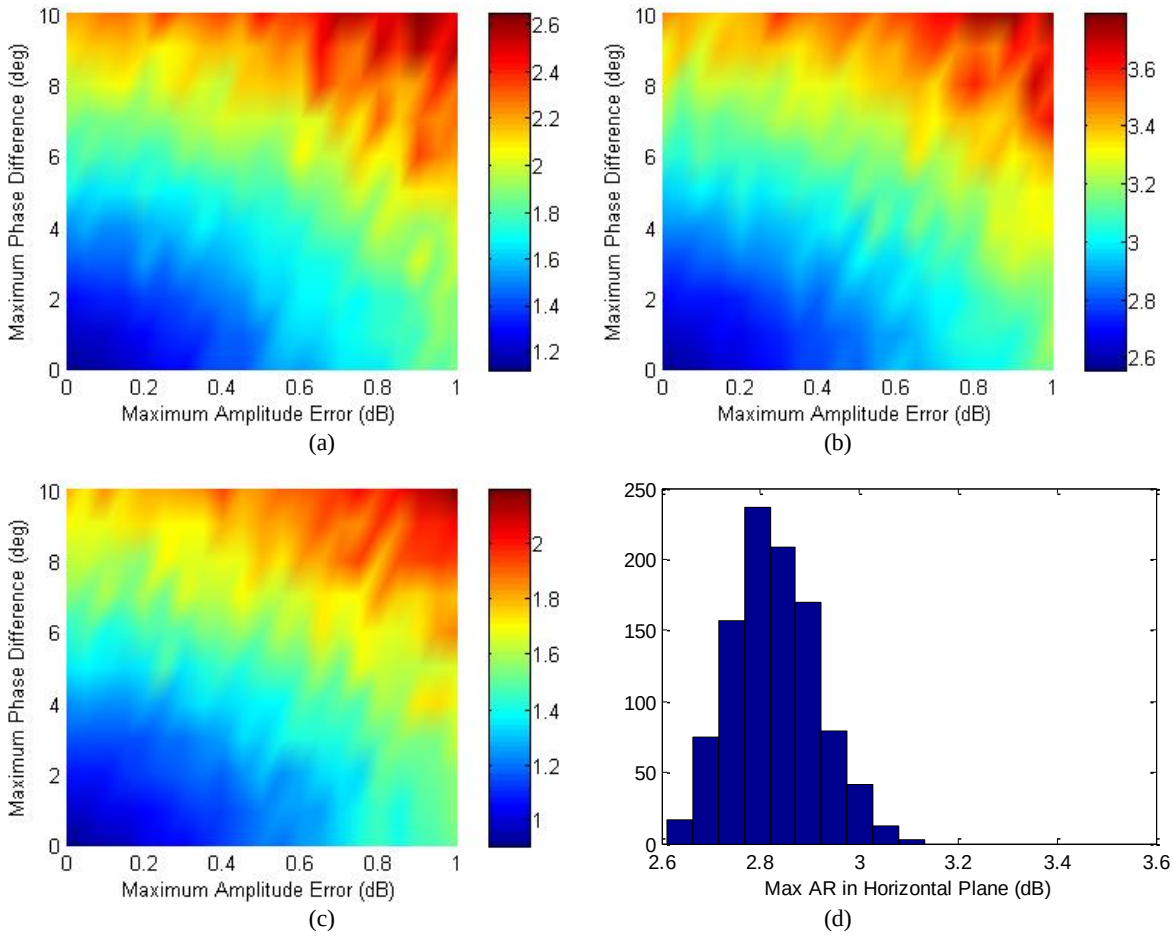

Figure 3.17. Maximum of AR over horizontal plane among 1000 different runs at (a) 1.3 GHz, (b) 1.7 GHz, and (c) 2 GHz. (d) Histogram plot of maximum of AR over horizontal plane for 1000 runs at 1.7 GHz and for maximum phase difference error of 6° and maximum amplitude error of 0.4 dB.

cases the AR is less than 3 dB. The results confirm that with the designed feed network, obtaining a wide AR bandwidth is possible.

The numbers at the output ports in Figure 3.16(b) also shows the relative phases of the reflected signals from the ports. It can be shown that the phase difference between reflected signals at the output ports of the divider at the third stage is 180° and thus the reflected signals are dissipated at the power divider's resistor and are not transferred to the input port or output ports. In this case, the reflection coefficient seen from the antenna ports is not translated to the reflection

coefficient seen from the input port of the feed network but it reduces the total efficiency of the antenna to the values shown in Figure 3.12(b) (considering no loss for the feed network).

The antenna is measured inside the anechoic chamber of the University of Michigan. Response of the antenna (phase and amplitude) to vertical and horizontal polarizations are measured separately in horizontal plane using a linearly polarized horn antenna and the results are combined to calculate AR and CP gains. The coordinate system used in measurements is shown in Figure 3.15.

Figure 3.18 shows the reflection coefficient of the fabricated antenna (measured from the input port of the feed network). It can be observed that the reflection coefficient is less than 10 dB over the band 1−2.02 GHz. The measured total efficiency of the antenna is also shown in Figure 3.18. The total efficiency is calculated by dividing average of the measured realized RHCP gain by average of the simulated RHCP directivity over the horizontal plane. The minimum total efficiency is 63% over the band 1.1−2.2 GHz. The reduction in measured total efficiency comparing to the simulated total efficiency in Figure 3.12(b) is due to the feed network loss. According to Figure 3.16(d), the loss for the feed network (deviation from the ideal value -12 dB) varies in the range 0.7−2 dB over the band 1.2−2 GHz. Using a substrate with a lower loss can improve the total efficiency of the antenna.

Figure 3.19(a) shows the average and maximum of the measured and simulated AR over horizontal plane versus frequency. Figure 3.19(b) shows the measured AR over horizontal plane and frequency. In measurement results, the average of AR is less than 3 dB over the band 1.11−2.17 GHz (64% bandwidth). Due to the feed network amplitude and phase errors, at a few points within the range 1.2−2 GHz, the measured AR is more than 3 dB according to Figure 3.19(b) but over the band 1.11−2.06, its maximum value is less than 3.3 dB (Figure 3.19(a)). Considering

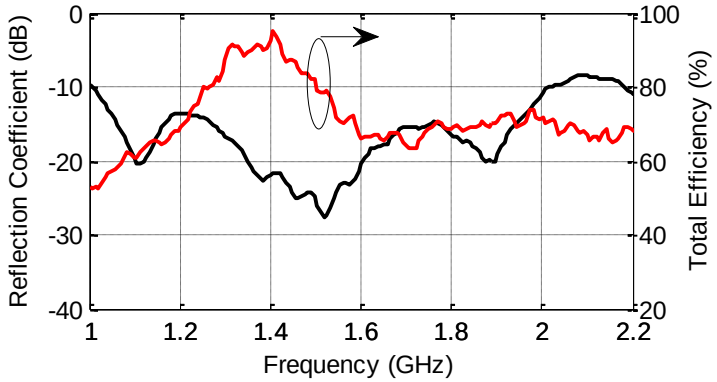

Figure 3.18. Measured reflection coefficient and total efficiency [16].

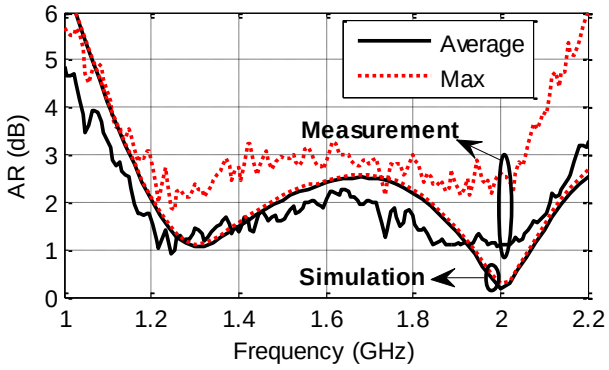

(a)

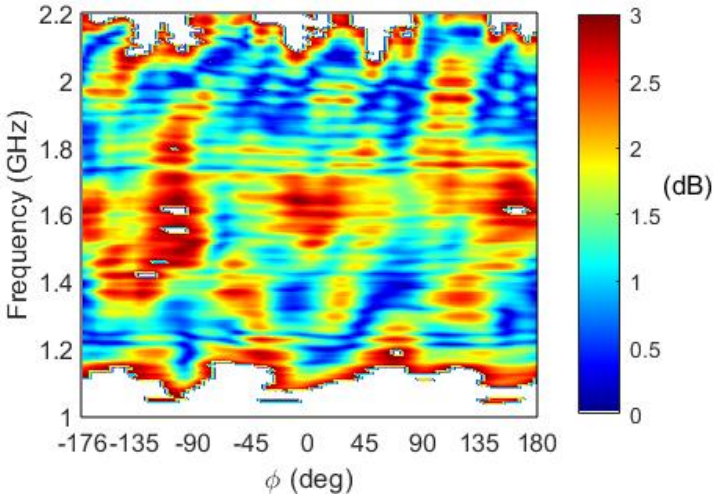

(b)

Figure 3.19. (a) Average and maximum of the measured and simulated AR over horizontal plane versus frequency [16]. (b) Measured AR in horizontal plane (θ = 90°) (white color indicates AR > 3 dB).

both 3-dB AR and 10-dB impedance bandwidth, the operation bandwidth of the antenna is in the range 1.11−2.02 GHz (58%).

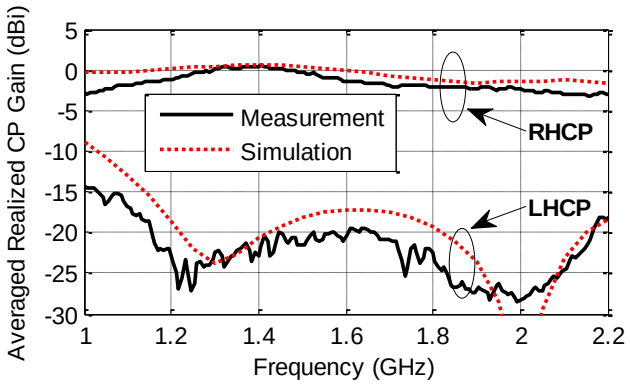

Figure 3.20. Measured and simulated average of realized RHCP and LHCP gains over horizontal plane [16].

Figure 3.20(b) shows the average of the measured and simulated realized RHCP and LHCP gains over horizontal plane versus frequency. Over the band 1.11−2.17 GHz (3-dB AR bandwidth), the measured and simulated RHCP realized gain varies within the range -2.9−0.52 dBi and -1.55−0.57 dBi, respectively. The difference between the measured and simulated gains is due to the fact that in simulations, loss of the feed network is not accounted for. Over the band 1.11−2.17 GHz, the measured averaged polarization isolation over the horizontal plane is greater than 18 dB.

The measured and simulated AR over horizontal plane are plotted in Figure 3.21 at 1.2, 1.6, and 2 GHz. The results show that the measured AR is less 3 dB over the horizontal plane. Figure 3.21(d) shows the simulated AR in elevation (ϕ = 0°) at 1.2, 1.6, and 2 GHz. According to the simulation results, AR is less than 3 dB for $|\theta| < 95°$.

The measured and simulated realized RHCP and LHCP gain patterns over horizontal plane are plotted in Figure 3.22 at 1.2, 1.6, and 2 GHz. The results show omnidirectional gain pattern for the antenna. The maximum measured and simulated gain variation in horizontal plane are 2 dB and 0.15 dB respectively. The difference in the measurement and simulation results is due to the measurement errors and also the errors in excitation phases and amplitudes of the elements. Figure 3.22(d) shows the simulated realized RHCP and LHCP gains in elevation (ϕ = 0°) at 1.2, 1.6, and

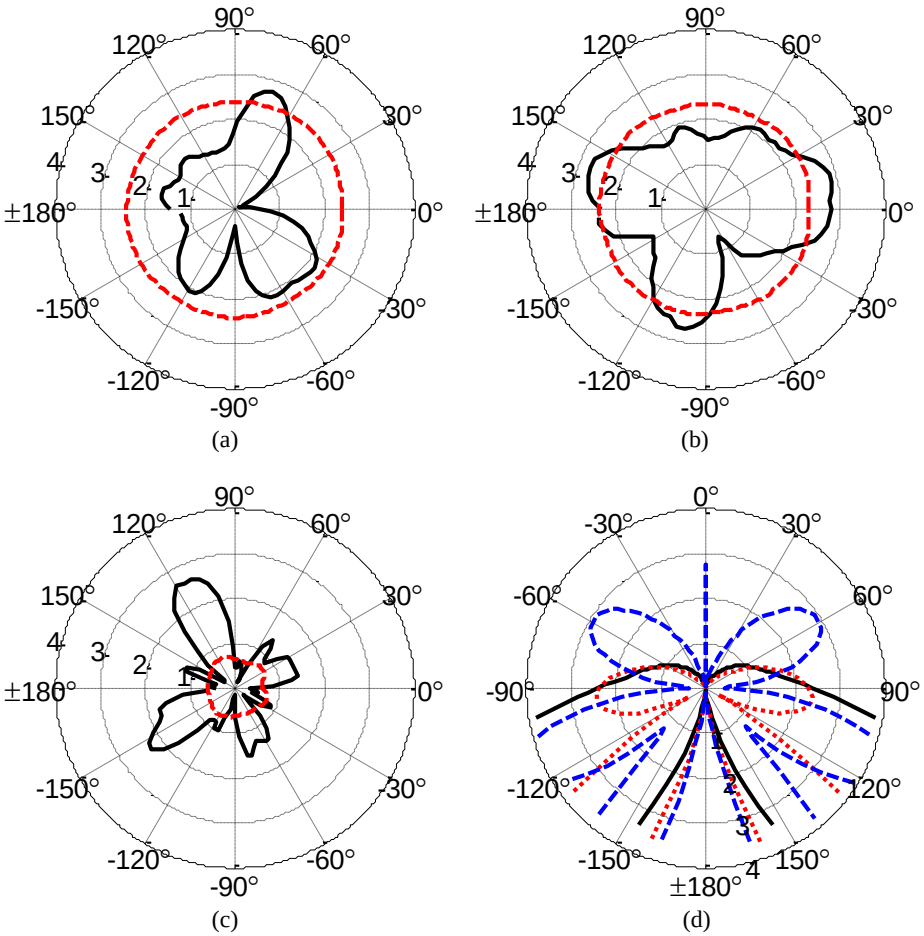

Figure 3.21. Axial ratio: measured (solid line) and simulated (dashed line without feed network) at θ = 90° and at 1.2 GHz (a), 1.6 GHz (b), and 2 GHz (c). Note that the AR is consistently below 3 dB and dissimilarity between the measured and simulated results are due to the feed network which is not included in the simulations. Also shown at (d) simulated AR at ϕ = 0° and at 1.2 GHz (solid line), 1.6 GHz (dotted line), and 2 GHz (dashed line) [16].

2 GHz. According to the simulation results, the maximum realized gain (excluding feed network loss) is 2 dBi at θ = 50°.

Table 3.1 compares the performance of different wideband circularly polarized omnidirectional antennas. The proposed antenna has the highest 3-dB AR and operation bandwidth. Diameter and total height of the antenna (excluding the connector) are 250 mm and 47 mm, respectively.

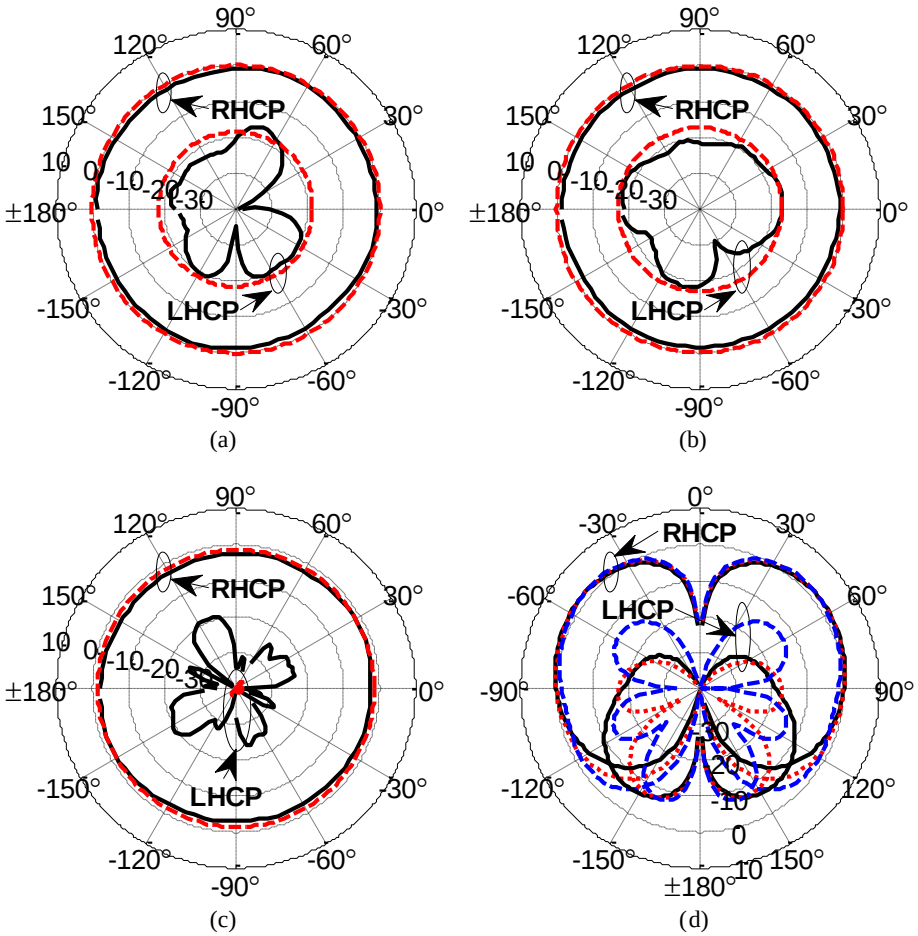

Figure 3.22. Gain pattern: Measured (solid line) and simulated (dashed line without feed network) realized CP gains at θ = 90° and at 1.2 GHz (a), 1.6 GHz (b), and at 2 GHz (c). Also shown are the simulated realized CP gains at ϕ = 0° and at 1.2 GHz (solid line), 1.6 GHz (dotted line), and 2 GHz (dashed line) [16].

Table 3.1. Performance comparison of wideband CP omnidirectional antennas.

Type of CP antenna	Center frequency (GHz)	3-dB AR bandwidth (%)	Operation bandwidth* (%)	Dimension $w\times l\times h$ (λ_0 is the wavelength at the center frequency)	Max realized gain (dBi) at specified elevation angle θ	Min efficiency (%)
This work	1.565	64 (Measured, Averaged at θ = 90°, Max 3.3 dB within operation bandwidth)	58	$1.3\lambda_0\times1.3\lambda_0\times0.25\lambda_0$	0.52 at θ = 90° 2** at θ = 50°	63 (78**)
Patch antenna with vortex slots and shorting vias [12]	2.845	57.9 (Measured, At θ = 125° and ϕ = 0°)	51.7	$0.85\lambda_0\times0.85\lambda_0\times0.14\lambda_0$	1 at θ = 125°	Not specified
Wideband vertically and horizontally polarized elements [13]	1.61	49.7 (Simulated)	49.7	Not specified	0 at θ = 90°	80
Monopole antenna and polarizer [3]	5.295	54.9 (Measured, At θ = 30° and ϕ = 0°)	41	$1.04\lambda_0\times1.04\lambda_0\times0.54\lambda_0$	6.3 at θ = 30°	Not specified
Array of rectangular loop elements [14]	2.075	41 (Measured)	41	$0.39\lambda_0\times0.39\lambda_0\times1.07\lambda_0$	~ 4.8 at θ = 90°	Not specified
Circular patch with slots operating at TM_{21} mode [15]	2.531	28.3 (Measured)	25.4	$2.63\lambda_0\times2.7\lambda_0\times0.084\lambda_0$	5.5 at θ = 33°	Not specified
Dielectric resonator with parasitic strips [2]	3.55	25.4 (Measured, At θ = 90° and ϕ = 0°)	22	$0.35\lambda_0\times0.35\lambda_0\times0.29\lambda_0$	1.48 at θ = 90°	84

* Measured 3-dB AR and 10-dB impedance bandwidth ** Excluding the feed network loss

3.7. Conclusion

A wideband circularly polarized omnidirectional antenna has been proposed for all-directions through-the-wall imaging radar application. The antenna operates based on excitation of a field distribution similar to circular TE_{21} mode over a wide bandwidth. It is shown that excitation of circular TE_{21} mode in the near-field of the antenna, produces a linearly polarized far-field electric field in horizontal plane whose polarization tilt angle varies as a function of azimuthal direction. Circular polarization is obtained by exciting two circular TE_{21} modes with excitation phase difference of 90° and spatial rotation angle difference of 45°. To excite the modes over a

wide bandwidth, an array of eight monopole SLAs was initially utilized. To improve the AR bandwidth of the antenna, the number of elements is increased to 16 elements. The final structure with 16 elements is fabricated and measured. In addition, a feed network for excitation of elements with the same amplitude and the required phases for RHCP operation is fabricated on the backside of the ground plane of the antenna. The diameter and total height of the antenna are 250 mm and 47 mm respectively.

The measured 3-dB AR and operation bandwidth (3-dB AR and 10-dB impedance bandwidth) are 64% (1.11−2.17 GHz) and 58% (1.11−2.02 GHz), respectively. The achieved AR and operation bandwidth are the highest among the proposed structures for omnidirectional circularly polarized antennas. The measured realized RHCP gain over horizontal plane is 0.52 dBi. Over the operation bandwidth, the minimum simulated total efficiency of the antenna excluding the feed network loss is 78%. The minimum measured total efficiency of the antenna including the feed network loss is 63%.

Chapter 4 All-Directions Through-the-Wall Imaging Using a Small Number of Moving Omnidirectional Bi-static FMCW Transceivers

4.1. Introduction

In Chapter 2, the idea of all-directions through-the-wall imaging has been presented. The focus of this chapter is on implementation of all-directions through-the-wall imaging and evaluation of its performance in real scenarios through laboratory and field measurements using a fabricated imaging system.

Bi-static configuration of transmitter and receivers in all-directions through-the-wall imaging requires synchronization between transmitter and receivers. It is shown that using frequency modulated continuous wave (FMCW) radar architecture, the synchronization can be performed with a simple method. To use the bi-static FMCW radar architecture, the imaging method presented in Chapter 2 is modified to be compatible with the new radar architecture.

In a bi-static imaging system, errors in synchronization and random and deterministic delays in transmitter and receiver circuits result in a distorted image. The presented imaging method can correct for these errors.

A complete bi-static FMCW radar system with wireless synchronization is designed and fabricated to demonstrate the performance of the all-directions through-the-wall imaging in real scenarios. A measurement is performed using the fabricated radar system and wideband linearly polarized (LP) omnidirectional blade antennas and wideband circularly polarized (CP) omnidirectional antennas presented in Chapter 3. It is shown that the circularly polarized antennas

enhance the imaging performance by reducing the direct signal from transmitter to receivers and better imaging of objects with large aspect ratio and arbitrary orientation.

4.2. Image Formation Technique Compatible with Bi-Static FMCW Radar Architecture

In this section, an image formation technique compatible with the bi-static FMCW radar architecture is introduced. Image formation is performed in two steps. The first step is aligning FMCW IF signals with respect to a reference point in the imaging area to correct for the errors in synchronization and random and deterministic delays in transmitter and receiver circuits. The second step is calculation of the image at each point in the imaging area.

4.2.1. Bi-static FMCW Signal Model and Correction for Errors in Synchronization and Delays in Circuits

In this section, an FMCW signal model and an error correction method for the signal received at nth sampling point are presented. The transmitter and nth sampling point are shown in Figure 4.1. For an FMCW transmitter, the transmitted signal ($s_x(t)$) is modeled by [64]

$$s_x(t) = e^{j2\pi f_0 t} e^{j\pi\gamma t^2} \qquad 0 < t < T, \tag{4.1}$$

where, f_0 is the start frequency, γ is the chirp rate, and T is the chirp duration. It is assumed that the amplitude of the chirp signal is equal to one. The frequency spectrum of the chirp signal described by (4.1) spans from f_0 to $f_0 + \gamma T$. The received signal from the point scatterer *P* (Figure 4.1) at the nth sampling point is modeled by

$$s_r(t) = \alpha e^{j2\pi f_0 (t - t_d)} e^{j\pi\gamma (t - t_d)^2}, \tag{4.2}$$

where α is the amplitude of the received signal which is, in general, a function of the range, scatterer radar cross section (RCS), and frequency. Here, it is assumed that α is independent of the

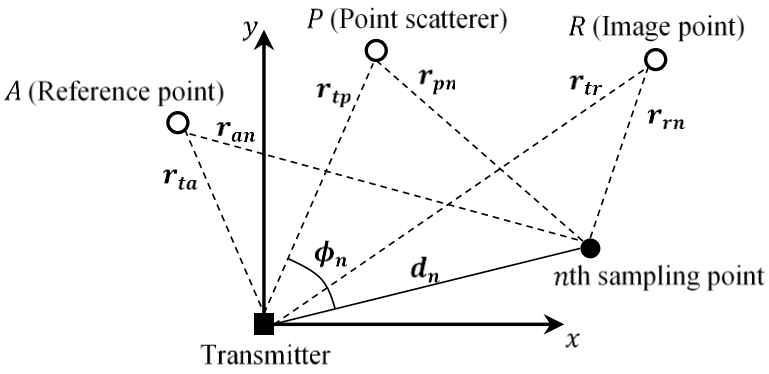

Figure 4.1. Transmitter and nth sampling point for image formation at point R [14].

frequency. In (4.2), t_d is the total delay in the received signal at the nth sampling point and has two components:

1. The delay that the signal experiences in its path from transmitter to P and from P to the receiver which is equal to $2R_t/c_0$ where c_0 is the speed of light in free space and R_t is the equivalent free space range which is equal to $(r_{tp}+r_{pn})/2$ (according to Figure 4.1, r_{tp} is the distance between the transmitter and the point scatterer P and r_{pn} is the distance between P and nth sampling point). Assuming transmitter located at the origin and the receiver at the nth sampling point, the slant range $(r_{tp} + r_{pn})$ to a point target is given by

$$r_{tp} + r_{pn} = r_{tp} + \sqrt{d_n^2 + r_{tp}^2 - 2d_n r_{tp}\cos(\phi_n)} \tag{4.3}$$

   where, d_n is the distance between the transmitter and nth sampling point and ϕ_n is the angle between the line passing through the transmitter and the scatterer P and the line passing through the transmitter and the nth sampling point.

2. The delay inside the transmitter and receiver RF circuits, interconnecting cables, and antennas. This delay is modeled by free space equivalent range of R_c and is equal to $2R_c/c_0$.

Considering the two components for t_d, (4.2) can be rewritten as

$$s_r(t) = \alpha e^{j2\pi f_0\left(t-\frac{2(R_t+R_c)}{c_0}\right)} e^{j\pi\gamma\left(t-\frac{2(R_t+R_c)}{c_0}\right)^2}. \quad (4.4)$$

At the receiver, the reference chirp signal ($S_{ref}(t)$) is modeled by:

$$s_{ref}(t) = e^{j2\pi f_0\left(t-\frac{2R_o}{c_0}\right)} e^{j\pi\gamma\left(t-\frac{2R_o}{c_0}\right)^2} \quad (4.5)$$

where, R_o is the equivalent free space range that models the delay (= $2R_o/c_0$) between the start of the chirp signals at the receiver and the transmitter. This delay is due to the synchronization error.

Filtered IF signal at the output of the receiver is

$$s_{IF}(t) = s_r^*(t)s_{ref}(t) = \alpha e^{j\frac{4\pi f_0}{c_0}(R_t+R_c-R_o)} e^{j\frac{4\pi\gamma}{c_0}\left(t-\frac{2R_o}{c_0}\right)(R_t+R_c-R_o)} e^{-j\frac{4\pi\gamma}{c_0^2}(R_t+R_c-R_o)^2}. \quad (4.6)$$

In (4.6), the first exponential is Doppler-frequency, the second exponential is range-frequency, and the third exponential is residual video phase (RVP). The received signal from the point *P* generates a peak in the frequency spectrum of the IF signal with the frequency at

$$f_P = \frac{2\gamma}{c_0}(R_t + R_c - R_o). \quad (4.7)$$

By calculating f_P for a known point *P* in the imaging area, the unknown $R_c - R_o$ can be determined. In a bi-static radar system with omnidirectional antennas, direct signal from transmitter to receiver produces a peak with the lowest frequency in the spectrum of the IF signal. The frequency of this peak (f_{direct}) is obtained from (4.7) while the point *P* is placed at the location of the transmitter (in this case r_{tp} = 0 and $r_{pn} = d_n$ reuslitng $R_t = d_n/2$). Knowing d_n and f_{direct}, $R_c - R_o$ is

$$R_c - R_o = \frac{c_0 f_{direct}}{2\gamma} - \frac{d_n}{2}. \quad (4.8)$$

In the following, the obtained $R_c - R_o$ is used to correct the synchronization errors and delays in RF circuits and antennas.

The IF signal at the output of the receiver is sampled using a high speed A/D. Assuming that A/D is set such that the sampling is started by the start of the chirp at the receiver, the time for the kth sample in A/D is

$$t_k = \frac{k}{F_s} + t_s + \frac{2R_o}{c_0}. \tag{4.9}$$

In (4.9), F_s is the sampling frequency and t_s models the difference between the start time for A/D sampling and start time for the chirp signal at the receiver. The sampled IF signal is represented by

$$s_{IF}(k) = \alpha e^{j\frac{4\pi f_0}{c_0}(R_t+R_c-R_o)} e^{j\frac{4\pi\gamma}{c_0}\left(\frac{k}{F_s}+t_s\right)(R_t+R_c-R_o)} e^{-j\frac{4\pi\gamma}{c_0^2}(R_t+R_c-R_o)^2}. \tag{4.10}$$

To compensate for the synchronization error, delays in RF circuits and antennas, and t_s, a reference point A in the imaging area is defined. The received signal from point A (s_a) is modeled by

$$s_a(k) = s_{IF}(k)|_{R_t=R_a,\ \alpha=1} = e^{j\frac{4\pi f_0}{c_0}(R_a+R_c-R_o)} e^{j\frac{4\pi\gamma}{c_0}\left(\frac{k}{F_s}+t_s\right)(R_a+R_c-R_o)} e^{-j\frac{4\pi\gamma}{c_0^2}(R_a+R_c-R_o)^2} \tag{4.11}$$

where, $R_a = (r_{ta} + r_{ap})/2$ (r_{ta} and r_{ap} are shown in Figure 4.1). In (4.11), t_s is unknown and must be determined before compensation. To determine t_s, $s_{IF}(k)$ is multiplied by $s_{a,0}^*(k) = s_a^*(k)|_{t_s=0}$

$s_{IF}(k)s_{a,0}^*(k)$

$$= \alpha e^{j\frac{4\pi f_0}{c_0}(R_t-R_a)} e^{j\frac{4\pi\gamma}{c_0}\left(\frac{k}{F_s}-\frac{2(R_a+R_c-R_o)}{c_0}\right)(R_t-R_a)} e^{j\frac{4\pi\gamma}{c_0}t_s(R_t+R_c-R_o)} e^{-j\frac{4\pi\gamma}{c_0^2}(R_t-R_a)^2} \tag{4.12}$$

According to the second exponential term in (4.12), a reflected signal from point A ($R_t = R_a$) produces a peak at zero frequency in the frequency spectrum of $s_{IF}s_{a,0}^*$. Transmitter location is a known point in the imaging area. Here, the transmitter location is selected as point A resulting $R_a = d_n/2$. In this case, the effect of the direct signal from transmitter to receiver is a peak at the zero

frequency in the frequency spectrum of $s_{IF}s_{a,0}^{*}$. In (4.12), the phase of $s_{IF}s_{a,0}^{*}$ at $R_t = R_a$ (= the phase of FFT for $s_{IF}s_{a,0}^{*}$ at zero frequency) is

$$\phi_0 = \frac{4\pi\gamma}{c_0} t_s(R_a + R_c - R_o). \tag{4.13}$$

and consequently, t_s can be obtained from

$$t_s = \frac{\phi_0 c_0}{4\pi\gamma} \frac{1}{(R_a + R_c - R_o)} . \tag{4.14}$$

After calculating t_s, the compensated s_{IF} (denoted by $s_{IF,c}$) is obtained by multiplying s_{IF} by s_a^*

$$s_{IF,c}(k) = s_{IF}(k)s_a^*(k)$$

$$= \alpha e^{j\frac{4\pi f_0}{c_0}(R_t - R_a)} e^{j\frac{4\pi\gamma}{c_0}\left(\frac{k}{F_s} - \frac{2(R_a + R_c - R_o)}{c_0}\right)(R_t - R_a)} e^{j\frac{4\pi\gamma}{c_0}t_s(R_t - R_a)} e^{-j\frac{4\pi\gamma}{c_0^2}(R_t - R_a)^2} \tag{4.15}$$

According to (4.15), for a signal received from the reference point A ($R_t = R_a$), the phase and frequency of the peak are zero.

The error correction process at each sampling point can be summarized as

1. Calculating FFT of the samples of IF signal (s_{IF}) at positive frequencies;
2. Determining the frequency of the first peak (f_{direct}) and using (4.8) to calculate $R_c - R_o$;
3. Setting $R_a = d_n/2$ and using $R_c - R_o$ from step 2 to calculate $s_{IF}s_{a,0}^{*}$;
4. Calculating phase of the FFT for the samples of $s_{IF}s_{a,0}^{*}$ at zero frequency (ϕ_0) and then using (4.14) to find t_s;
5. Calculating corrected IF signal ($s_{IF,c}$) using (4.15);
6. Using the obtained $R_c - R_o$, t_s, and $s_{IF,c}$ at each sampling point for image formation.

It should be noted that in reality, IF signal is real and equal to the real part of (4.6). However, since in error correction and image formation, the FFT of the IF signal at positive frequencies is used, both the real and complex IF signals produce the same results.

The RVP term in $s_{IF,c}$ (last exponential term in (4.15)) produces an unwanted range dependent phase shift. It can be removed by the simple filtering method presented in [64]. However, RVP is not removed here, since with $\gamma = 1.5\times10^{13}$ Hz/s in the fabricated radar system, phase of RVP is less than 5° for ranges up to 6 m.

A sample of the IF signal before and after correction is shown in Figure 4.2. For correction, the reference point (A) is set at the transmitter location. It can be observed that the first peak which is due to the signal received from point A (the direct signal from the transmitter to receiver), is shifted to zero frequency in the corrected signal.

4.2.2. Image Formation

In image formation, it is assumed that the transmitter and receiver remain stationary during signal transmission and reception. $R_c - R_o$, $s_{IF,c}$, and t_s that are calculated at the nth sampling point are denoted by $R_{c,n} - R_{o,n}$, $s_{IF,c,n}$, and $t_{s,n}$, respectively. The image at point R, $I(R)$, is calculated by time domain correlation method described in [65]

$$I(R) = \sum_{n=1}^{N} \int_{0}^{T} s_{IF.c,n}(t) s_{c,n}^{*}(t) dt \tag{4.16}$$

where N is the number of sampling points and $s_{c,n}(t)$ is

$$s_{c,n}(t) = e^{j\frac{4\pi f_0}{c_0}\left(R_{t,n}-R_{a,n}\right)} e^{j\frac{4\pi\gamma}{c_0}\left(t-\frac{2\left(R_{a,n}+R_{c,n}-R_{o,n}\right)}{c_0}\right)\left(R_{t,n}-R_{a,n}\right)} e^{j\frac{4\pi\gamma}{c_0}t_{s,n}\left(R_{t,n}-R_{a,n}\right)}. \tag{4.17}$$

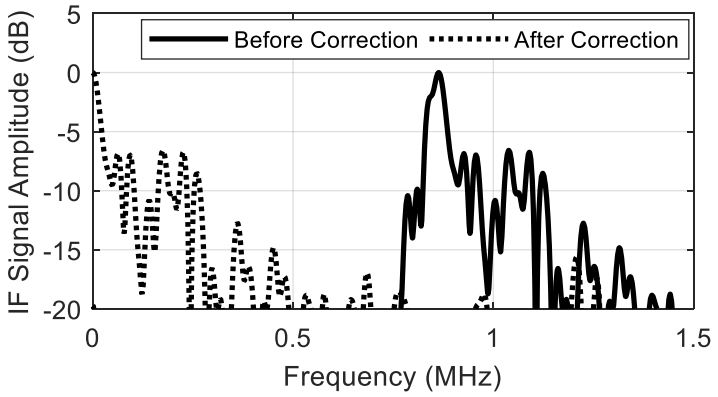

Figure 4.2. A sample of IF signal before and after correction. Setting reference point *A* at the transmitter location, the first peak which is due to the signal received from point *A* (direct signal from the transmitter to the receiver), is shifted to zero frequency in the corrected signal [14].

In (4.17), $R_{a,n} = d_n/2$ (d_n is the distance between the transmitter and the nth receiving point) and $R_{t,n} = (r_{tr} + r_{rn})/2$, where r_{tr} is the distance between transmitter and point R and r_{rn} is the distance between point R and nth sampling point, as shown in Figure 4.1.

If the transmitter and receivers are stationary during each measurement, the integral in (4.16) can be represented by FFT of $s_{IF,c,n}$ ($S_{IF,c,n}$) at the frequency of $2\gamma(R_{t,n} - R_{a,n})/c_0$, which results in a more computationally efficient back-projection algorithm [65]

$$I(R) = \sum_{n=1}^{N} \left(e^{-j\frac{4\pi}{c_0}\left(f_0 - \frac{2\gamma\left(R_{a,n}+R_{c,n}-R_{o,n}\right)}{c_0}\right)\left(R_{t,n}-R_{a,n}\right)} \times e^{-j\frac{4\pi\gamma}{c_0}t_{s,n}\left(R_{t,n}-R_{a,n}\right)} S_{IF,c,n}\left(\frac{2\gamma\left(R_{t,n}-R_{a,n}\right)}{c_0}\right)\right). \quad (4.18)$$

Equation (4.18) is used to calculate the image in all the points R within the imaging area.

A MATLAB code for all-directions through-the-wall imaging using bi-static FMCW transceivers is provided in Appendix A.

4.3. Bi-static FMCW Radar System Realizing All-Directions Through-the-Wall Imaging

To test the performance of the proposed all-directions through-the-wall imaging method in real scenarios, a bi-static FMCW radar system has been designed, fabricated, and tested. The block diagram of the transmitter and receiver is shown in Figure 4.3. In transmitter and receiver, the constituent parts of the chirp generator are a direct digital synthesizer (DDS), a PLL, and a wideband RF VCO. According to Figure 4.3(a), DDS generates a low frequency chirp signal in the range 50−82 MHz. This chirp signal is fed to the reference input of a wideband phase/frequency detector (PFD). The output of PFD is connected to a wideband loop filter whose output controls the VCO frequency. The frequency of the signal at the VCO output is divided by 24 and is fed to the RF input of PFD. In this case, the frequency of the chirp signal generated by DDS is multiplied by 24, resulting in a chirp signal with the frequency spectrum spans from 1.2 GHz to 1.968 GHz. The total sweep time for the chirp signal (T) is 51.2 μs resulting in a chirp rate (γ) of 1.5×10^{13} Hz/s. The operation bandwidth of the system (768 MHz) results in a theoretical range resolution of 19.5 cm. With the specified chirp rate, each 1 cm increase in the range of the target, increases frequency of the resulting peak in spectrum of the IF signal by 1 kHz. For two objects with separation of one range resolution, the frequency difference in the IF signal is 19.5 kHz. To resolve the images of two targets with a separation of the range resolution in the range direction, the chirp generator must have a low phase noise at 19.5 kHz offset. The measurement results show that at all frequencies within the operation band, the phase noise is less than -100 dBc/Hz at 19.5 kHz offset. Measured phase noise values at 1.2 and 2 GHz are shown in Table 4.1.

As shown in Figure 4.3(b), IF signal at the output of the receiver is connected to a high-speed A/D (100 MSamples/s). The samples of the IF signal are stored in a high-speed FIFO and

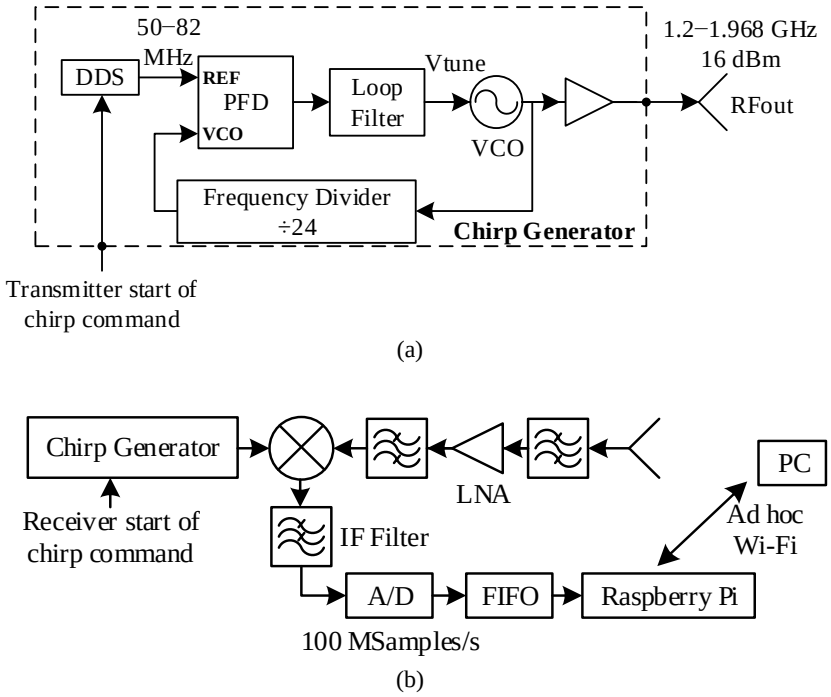

Figure 4.3. Block diagram of the fabricated radar [14]. (a) Chirp generator and transmitter. (b) Receiver.

Table 4.1. Phase noise of the fabricated radar

f_c (GHz)	Phase noise at 19.5 kHz offset (dBc/Hz)	Phase noise at 100 kHz offset (dBc/Hz)
1.2 GHz	-101	-112
2 GHz	-100	-106

are subsequently read by a Raspberry Pi board and transferred wirelessly to a PC (for image formation) via an ad-hoc Wi-Fi network.

The selected A/D oversamples the IF signal. Assuming a maximum target range of 10 m and the maximum synchronization error which is mentioned later in this section, the IF signal bandwidth is less than 10 MHz and therefore A/D sampling rate can be decreased.

Start time for the chirp signal at the transmitter and receiver(s) and start of the sampling in A/D are controlled by a wireless synchronization circuit. A simple solution for synchronization is using a digital transceiver for sending and receiving the start of chirp command. However due to the random delays in the digital transceiver circuits, the synchronization error largely varies in time. For a 300 kb/s transceiver, the maximum measured synchronization error is 400 ns. In the

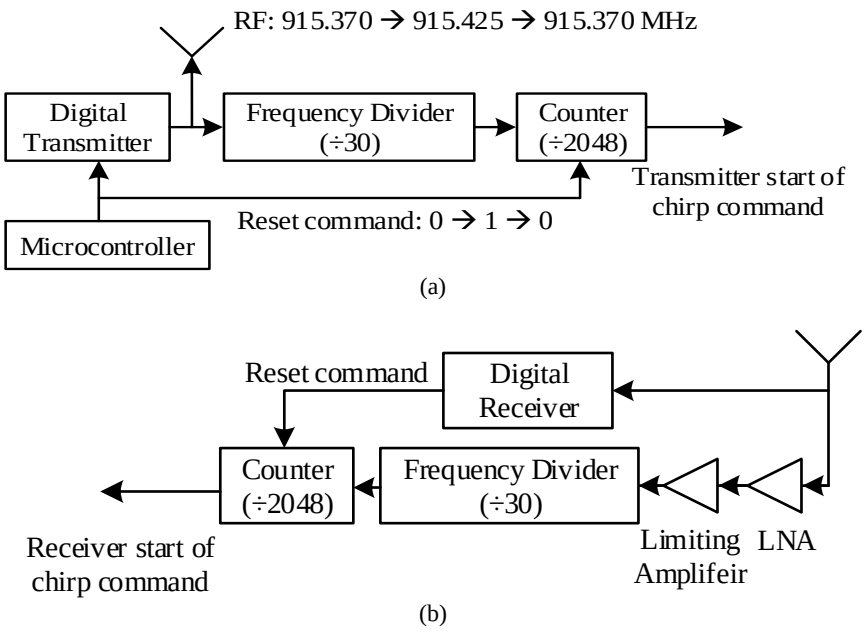

Figure 4.4. Block diagram of the synchronization circuit at (a) transmitter and (b) receiver [14].

fabricated radar system, for a fixed transmitter, receiver, and target, this error shifts the spectrum of IF signal randomly by up to 6 MHz in successive chirp sweeps. This large variation in the spectrum of IF signal reduces the coherency and image quality even if all the synchronization errors are corrected since the response of the mixer and IF filter is not completely the same over the operation band. For the best results, this error must be kept constant for successive chirp sweeps.

Figure 4.4 shows the block diagram of the proposed synchronization circuit in transmitter and receiver. The digital transmitter (FSK modulator) transmits a CW signal with the frequency of f_1 (915.370 MHz) for bit 0 or f_2 (915.425 MHz) for bit 1. This signal is received at the receiver. The frequency of the signal is reduced by cascaded frequency dividers and counters at both the transmitter and receiver. The resulting low frequency signal is used as a command for start of chirp signal. In this configuration, any change in the frequency of the transmitted signal due to the instability of the oscillator in the digital transmitter and change of the input data has the same effect

on the generated low frequency signals at both transmitter and receiver. After power up, a large delay exists between the start of the chirp commands at the output of the counters. The reason is that the counters at the receiver, receive the CW signal with a delay equal to the free space path delay between the transmitter and the receiver. To correct this error, a microcontroller is used at transmitter to directly reset the counters at the transmitter and also reset the counters at the receiver via a wireless channel provided by the digital transmitter and receiver. After the reset command, the delay between the start of the chirp signal at transmitter and receiver decreases and remains constant in successive chirp sweeps. This constant delay is due to the delays in the digital transceiver circuits and as mentioned previously, it is less than 400 ns.

It should be noted that the synchronization circuit must be adjusted such that the chirp signal at the receiver starts before receiving the first signal from the transmitter. Otherwise both the near-range and far-range targets will be imaged as near-range targets. The proper timing can be achieved by imposing a time difference in sending the reset commands to the counters in the transmitter and receiver.

Figure 4.5 shows different parts of the fabricated radar which is used for the measurements presented in the next section. The antennas used in measurements are wideband LP omnidirectional blade antennas and wideband CP omnidirectional antennas presented in Chapter 3. The antennas are shown in Figure 4.5(d). The maximum gains for LP and CP antennas over the horizontal plane and the band 1.2−1.968 GHz are 2.1 and 0.52 dBi, respectively.

To evaluate performance of each fabricated radar board, a monostatic measurement has been performed inside the anechoic chamber and the results have been compared to the results obtained by a vector network analyzer (VNA). For monostatic measurements, the RF output of the radar board is divided by a two-way power divider. One output is directly connected to the LO

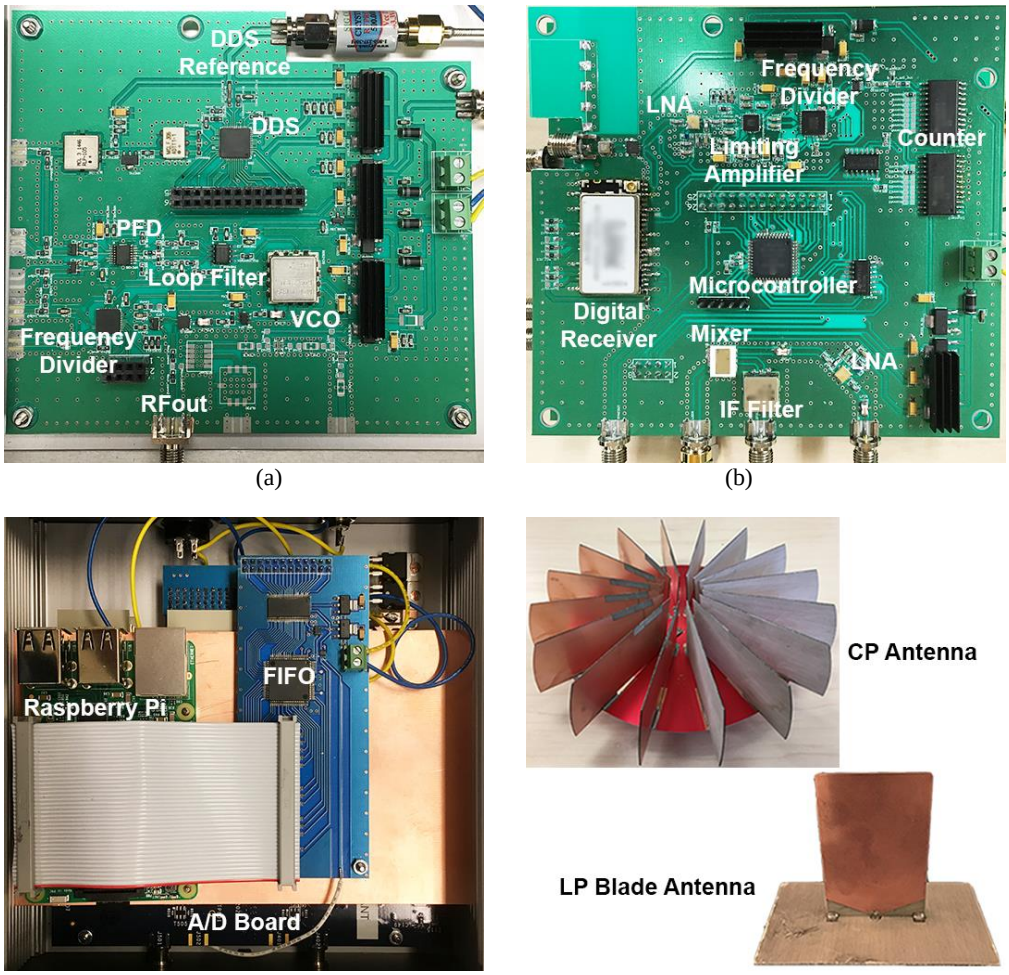

Figure 4.5. Fabricated radar system [14]. (a) Chirp generator/FMCW transmitter. (b) Frequency mixer and synchronization board in receiver. (c) A/D module. (d) Wideband CP and LP antennas.

input of the mixer and the second output is connected to a high gain horn antenna. The RF input of the radar board is connected to an L-band waveguide transition which acts as a low gain receiving antenna. The target is a metallic sphere with the diameter of 35 cm. The distance between the target and antenna apertures is approximately 14.5 m. The RCS of the target is -9.5 dBsm at the center frequency (1.6 GHz). The target is shown in Figure 4.6(a).

Figure 4.6(b) shows the FFT of the IF signal for three cases: 1) object is not present (Background), 2) object is present (Sphere), and 3) background signal is subtracted from the signal measured in the second case (Sphere - Background). In these results, the IF frequency is converted

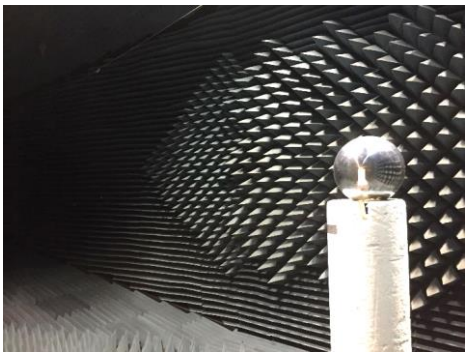

(a)

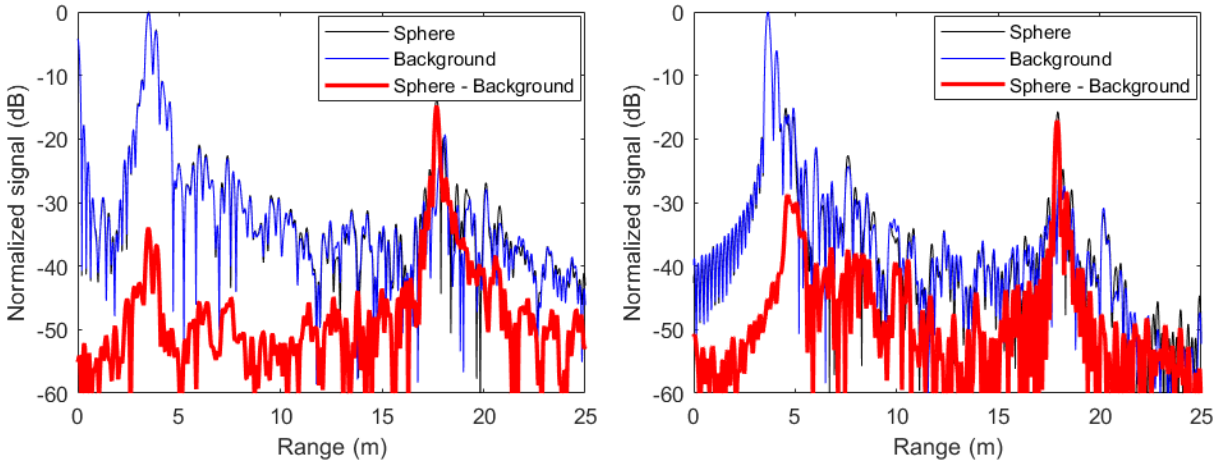

(b) (c)

Figure 4.6. Monostatic measurement results inside the anechoic chamber. (a) Metallic sphere (target) inside the chamber. (b) Fabricated radar (FFT of the IF signal). (b) VNA (IFFT of 801 frequency samples over the band 1.2–2 GHz).

to the range knowing that each 1 cm increase in range in equivalent to 1 kHz increase in the IF frequency. The first peak in background and sphere signals are due to the direct coupling from the transmitter to receiver and its location indicates the antenna apertures. This peak is located at the range 3.487 m. The peak located at the range 17.68 m (in sphere signal) is due to the metallic sphere. It can be observed that this peak is not present in Background signal. With these two measurements, the range of the sphere is calculated as 17.68 – 3.487 = 14.193 m. The third peak (at the range of 20 m) in both Background and Sphere signals is due to the reflection from the end of the chamber. The first and third peaks in the background subtraction result are attenuated since they are present in both sphere and background signals. In background subtraction result, the peak with the highest amplitude indicates the location of the target. Figure 4.6(b) is the measurement

result for one radar board. For the second fabricated radar board, the monostatic measurement results are similar to Figure 4.6(b). Figure 4.6(c) shows the image of target obtained by applying inverse Fourier transform to 801 frequency samples over the band 1.2−2 GHz measured by a VNA. In Figure 4.6(c), the antennas apertures are located at 3.65 m and the target is located at 17.91 m and therefore the range of the target is 17.91 – 3.65 = 14.26 m which is very close to the result obtained by the fabricated radar. Comparing the background subtraction results in Figure 4.6(a) and Figure 4.6(b) shows that the results obtained by the fabricated radar is very similar to the results obtained by VNA.

To evaluate performance of fabricated radar in through-the-wall imaging, a laboratory test has been performed using the fabricated radar. Figure 4.7(a) shows the configuration of the antennas. Transmitting and receiving antennas are two double ridged horn antennas. The position of the transmitting antenna is fixed whereas the receiving antenna is moved on concentric circles using an X-Y table as shown in Figure 4.7(a). With this configuration for antennas, the measurement is bi-static. In this measurement, both chirp signals at the transmitter and FMCW receiver are generated by a single board.

Figure 4.7(b) shows the measurement setup. The wall is formed by a layer of drywall and a layer of wood with separation of 20 cm. A metallic sphere with diameter of 35 cm is located behind the wall. The image is obtained by 51 samples of the scattered field. The sampling points are located on two concentric circles with the center of the origin of the coordinate system and radii of 0.2 m and 0.4 m. The spacing between each two adjacent sampling points on a curve is $\lambda_{min}/2$. The measurement is performed over the frequency band 1.2−1.968 GHz. Figure 4.7(c) shows the imaging result. It can be observed that the sphere and also the wall boundaries are clearly

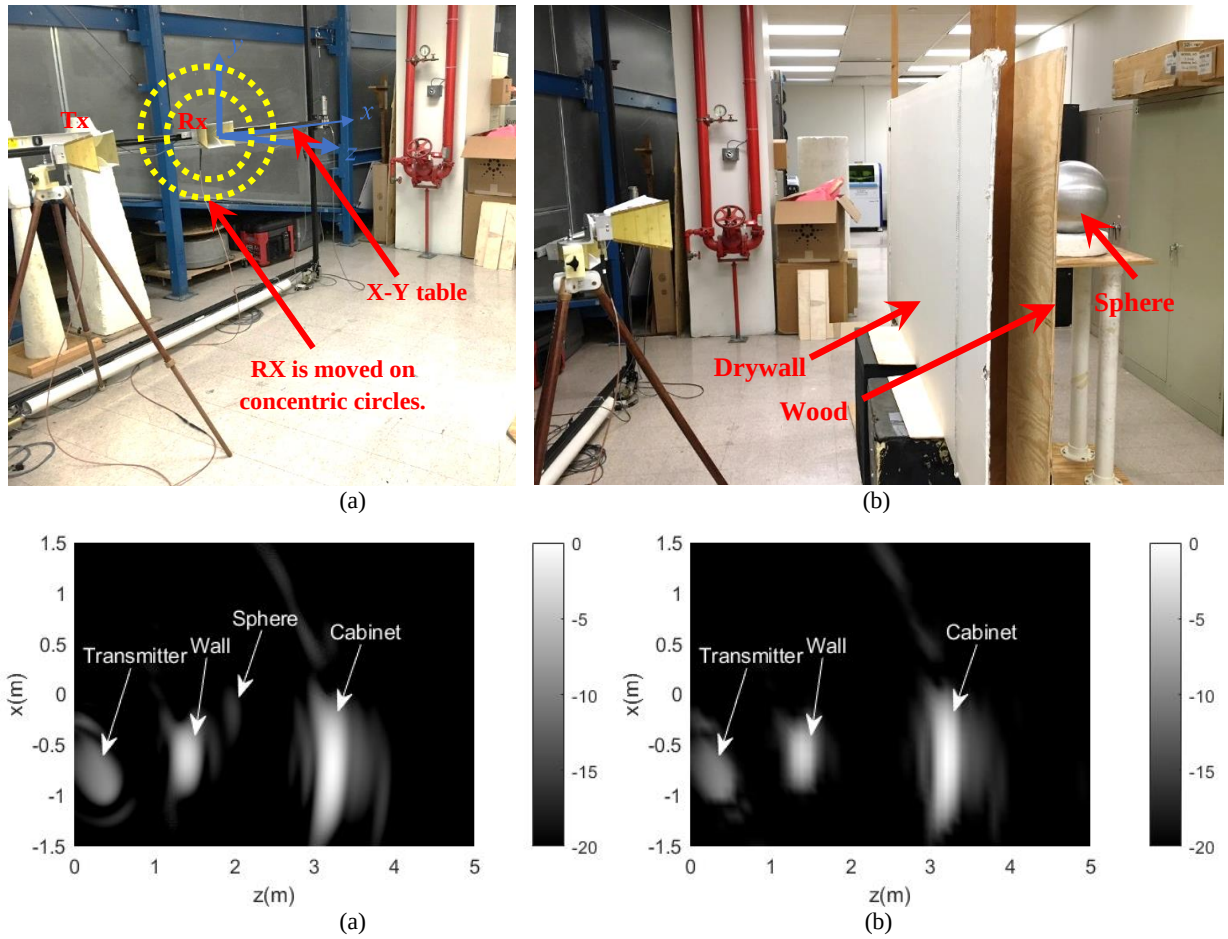

Figure 4.7. Through-the-wall imaging using the fabricated radar and horn antennas. (a) Transmitting and receiving antennas configuration. (b) Wall and objects behind the wall (metallic sphere and cabinet). (c) Imaging result in presence of sphere. (d) Imaging result while the sphere is removed.

imaged. Figure 4.7(d) shows the imaging result while the sphere is removed. Comparing Figure 4.7(c) and Figure 4.7(d) indicates that the image of the sphere is removed in Figure 4.7(d).

4.4. Measurement Results

In this section, first, the range and cross-range resolution performance of the imaging method and the fabricated system are evaluated through simulations and measurements and then, all-directions imaging method is tested in three different scenarios using the fabricated radar system. In all measurements in this section, the transmitter is at the origin of the coordinate system. A computer-controlled turntable is used for moving the receiver on a circular path centered at the

transmitter location. Transmitting and receiving antennas are placed at a height of 92.5 cm measured from the ground to reduce unwanted reflections form the ground.

The transmitter and receiver distance is fixed for all sampling points and is equal to 80 cm for measurements using CP antennas and 121 cm for measurements using LP antennas. Due to the high isolation between the transmitting and receiving CP antennas, the received direct signal is weak in measurements with CP antennas. Since the direct signal is required for error correction, to reliably detect the direct signal from transmitter to receiver, distance between the antennas is reduced in measurements using CP antennas.

In all measurements, the angle between each two adjacent sampling points is 2° resulting in distance of 2.79 cm and 4.22 cm between the sampling points in measurements using CP and LP antennas, respectively. In both cases, the distance between the adjacent sampling points is less than half of the minimum wavelength over the band 1.2–1.968 GHz. For better view of walls and objects, image is not calculated within the distance of 50 cm from the transmitter.

To evaluate the performance of the imaging method and the fabricated radar, the range and cross-range resolution are calculated from measured data obtained using the fabricated radar and metallic pipe (cylinder) and trihedral reflector as targets. The measured results are compared to the simulation results modeling point targets and an ideal bi-static FMCW system with the same frequency sweep parameters as the fabricated system.

Figure 4.8(a) and Figure 4.8(b) show the measurement setup including the fabricated system, CP antennas, and a metallic pipe and a metallic trihedral reflector as the targets. The metallic pipe with the diameter of 7.5 cm and the trihedral reflector with sides of 42.5 cm are located at the distance of 2.1 m and 2.3 m from the transmitter, respectively. Figure 4.8(c) and Figure 4.8(d) show the obtained images for the pipe and the trihedral reflector, respectively, using

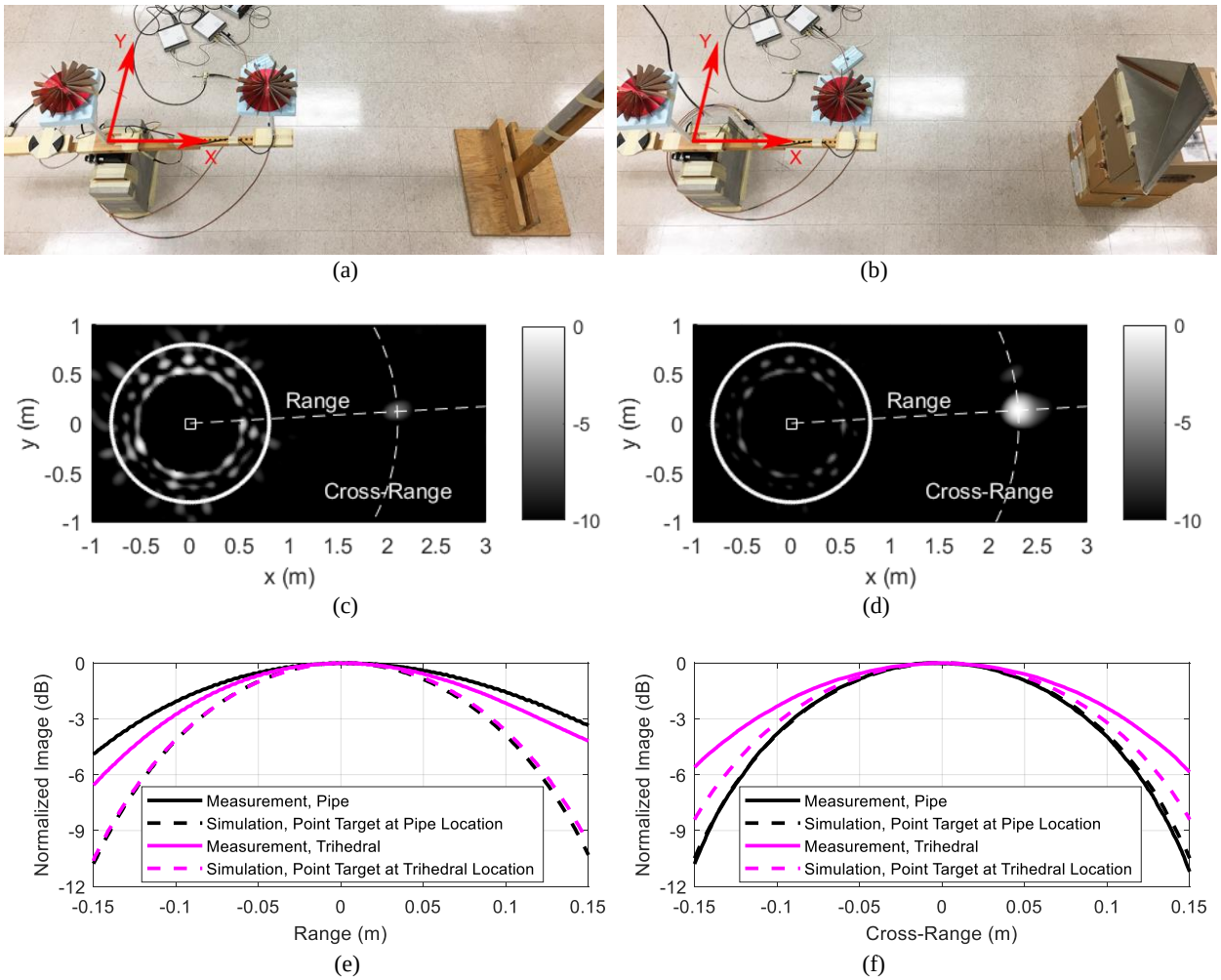

Figure 4.8. Range and cross-range resolution performance evaluation of the fabricated system and imaging method [14]. Transmitter is at $(x, y) = (0, 0)$. 180 sampling points are on the white circles. (a) Measurement setup and a metallic pipe as the target. (b) Measurement setup and a trihedral reflector as the target. (c) Image formed for (a). (d) Image formed for (b). Dashed lines show the range and cross-range directions. Measured image for the pipe and trihedral reflector and simulated image (considering ideal system and point targets at the location of the pipe and trihedral reflector) along the range direction (e) and along the cross-range direction (f) (images are centered at the targets' locations).

180 equally spaced sampling points on a circle with the radius of 0.8 m. It can be observed that both objects are clearly imaged. To evaluate the range and cross-range resolution of the fabricated system and imaging method, the image is calculated along the range and cross-range directions shown in Figure 4.8(c) and Figure 4.8(d) using measured data and compared to the simulation results (modeling point targets located at the same position as the targets in the measurements). The results for range and cross-range resolution are plotted in Figure 4.8(e) and Figure 4.8(f), respectively.

For a pair of transmitter and receiver in a bi-static imaging system, the range resolution is a function of directions to the transmitter and receiver [66]. However, considering all the receivers located on a circle with the center at the transmitter location, the range resolution is uniform in all directions. According to Figure 4.8(e), the range resolution for point targets is 0.18 m and is independent of the distance from the transmitter. Considering the -3-dB points, the obtained range resolution for pipe and trihedral reflector is 0.26 m and 0.22 m, respectively. The increase in the value of the range resolution is due to the fact that the bi-static RCS of the pipe and trihedral reflector varies over the frequency.

According to the results for point target in Figure 4.8(f), the cross-range resolution depends on the range and is equal to 0.178 m and 0.194 m at the distance of 2.1 m and 2.3 m from the transmitter, respectively. It can be observed in Figure 4.8(f) that the image of pipe has the same cross-range resolution as the point target. This is due to the fact that at a given frequency within the operation band, the pipe exhibits approximately the same bi-static RCS for different sampling points. For the trihedral reflector, the bi-static RCS is reduced significantly at the sampling points located at the top and bottom of Figure 4.8(d). This results in a reduced synthetic aperture size and cross-range resolution (0.22 m).

Figure 4.9 shows the simulated range and cross-range resolution for a point target at different distances from the transmitter and for different operation bandwidths. The transmitter and sampling points configuration is the same as Figure 4.8. In Figure 4.9, the -3-dB points are considered for the calculation of the range and cross-range resolution. According to Figure 4.9(a), the range resolution is independent of the distance from the transmitter while the cross-range resolution is proportional to the distance from the transmitter.

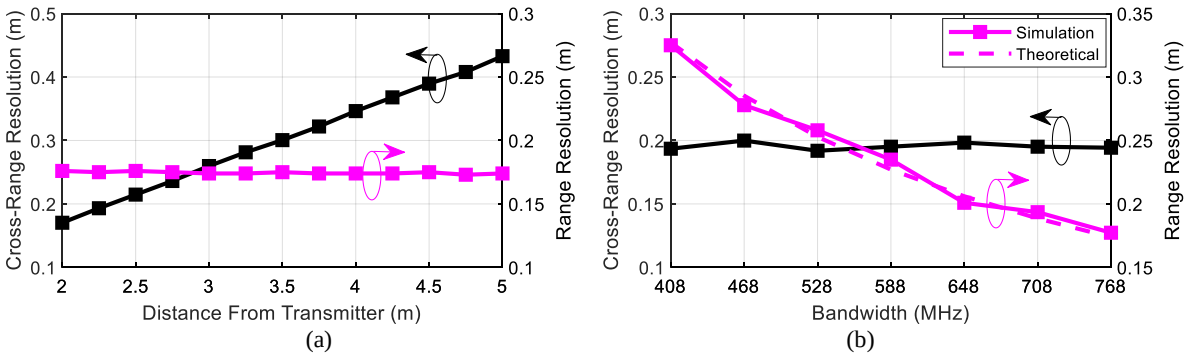

Figure 4.9. Range and cross-range resolution simulation results considering ideal imaging system and point targets and utilizing 180 sampling points distributed uniformly on a circle with radius of 0.8 m centered at the transmitter location [14]. (a) Range and cross-range resolution versus distance of the point target from the transmitter. The operation bandwidth is 768 MHz. (b) Range and cross-range resolution with respect to the operation bandwidth for a point target at the distance of 2.3 m from the transmitter. The center frequency is at 1.584 GHz.

In Figure 4.9(b), the bandwidth of the system is varied while the center frequency is kept constant. With a fixed center frequency, the cross-range resolution is approximately independent of the bandwidth while the range resolution improves as the system bandwidth increases. According to the results, the range resolution follows its theoretical formula.

To test the performance of the all-directions through-the-wall imaging method, three different scenarios are considered.

For the first measurement, a simple 3.6 m × 3.6 m × 1.2 m room was fabricated using two layers of drywalls and wooden posts. Thickness of each drywall is 1 cm and the walls are separated by 9 cm. Figure 4.10(a) shows the configuration and dimensions of the walls and the objects placed behind the walls. The objects are one trihedral reflector (with sides of 42.5 cm), two vertical metallic pipes (with diameters of 5 and 7.5 cm) connected from the sides, and one metallic cylindrical object placed horizontally. Figure 4.10(b) shows the photograph of the imaging area. Transmitter is placed at the center of the room.

Figure 4.10(c) shows the imaging result using LP antennas. According to Figure 4.10(c), parts of the walls with specular reflections, trihedral reflector, and pipes are imaged while the

horizontally oriented object is not clearly imaged due to its low RCS for vertically polarized waves. The peaks close to sampling points are due to the direct signal from the transmitter to receiver.

CP antennas transmit and receive both vertically and horizontally polarized waves and as a result, they can be employed for imaging of the objects with large aspect ratio independent of their orientation. Figure 4.10(d) shows the imaging result while a left-handed CP (LHCP) antenna is used for the transmitter and a right-handed CP antenna (RHCP) is used for the receiver. It can be observed that walls and all objects including the launcher are clearly imaged and there is no peak close to the sampling points. The latter indicates that the direct signal from the transmitter to the receiver is reduced using orthogonal CP antennas.

In Figure 4.10(c) and Figure 4.10(d), the walls are imaged as discrete points instead of solid lines. This is due to the fact that the points on the walls' surface provide specular reflections for only a limited number of sampling points in contrast to the objects with limited size (e.g. pipe) which provide specular reflections for majority of the sampling points. In this case, image formation using the sampling points that do not receive specular reflections from a specific point on the wall, may have destructive impact on the final image at that point. This generates nulls in the image of walls. In the next chapter, a method is presented to discriminate walls and large flat surfaces from limited size objects.

For the imaging system, the required time for performing 180 measurements is about 9.22 ms (= 180 × 51.2 μs). However, in measurements, collecting 180 samples at different positions takes about 15 minutes, which is due to the low rotation speed of the turntable.

In Figure 4.10(d), the range and cross-range resolution for trihedral reflector is 0.2 m and 0.25 m, respectively.

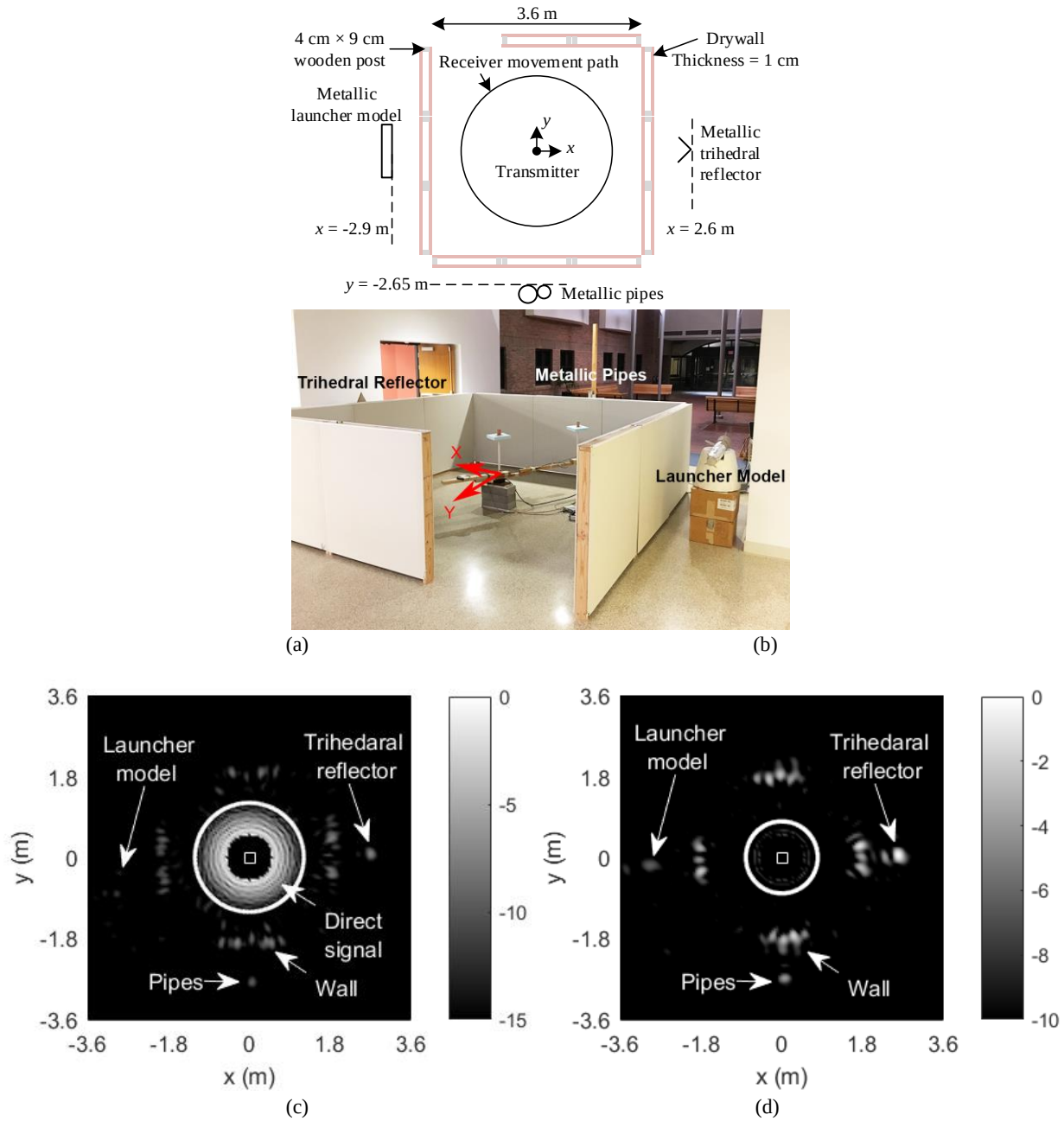

Figure 4.10. (a) Geometry of the fabricated room and objects. (b) Photo of the room and objects. Normalized image (in dB) using LP antennas (c) and CP antennas (d). Transmitter is at $(x, y) = (0, 0)$. Sampling points are on the white circle [14].

It should be noted that the small shift in the position of the objects' images is due to the effects of walls that are not compensated here.

Using a MATLAB code running on a Core i5 CPU, the computation time for the image in Fig. 9(d) is about one minute.

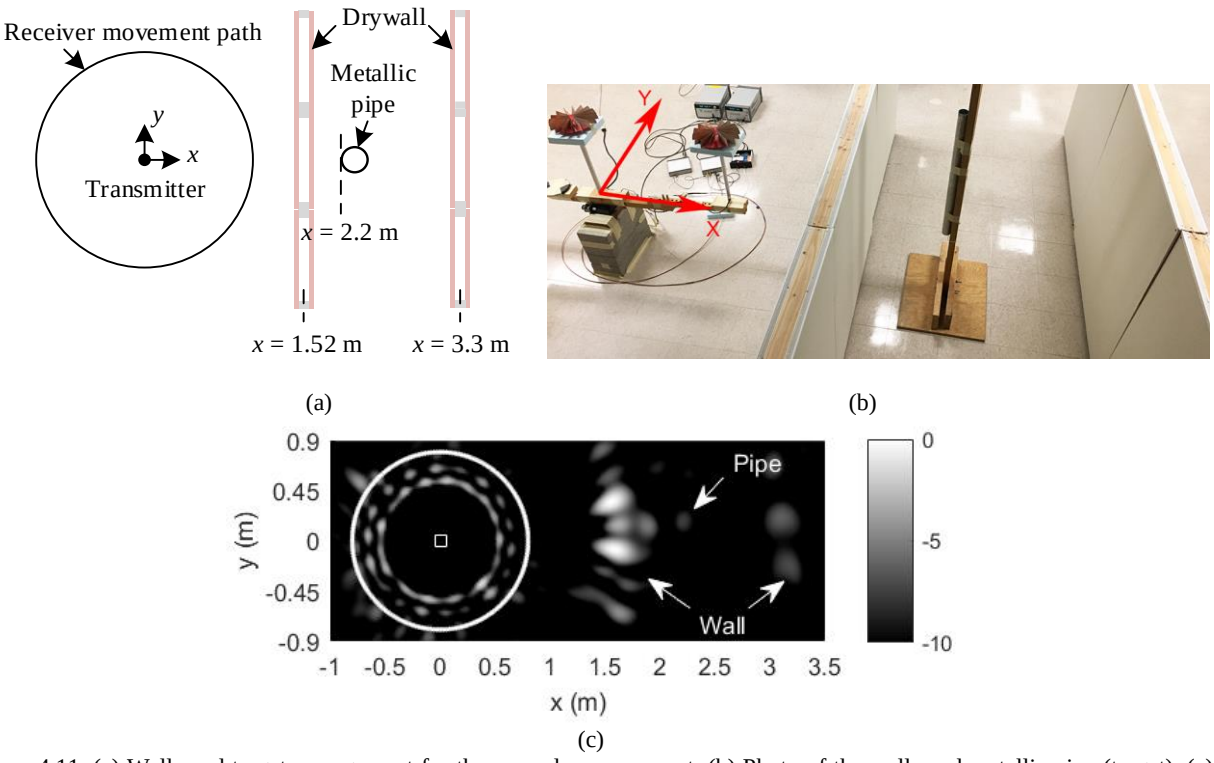

Figure 4.11. (a) Walls and target arrangement for the second measurement. (b) Photo of the walls and metallic pipe (target). (c) Normalized image (in dB) using CP antennas. Transmitter is at $(x, y) = (0, 0)$. Sampling points are on the white circle [14].

Figure 4.11(a) and Figure 4.11(b) show the measurement setup for the second scenario. In this measurement, a metallic pipe with the diameter of 7.5 cm is placed in between two parallel walls. The structure of the walls and arrangement of the transmitter and sampling points are the same as the previous measurement. Figure 4.11(c) shows the image formed using CP antennas. It can be observed that both walls and the pipe are clearly imaged. In Figure 4.11(c), the range and cross-range resolution for the pipe is 0.19 m and 0.23 m, respectively.

Figure 4.12(a) shows the measurement setup in a real room. For this measurement, an LHCP antenna is used for the transmitter and an RHCP antenna is used for the receiver. Because of the limitation in space, instead of a full circle, the receiver is moved in the range ϕ = -30°–210° (ϕ is an angle defined by a line passing through the transmitter and receiver location and x-axis). Figure 4.12(b) shows the image formed by 121 sampling points. It can be observed that, parts of

(a)

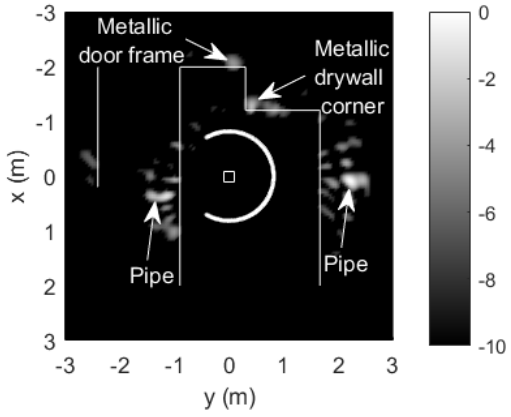

(b)

Figure 4.12. (a) Measurement setup in a real room. (b) Normalized image (in dB) using CP antennas. Solid lines show the position of sides of walls which are closer to the transmitter. Transmitter is at $(x, y) = (0, 0)$. Sampling points are on the white curve around the transmitter [14].

the walls with specular reflections and the objects behind the walls (two metallic pipes) are imaged. In addition, a wall behind the door on the left (Figure 4.12(a)) is also imaged. The wooden doors are not imaged because of their low reflection coefficient.

The measurement results in this section show that all-directions through-the-wall imaging provides high resolution 360° images using only sampling points on a circle. In all images, parts of the surrounding walls and hidden objects that provide specular reflections are imaged.

4.5. Conclusion

An imaging system realizing the concept of all-directions through-the-wall imaging and an image formation technique compatible with the proposed system have been introduced. The imaging system is a bi-static FMCW radar utilizing wideband omnidirectional CP antennas. Image

formation technique corrects for deterministic and random delays in the system and synchronization errors. The performance of the system and imaging method have been tested through laboratory and field measurements. Imaging results show that all-directions through-the-wall imaging can provide high resolution 360° images of the walls, objects, and hidden features of the imaging area with specular reflections using only one transmitter and one moving receiver with high mobility.

Chapter 5 Methods for Imaging Enhancement in Through-the-Wall SAR Imaging

5.1. Introduction

In this chapter, two methods are introduced for enhancing the imaging in through-the-wall SAR imaging.

The first method is an imaging algorithm employing Generalized Pencil of Function (GPOF) to reduce the background noise resulted from unresolved multi-path and unsuppressed sidelobes of point spread function of the imaging algorithm. The method also improves the range resolution by accurately detecting the location of reflections in the imaging area and forming the image at the detected point. The method detects the delays between the transmitter to scattering points and from there to the receiver and utilizes multi-static back-projection focusing to create high fidelity and high resolution radar images. The method introduced in this chapter in applicable to the stepped frequency radar data. However, its applicability can be extended to FMCW radar data. Performance of the new imaging enhancement method is evaluated by applying it to the simulation data presented in Chapter 2.

As shown in Chapter 4, in the standard high resolution SAR processing, walls and objects with large surface are imaged as discrete points instead of solid lines and as a result, without prior knowledge about the imaging area, walls may be interpreted as few discrete closely spaced targets. In this chapter, a method is presented to discriminate walls and objects with large flat surfaces from other objects. Considering specular reflections from a wall surface, it is shown that the

transmitter in conjunction with a wall surface acts as an object with limited size whose location is approximately equivalent to the location of the transmitter mirrored with respect to the wall surface. In the wall detection approach, instead of focusing the synthetic radar beam on a point on the wall surface, the beam is focused at the location of the image of transmitter with respect to the wall surface considering only specular reflections. This is done by assuming there exists a wall at a distance from the transmitter with a known orientation. Output of the method is an image in polar format in which locations of peaks determine the distance and orientation of the actual wall surfaces inside the imaging area. The method is applied to the measured bi-static and monostatic SAR data and the results exhibit the capability of the method in detection of walls in real scenarios even in presence of strong scatterers and large coupling between transmitter and receiver.

5.2. Background Noise Reduction and Range Resolution Enhancement in Through-the-Wall SAR Imaging

In through-the-wall imaging scenario shown in Figure 2.2, assuming that the transmitter sends a narrow pulse in time domain, the transmitted pulse is then reflected from different boundaries and thus the received signal is a sum of the shifted copies of the transmitted pulse with different amplitudes and delays. Therefore, the signal received at nth sampling point (s_n^r) can be represented as

$$s_n^r(t) = \sum_{k=1}^{K} a_k p(t - t_k) \tag{5.1}$$

where, $p(t)$ is the transmitted pulse and a_k and t_k (real numbers) are the amplitude and delay of the kth copy of the transmitted pulse. The Fourier transform of the received signal is

$$S_n^r(f) = \left(\sum_{k=1}^{K} a_k e^{-j2\pi f t_k}\right) P(f) = H(f)P(f), \tag{5.2}$$

where $P(f)$ is the Fourier transform of the transmitted pulse and $H(f)$ is the frequency response of the imaging area. Using a stepped frequency radar system, $H(f)$ can be directly measured at discrete frequency samples. According to (5.2), $H(f)$ is the sum of exponential terms. In general, the received copies of the transmitted pulse may be distorted in time due to dispersion and thus $H(f)$ is approximately equal to sum of exponentials

$$H(f) \cong \sum_{k=1}^{K} a_k e^{-j2\pi f t_k}. \tag{5.3}$$

Equation (5.3) suggests that by representing $H(f)$ by a finite number of exponentials, t_n's can be determined. Multiplying t_n by free space velocity of EM waves, the total travel distance is determined. Knowing the positions of the transmitter and receiving points, the location of the reflecting points which are the wall boundaries and objects can be determined. By calculating the image only around these points, the side lobes in the range direction (due to the limited bandwidth) are eliminated and thus the range resolution in the final image is improved.

To apply the mentioned method for improving the range resolution, first, $H(f)$ should be approximated by the sum of exponential terms. There are different methods for representing signals by sum of exponentials such as Prony method [67], Generalized Pencil of Function (GPOF) [68], and matrix pencil method (MPM) [69]. In the proposed method, GPOF is selected to represent $H(f)$ by sum of exponentials due to its good performance in the presence of noise. By applying GPOF to the samples of $H(f)$, $H(f)$ is presented as

$$H(f) = \sum_{m=1}^{M} A_m e^{B_m f} \tag{5.4}$$

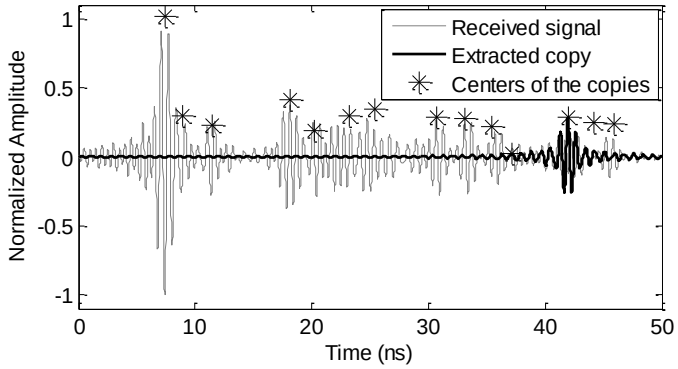

Figure 5.1. Received time domain signal at the sampling point (r, ϕ) = (2.25 m, 90°) in Figure 2.7(c) and detected centers and amplitudes of the copies of the transmitted signal by GPOF [13].

where, A_m and B_m are generally complex numbers and M is the number of exponential terms that should be set in GPOF. Each exponential term represents a copy of the transmitted signal received at the sampling point. In order to accurately represent $H(f)$ by sum of exponential, M in (5.4) must be equal to K in (5.3) which is unknown for a received signal. Increasing M beyond K produces the terms with A_m's close to zero or invalid terms with negative delays. By equating the mth terms in (5.4) and (5.3), t_m is obtained by

$$t_m = Re(B_m/(-j2\pi)\,). \tag{5.5}$$

To show the performance of the proposed method, GPOF is applied to the signal received at the sampling point located at (r, ϕ) = (2.25 m, 90°) in Figure 2.7(c). Figure 5.1 shows the inverse Fourier transform of the received signal. Transmitted signal has uniform magnitude over the frequency range 1.2−2 GHz and thus the time domain transmitted signal is a modulated sinc function. Received signal is sum of shifted copies of the transmitted signal with different amplitudes. The center of each copy in time shows the delay of that copy. The delays detected by applying GPOF to the received signal are indicated by asterisks in Figure 5.1 where M = 16 is used. The vertical positions of the asterisks is equal to the detected amplitude for the copies ($|A_m|$). It is shown that the detected delays are in accordance with the center of the copies. The inverse

Fourier transform of the ninth exponential term is also plotted in Figure 5.1. The number of the copies that have significant amplitudes are 13 according to Figure 5.1. The extra three terms have the amplitudes close to zero (one is shown in Figure 5.1 and the remaining two terms with small amplitudes were discarded since they predicted negative delays).

In the proposed imaging method, the detected delays for the copies at all sampling points can be used for removing the sidelobes around the imaged objects to improve the range resolution and also reduce the background noise. To achieve this, first, the location of the reflecting points is determined using the extracted delays and then the imaging is performed only at the determined reflecting points instead of the entire imaging area. The imaging procedure is as follows

1. The imaging area is discretized with a very fine mesh and value of one is assigned to all pixels in the imaging area as shown in Figure 5.2(a).
2. For each sampling point, the delays (t_ms) are calculated and the valid values (positive delays) are saved. Each saved delay corresponds to a reflecting point.
3. For each sampling point and for each extracted delay value, the delay is multiplied by the speed of EM waves in free space (c_0) to calculate the total distance from transmitter to the reflecting point and from the reflecting point to the sampling point (d_m). The calculated distance is used to determine the locus of the reflecting point which is an ellipse with the focal points located at the transmitter and the sampling point positions. This is illustrated in Figure 5.2(b).
4. For each pixel in the imaging area, the total distance from the transmitter to the center of the pixel and from the center of the pixel to the sampling point is calculated (d_p). If $\left|d_m - d_p\right| < \delta$ (for some small quantity δ), then the pixel is considered as a reflecting

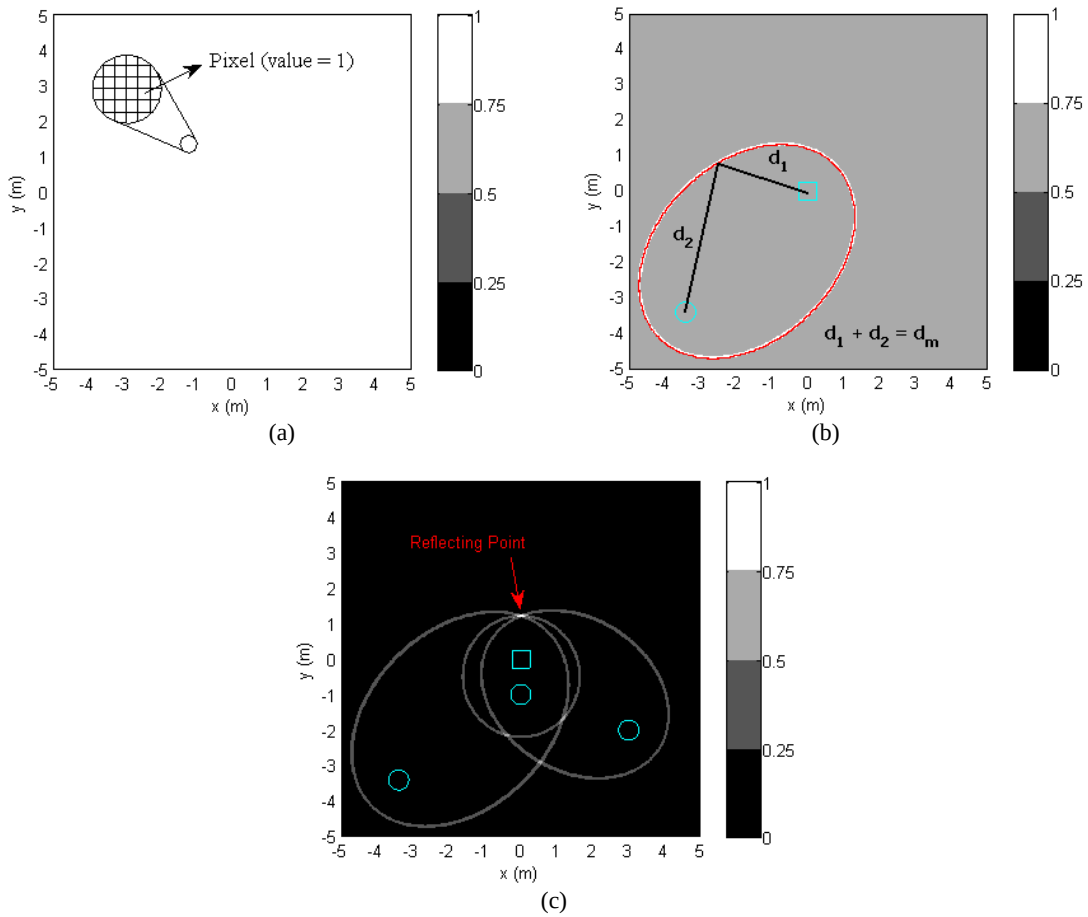

Figure 5.2. Detection of reflecting points (square represents the transmitter, circles indicate sampling point) [13]. (a) Meshing and initialization of pixels in the imaging area. (b) Possible loci of a reflecting point obtained by a detected delay from a sampling point (solid line is the actual possible loci of the reflecting point and the nearby pixels satisfy the criteria $|d_m - d_p| < \delta$). (c) The reflecting point detected by three sampling points.

point and its current value is multiplied by one. If a pixel is not a reflecting point, its current value is multiplied by a factor $\alpha < 1$. This is shown in Figure 5.2(b).

5. Following the same procedure for all sampling points, all extracted delays, and all pixels, the pixels that have the value close to one are locations of the reflecting points that are detected at most of the sampling points. This is illustrated in Figure 5.2(c) for three sampling points and one delay for each sampling point.
6. Back-projection imaging is performed only at the pixels with values greater than P (P is a positive number less than one that is set by the user).

Figure 5.3(a) shows the final value of pixels obtained by applying the above procedure with $\delta = 0.5\lambda_{min}$ and $\alpha = 0.99$ to the same configuration as Figure 2.7(c). It can be observed that the pixels at the target position and wall boundaries have values close to 0 dB since they are detected as reflecting points by most of the receivers at different points. Figure 5.3(b) shows the same image as Figure 2.7(c) except that it is calculated only at the pixels obtained in Figure 5.3(a) with the values greater than -8 dB ($P = 0.4$). It can be observed that the background noise is significantly reduced. Figure 5.3(c) and Figure 5.3(d) show the imaging result when applying the above procedure with $\delta = 0.5\lambda_{min}$, $\alpha = 0.99$, and $P = 0.4$ to the same configuration as Figure 2.8(b) and Figure 2.10(c) respectively. In both figures, it can be observed that the background noise and effect of multiple reflections are significantly reduced.

In addition to reducing the background noise, the proposed method can also improve the range resolution even in presence of noise. Considering the same configuration for the transmitter and sampling points as Figure 2.3(b), for two point targets located at (r, ϕ) = (5 m, 90°) and (5 m + $0.6\Delta R$, 90°) (ΔR is the theoretical range resolution which is equal to 0.1875 m considering 800 MHz bandwidth used in all simulations), the PSF is calculated by (2.1) with uniform array coefficients and shown in Figure 5.4(a). In this figure, SNR is 15 dB (in all simulations, the noise model is white Gaussian noise). It can be observed that images of two objects cannot be resolved. Figure 5.4(b) shows the image after applying the proposed method (the values for different parameters of the method is the same as the values used to obtain Figure 5.3). The result shows that the images of two objects are completely resolved and thus the range resolution of the image with SNR of 15 dB is improved from the theoretical value of ΔR to $0.6\Delta R$. Different runs of the same simulation (with SNR = 15 dB) provides the same result for the range resolution. Simulation results show that with SNR of less than 15 dB, the method is not able to achieve the range

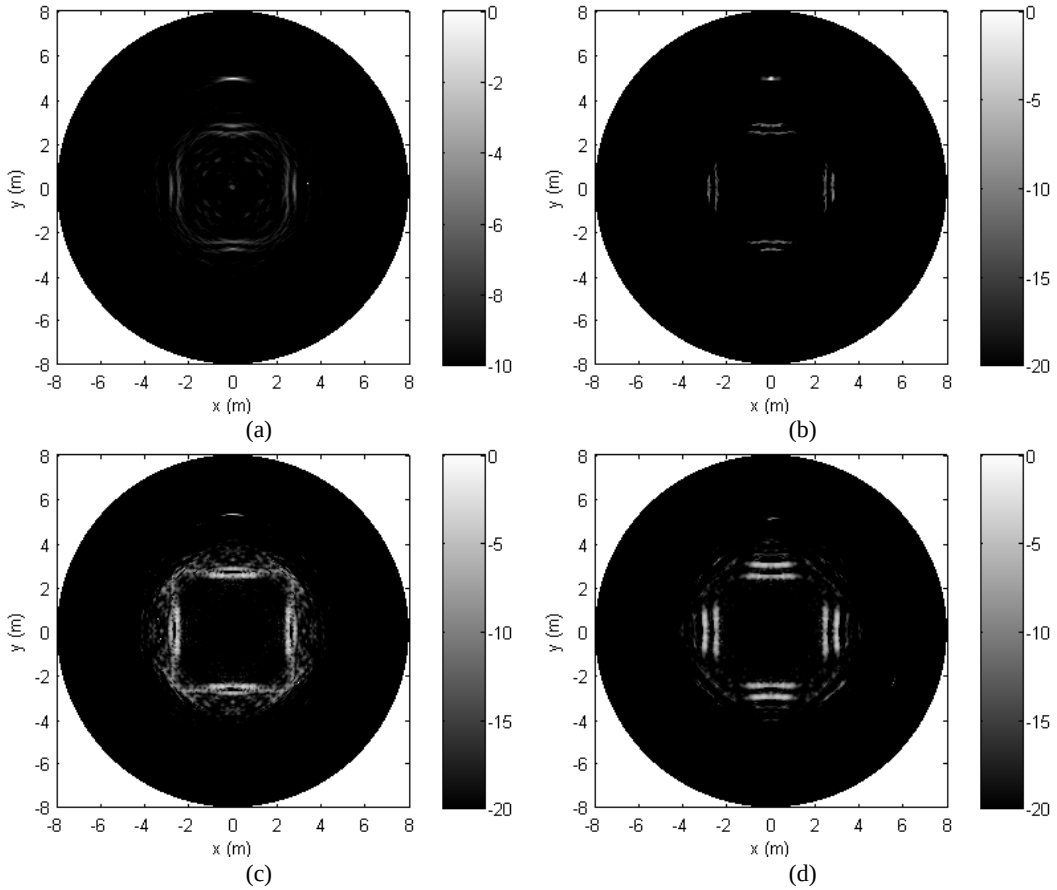

Figure 5.3. (a) The value of pixels (in dB) after applying the imaging method based on GPOF to the same configuration as Figure 2.7(c). (b) The same image as Figure 2.7(c) except that it is calculated only at the pixels in (a) with the values greater than -8 dB. (c) The image after applying the imaging method based on GPOF to the same configuration as Figure 2.8(b). (d) The image after applying the imaging method based on GPOF to the same configuration as Figure 2.10(c) [13].

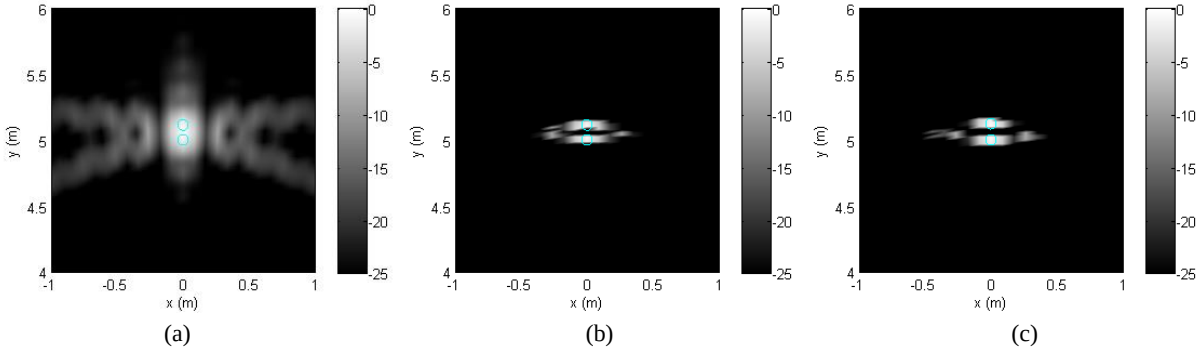

Figure 5.4. PSF calculated by uniform array coefficients for the same configuration for transmitter and sampling points as Figure 2.3(b), circles indicate the location of point targets. (a) Imaging results for two point targets located at (r, ϕ) = (5 m, 90°) and ((5 m + 0.6ΔR), 90°), SNR = 15 dB. (b) Applying the imaging method based on GPOF for improving the range resolution to the image in (a), SNR = 15 dB. (c) Applying the method for improving the range resolution to the image of two point targets located at (r, ϕ) = (5 m, 90°) and ((5 m + 0.65ΔR), 90°), SNR = 10 dB [13].

resolution of 0.6ΔR. Figure 5.4(c) shows the imaging result with SNR of 10 dB for the same configuration as Figure 5.4(a) except that the distance between two points objects is increased to

$0.65\Delta R$. It can be observed that the images of two objects are completely resolved and therefore the range resolution of the image is $0.65\Delta R$ considering SNR = 10 dB.

5.3. A Method for Detection of Flat Walls in Through-the-Wall SAR Imaging

For many applications such as mapping building interiors for security and rescue missions using robotic platforms, identification of walls, corridors, and hidden pathways are also of great interest. In monostatic SAR, if the linear path of the synthetic aperture is not parallel to the wall, the receiver may not receive reflected signals from the wall and hence the wall may not be imaged. On the other hand, all-directions through-the-wall imaging using a bi-static SAR system employing omnidirectional antennas (introduced in Chapter 2) is capable of receiving reflected signals from walls without the need for the transceiver movement path to be parallel to the walls.

Unlike point targets, walls that are extended along a plane do not present single phase center, hence SAR techniques such as back-projection cannot easily identify walls from point targets.

In high resolution SAR, at least a pair of a transmitter and a receiver measure the scattered fields at different locations (sampling points) within the synthetic aperture. Point targets or targets with limited surface size exhibit significant scattering in different directions that include the receiver aperture. On the other hand, each point on a flat wall and objects with large flat surfaces exhibits reflections at certain directions (specular reflections) which depending on the relative position of the transmitter and receiver and the surface orientation may or may not fall within the synthetic aperture. In this case, forming the image using the entire aperture including the sampling points that do not receive reflection from a point on the wall surface, may have a destructive effect on the image of that point. Measurement and simulation results show that in SAR systems with

high cross-range resolution where a large aperture is entirely used for image formation, walls are imaged as few discrete points instead of a solid line. It can be seen in the imaging results presented in Figure 4.10. As a result, without prior knowledge about the imaged area the walls may be interpreted as discrete closely separated objects.

Methods for detection of building features including walls and corners have been developed. These methods are generally based on smashed filter processing [70] or use of over-complete dictionary [71], [72] and require training data or prior knowledge about the phase and amplitude response of the buildings' features. In this section, a simple and fast method is presented to discriminate walls and objects with large flat surfaces from point targets and detect the position and orientation of walls surfaces in multi-static SAR through-the-wall imaging. The method can be used in monostatic SAR imaging if specular reflections from the wall surface are within the aperture. The method is applicable even in presence of strong scatterers and large coupling between transmitter and receiver. In contrast to conventional methods for detection of walls and building features, the presented method does not require training data or knowledge about the phase and amplitude response of the walls. However, its application is limited to detection of walls surfaces.

5.3.1. Image of Walls in Through-the-Wall SAR Imaging

Figure 5.5(a) shows the image of pipe and the wall that is close to the pipe in the measurement setup shown in Figure 4.10(a) formed by 90 samples located at $x>0$ half space and Figure 5.5(b) shows the image formed by 90 samples located at $x<0$. It can be observed that the object behind the wall with limited surface area (pipe) is imaged at the same location in both figures. This is due to the fact that the object with limited surface size exhibits significant scattering

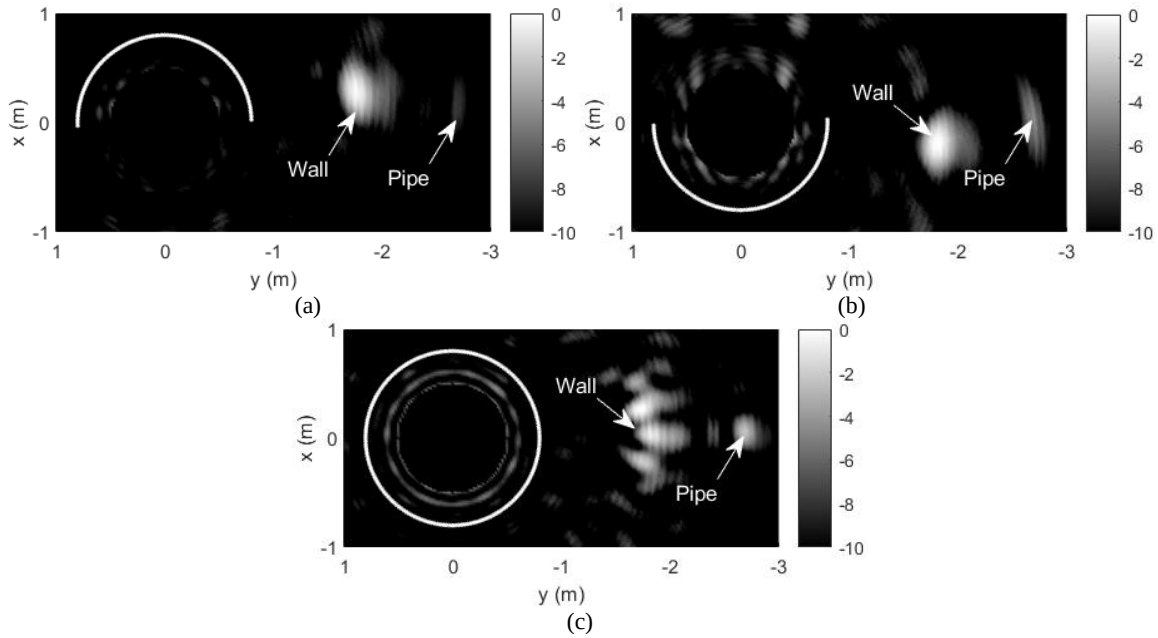

Figure 5.5. (a) Image (in dB) calculated using the sampling points located at x>0 in the measurement setup shown in Figure 4.10(a) using CP antennas. (b) Image calculated using the sampling points located at x<0. (c) Image formed using all the sampling points. Sampling points are indicated by white dots [17].

in different directions including the entire formed aperture as illustrated in Figure 5.6. In contrast, each point on the wall surface exhibits specular reflection at a certain direction depending on the location of the transmitter as shown in Figure 5.6. As a result, only part of the wall surface that exhibits specular reflections within the aperture is imaged instead of the entire wall surface as shown in Figure 5.5(a) and Figure 5.5(b). In this case, trying to form the image of the entire wall using all sampling points including the sampling points that do not receive scattering from a specific point on the wall surface, may have destructive effect on the image of that point. This is shown in Figure 5.5(c), where the image is formed using all the sampling points. In this figure, the wall is imaged as few discrete points instead of a solid line, indicating the destructive effect of imaging using the entire aperture (in this case part of the wall located at x<0 (x>0) does not provide specular reflections for sampling points located at x>0 (x<0)). It can be observed in Figure 5.5(c) that the metallic object behind the wall is imaged without any distortion, since the scattered signals from the object is received at majority of sampling points.

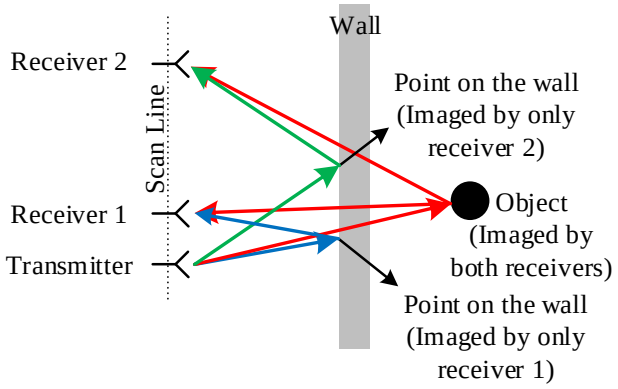

Figure 5.6. Reflection and scattering from a wall surface and a small size object [17].

In monostatic SAR imaging, at a given location for the transceiver, only a part wall in front of the transceiver provides a specular reflection. In this case, similar to bi-static case, forming the image of wall using all the sampling points including the sampling points that do not receive scattering from a specific point on the wall surface, may produce nulls in the image of that point. This could be observed in the monostatic SAR imaging results presented in Figure 7(c) of [73], and measurement results in Figure 11(a) of [74].

5.3.2. Method for Detection of Walls and Large Flat Surfaces

In through-the-wall imaging, signals received from a flat wall surface experienced specular reflection. Figure 5.7 illustrates the rays experienced specular reflection from a wall surface in both bi-static and monostatic SAR imaging scenarios. According to Figure 5.7, the reflected rays from a wall surface are equivalent to the rays that emanated from a fictitious object located behind the wall. Neglecting the additional delay that signals experience in propagation inside the wall, location of these fictitious objects is the same as the location of the transmitter mirrored with respect to the wall surface. For a specific wall surface, this location may be either fixed (Figure 5.7(a)) or variable (Figure 5.7(b)). This suggests that if a wall surface is assumed to be present in

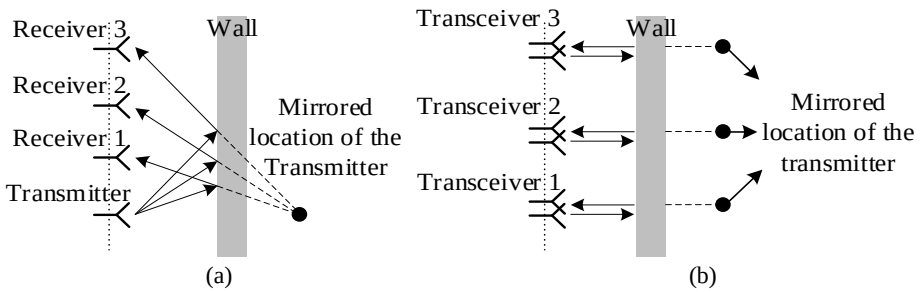

Figure 5.7. Specular reflections from a flat wall surface in (a) bi-static SAR and (b) monostatic SAR [17].

the imaging area and for all pairs of transmitter and sampling point, the image is calculated at the location of the transmitter mirrored with respect to the assumed wall surface, the image will have high intensity if the assumed wall surface is real. This technique can be used to detect walls and large flat surfaces in the imaging area.

Knowing the locations of the transmitter and sampling points and locations and orientations of walls surfaces, the signal path for specular reflections can be simply determined. However, in reality, the location and orientation of walls surfaces are unknown and must be determined.

To determine the location and orientation of walls surfaces in the imaging area, a wall surface with the length of infinity is considered at the distance of R from the origin as shown in Figure 5.8. The orientation of the wall is defined by the angle between the line perpendicular to the wall surface and x-axis which is denoted by θ in Figure 5.8. Assuming that the aperture is formed by N pairs of the transmitter and sampling point, the steps for detection of a wall surface are as follows

1. choose a value for R and θ such that all transmitter and sampling point pairs are located in one side of the wall (otherwise R and θ do not define a real wall);
2. define a unit vector normal to the wall surface pointing to side of the wall where all pairs of transmitter and sampling points are located. This vector is denoted by $\hat{n}$ in Figure 5.8 and is equal to $-\cos(\theta)\,\hat{x} - \sin(\theta)\,\hat{y}$;

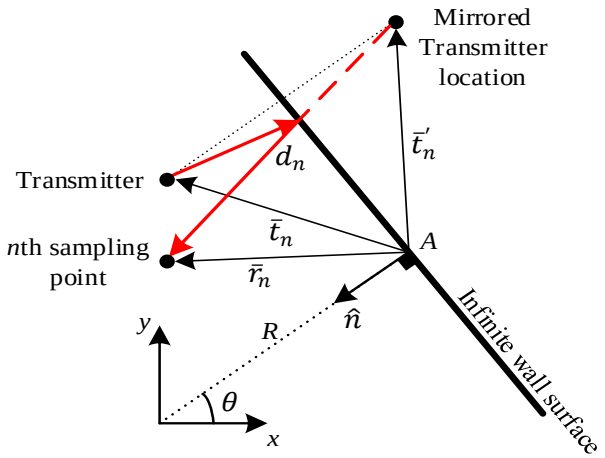

Figure 5.8. Defining a wall surface and mirroring transmitter with respect to the wall surface for wall detection using specular reflections and back-projection [17].

3. define the point A where the wall and the line perpendicular to the wall and passing through the origin intersect (Figure 5.8). A is at $(x, y) = (R\cos(\theta), R\sin(\theta))$;
4. for nth pair of transmitter and sampling point, define the vectors $\bar{t}_n$ and $\bar{r}_n$ that define locations of the transmitter and sampling point, respectively, with respect to the point A a shown in Figure 5.8;
5. using the vectors $\hat{n}$ and $\bar{t}_n$, mirror the location of the transmitter with respect to the wall. The vector $\bar{t}'_n$, defining the location of the mirrored transmitter, is obtained by $\bar{t}'_n = \bar{t}_n - 2(\hat{n} \cdot \bar{t}_n)\hat{n}$;
6. free space path length from the mirrored transmitter location to nth sampling point location, d_n, for a ray experiencing specular reflection from the wall is calculated by $d_n = |\bar{t}'_n - \bar{r}_n|$;
7. considering a stepped frequency continuous wave radar with M frequency steps, the image at location of the transmitter mirrored with respect to the assumed wall is calculated for each pair of transmitter and sampling point using back-projection and

then the resulting images are coherently added and assigned to the selected R and θ as follows

$$I(R,\theta) = \sum_{n=1}^{N} \sum_{m=1}^{M} S_{mn} e^{jk_m d_n} \tag{5.6}$$

where S_{mn} is the frequency response at mth frequency step and for nth pair of transmitter and sampling point. $I(R,\theta)$ will have large intensity if R and θ define a real wall surface. It is noted that in this step, images that are calculated for different pairs of transmitter and sampling points are always added together constructively, although they are calculated at different locations for the transmitter mirrored with respect to the wall (e.g. in monostatic SAR as illustrated in Figure 5.7(b));

8. repeat steps 4)−7) for all N pairs of transmitter and sampling point;
9. repeat steps 2)−8) for all valid pairs of R and θ within field of view of the synthetic aperture.

After calculation of $I(R,\theta)$ for all possible values of R and θ, plotting $I(R, \theta)$ in a polar format results in an image in which the location of peaks determine points A (the distance from the origin and orientation) for the walls and large flat surfaces that exist in the imaging area and provide specular reflections within a large area in the synthetic aperture.

A MATLAB code for detection of walls and large flat surfaces in through-the-wall imaging using bi-static FMCW transceivers is provided in Appendix B.

To evaluate performance of the method in detection of walls, the method is applied to a 2D (no variation along *z*) simulated bi-static through-the-wall imaging data. Figure 5.9(a) shows the geometry of the imaged area which is a room with four walls. The walls thickness and permittivity are 20 cm and 4, respectively. The wall located at the top is a cinder block wall. Transmitter is an

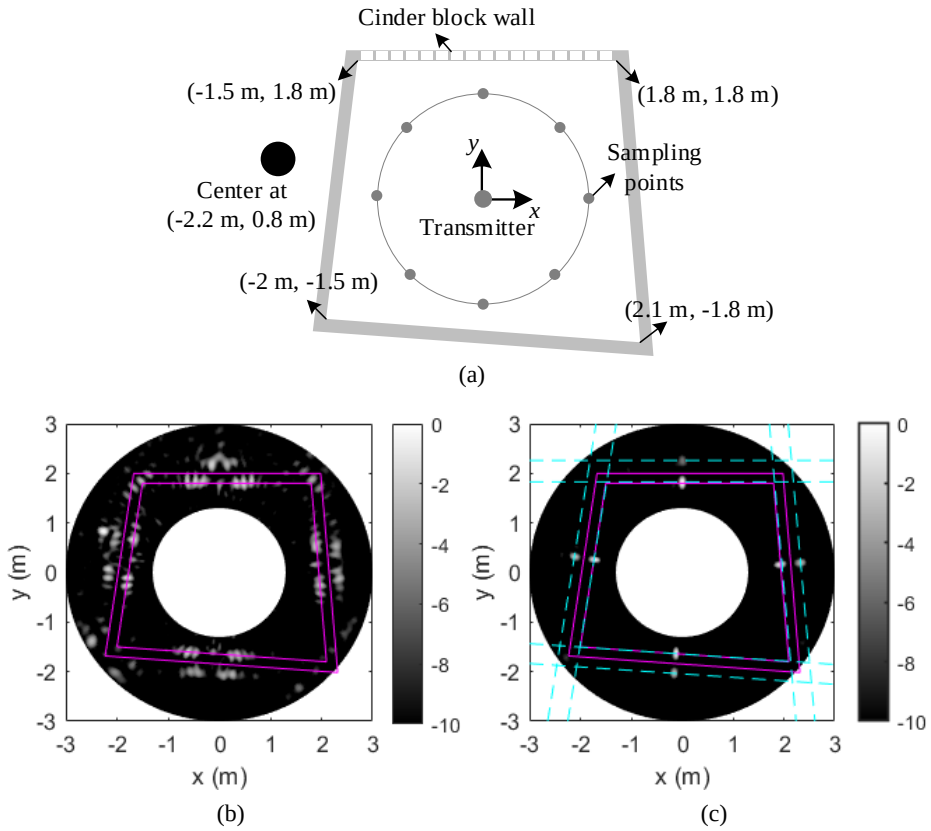

Figure 5.9. (a) Geometry of the simulated through-the-wall SAR imaging scenario. The wall located at the top is a cinder block wall. (b) Imaging using standard back-projection. (c) Result of applying the wall detection method (solid lines indicate actual walls and dashed lines indicate detected walls) [17].

electric line source and located at the origin. The object behind the wall is an infinite PEC cylinder with the radius of 15 cm. Using isotropic receivers, the scattered fields are sampled at 91 equally spaced points distributed on a circle with radius of 1.25 m centered at the transmitter location. The scattered fields are obtained by COMSOL 2-D simulations at 81 frequency steps within the range 1.2−2 GHz. Applying the back-projection to the simulated data results Figure 5.9(b) in which walls and the object are imaged. However, the walls are imaged as discrete points. Figure 5.9(c) shows the image (in polar format) obtained by applying the wall detection method to the simulated data. It can be observed that all walls (including cinder block wall) surfaces are detected and in contrast, the small object which does not provide large specular reflections for majority of sampling points is not imaged. In Fig. 5(c), the detected wall boundaries are indicated by dashed lines. The shift

observed in position of outer wall boundaries is due to the propagation of waves inside the walls which is not compensated for.

5.3.3. Applying the Proposed Wall Detection Method to the Measured Data

To evaluate performance of the introduced wall detection method in real scenarios, the method is applied to two measured through-the-wall imaging datasets obtained using the fabricated FMCW transmitter and receiver operating in the range 1.2–1.964 GHz (introduced in Chapter 4). Since the measurements are done using an FMCW radar system, the back-projection method presented in Chapter 4 is used instead of the standard back-projection method. For wall detection, instead of (2.1), calculated d_ns are used in (4.18) (R_t is set equal to $d_n/2$). In the imaging results presented in this section, since the wall thickness is less than the range resolution, the two boundaries of walls are not resolved.

Figure 4.10 shows the first measurement setup (described in chapter 4) in which a transmitter and a receiver form a bi-static imaging radar. Figure 5.10(a) shows the result of applying the wall detection method to the measured data. According to the obtained image, the walls are accurately detected at their real positions. In the image, a peak is detected at the location of the trihedral reflector (a point target). This is due to the fact that the specular reflections from the trihedral reflector with large RCS received at small number of sampling points is comparable with the specular reflections from the walls with low reflection coefficient received at most of the sampling points. However, the peak at the trihedral reflector location is well below the peaks detected at walls locations. In the measurement setup for Figure 5.10(a), using orthogonal circular polarizations, the polarization isolation between transmitter and receiver is 18 dB. To evaluate performance of the method in presence of strong coupling between transmitter and receiver, the

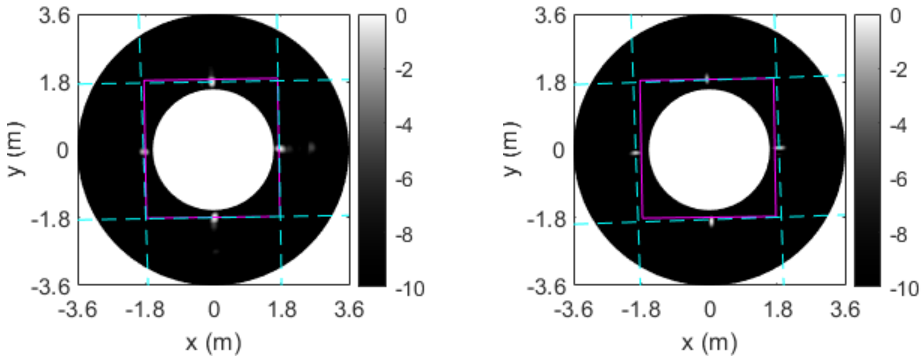

(a) (b)

Figure 5.10. Wall detection result for the measurement setup shown in Figure 4.10. Result of applying the wall detection method to the measured data with 18 dB polarization isolation between transmitter and receiver (CP antennas) (a) and no polarization isolation between transmitter and receiver (LP antennas) (b). Solid lines show real locations of walls and dashed lines show location of the detected walls [17].

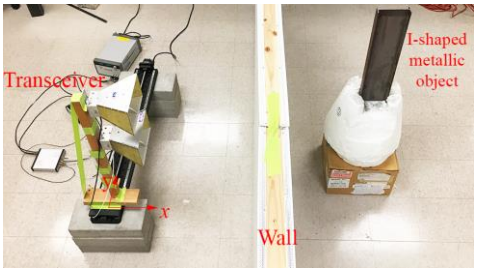

(a)

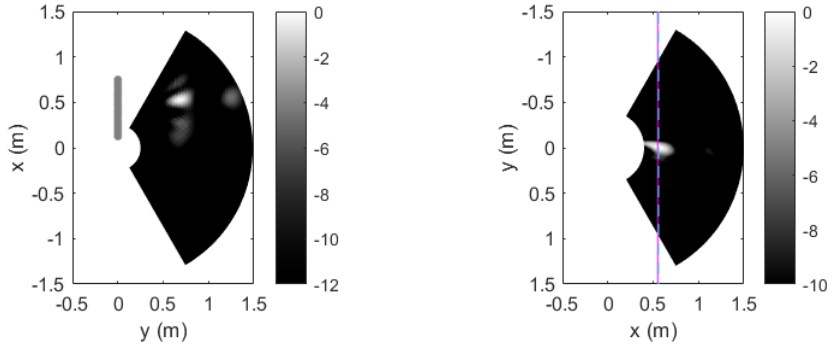

(b) (c)

Figure 5.11. (a) Measurement setup for monostatic SAR imaging. (b) Image (in dB) obtained by applying back-projection (Sampling points are indicated by gray dots). (c) Result of applying the wall detection method to the measured data. Solid line shows real location of the wall and dashed line shows location of the detected wall [17].

same measurement is repeated using vertically polarized antennas with no polarization isolation and the result of applying the wall detection method is shown in Figure 5.10(b). It can be observed that all walls are detected even in the presence of strong coupling between transmitter and receiver.

Figure 5.11(a) shows a measurement setup for monostatic SAR imaging. In the measurement setup, an I-shaped metallic object is placed behind a wall formed by two layers of

drywall with thickness of 1 cm and separation of 9 cm. Total of 26 samples with separation of 2.5 cm are collected along a line parallel to the wall using a precision linear actuator. The distance between the wall and the sampling points is 55 cm. Figure 5.11(b) shows the imaging result obtained by back-projection. It can be observed that both the wall and the metallic object behind the wall are imaged. However, the wall is imaged as discrete points. Figure 5.11(c) shows the result of applying the wall detection method to the measured data. According to the obtained image, the wall is accurately detected. In Figure 5.11(c), the object behind the wall (with limited size) is not detected since it does not provide specular reflection for a large number of sampling points within the formed aperture.

5.4. Conclusion

In this chapter, two methods for imaging enhancement in through-the-wall SAR imaging have been introduced.

The first method improves the range resolution of the SAR image and reduces the background noise and spurious images resulted from unresolved multi-path and unsuppressed sidelobes. Based on generalized pencil of function (GPOF) algorithm, the method detects the location of reflections which are objects and walls boundaries. Forming the SAR image at the detected reflecting points results in images with improved range resolution and reduced noise and spurious images. The methods presented in this chapter is applicable to stepped frequency radar data. However, its application can be extended to FMCW radar data.

In high resolution through-the-wall SAR imaging, flat walls are imaged as closely spaced discrete objects. A method for detection of walls and large flat surfaces has been presented for both multi-static and monostatic through-the-wall SAR imaging. Specular reflections from a wall

surface are equivalent to the signals received from a small fictitious object located at location of the transmitter mirrored with respect to the wall surface. Assuming that a wall surface is present in the imaging area, the image can be calculated at the location of these fictitious objects. A large intensity for the obtained image indicates that the assumed wall surface is real. Performance of the method has been evaluated through simulations and measurements in both multi-static and monostatic imaging scenarios where all walls surfaces have been detected and discriminated from objects with small size. It is shown that the method can detect walls even in presence of strong scatterers and large coupling between transmitter and receiver

Chapter 6 High Resolution Imaging of Buried Targets Using Distributed Robotic Sensors

6.1. Introduction

Inspection of the ground for detection and localization of buried objects (e.g. mines, pipelines, and cables) and subsurface features (e.g. tunnels and pipeline leaks) are sought for various military, security, civilian, and industrial applications. Current technology for detection of buried targets and subsurface features is ground penetrating radar (GPR) [75]–[77]. GPR suffers from many limitations including

1. Applicability of GPR and its penetration depth are site specific and highly depends on soil composition and moisture. According to GPR suitability map by USDA [78], soil in large areas in north, east, and west of US is not suitable for inspection using GPR.
2. GPR systems essentially utilize a monostatic transceiver with limited field of view to acquire data in a uniform grid of sampling points within the imaging area [15] (Figure 1.3). Limited field of view of GPR systems requires scanning all the points within the area under inspection in order to provide a complete image of the subsurface. Consequently, GPR inspection within large areas or long distances is a time-consuming process.
3. In conventional GPR, the data points are not processed coherently and as a result these systems suffer from low lateral resolution meaning that they are not able to resolve

closely spaced targets. To enhance subsurface imaging resolution, large antenna arrays must be used that limits mobility and increases cost of the system.

4. GPR systems must comply with the power regulations mandated by authorities. This further limits the penetration depth of the GPR system.
5. The low resolution of the images and appearance of spurious images require trained individuals to interpret radar data.

These limitations reduce the applicability and reliability of GPR in various applications and detection scenarios including

1. transportation of oil, gas, and hazardous material using pipelines: localization of old pipelines and pipeline leaks over large areas and deeply buried pipelines is of great interest for many industries including construction and oil and gas industries;
2. detection of mines and unexploded ordnance (UXO) that requires high lateral resolution imaging and operation in wide range of soil moisture and composition and depth;
3. detection of deeply submerged features such as perimeter breaches tunnels that is required in security operations.

Despite the aforementioned limitations, GPR is the only technology that is widely used for underground inspection and imaging in infrastructure development, mining, archaeology, construction, and industry.

To enhance cross-range resolution, GPR systems utilizing SAR technique have been introduced. These systems are either forward looking or downward looking and are mounted on vehicles or drones [79]–[81]. In these systems, the data collection is still a time-consuming process (data are collected on grids within the imaging area). To reduce data collection time, compressive

sensing method have been developed for SAR and GPR imaging to reduce the number of samples that are required to be collected [82], [83]. However, these methods mainly detect the presence of targets and cannot provide accurate shape of the targets [84].

In this chapter, a new subsurface imaging technique based on SAR imaging utilizing bi-static transmitters and receivers is proposed to provide images of buried targets with a high lateral resolution in a short period of time. Transmitter is located at the center of the imaging area and one or more receivers move around the transmitter and sample the reflected signals at different locations (sampling points). By combining the sampled signals using a beam-forming technique, a large 2-D synthetic aperture is formed to obtain images with a high lateral resolution. Eliminating the need for employing large antenna arrays for achieving high lateral resolution enhances the system mobility and as a result the transmitter and receivers can be mounted on ground robots or drones for autonomous data collection specifically in hazardous areas such as mine-fields. The proposed method, in contrast to GPR, does not require sampling of the reflected signals on a grid and only samples on a circle centered at transmitter location are sufficient to form the image within the circle. This makes the data collection and imaging formation fast.

6.2. Image Formation Technique

According to Figure 6.1, in the new subsurface imaging method, a stationary transmitter equipped with a wide beamwidth antenna illuminates a wide subsurface area and at least one moving receiver samples the scattered signals on a circle with center at the transmitter location. Assuming that a stepped frequency continuous wave (SFCW) radar is utilized for acquiring the samples at N frequency steps and M locations, the image at different subsurface points is obtained by applying back-projection as follows

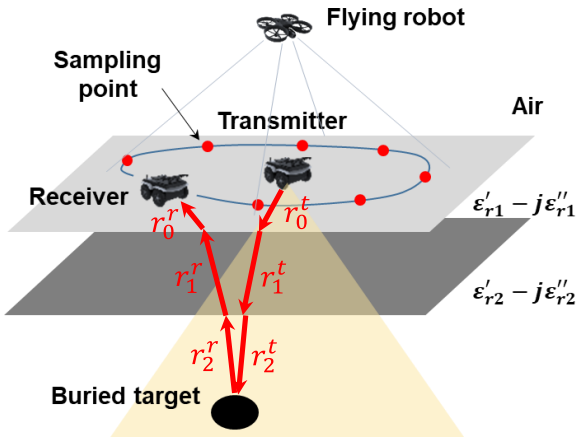

Figure 6.1. Arrangement of transmitter and receiver in the proposed subsurface imaging method.

$$I(r) = \sum_{m=1}^{M} \sum_{n=1}^{N} S_{mn} \prod_{l=0}^{L} e^{jIm(\gamma_{nl})(r_l^t + r_l^s)}. \tag{6.1}$$

In (6.1), L indicates the number of soil layers and layer 0 indicates air. γ_{nl} is the complex propagation constant for the lth layer at nth frequency step. S_{mn} is the frequency response obtained at nth frequency step and mth sampling point. As illustrated in Figure 6.1, r_l^t and r_l^s are the distances that constant phase planes travel inside the lth layer from the transmitter to the image point and from the image point to mth sampling point, respectively. Knowing the relative position of transmitter and receiver for each sampling point and complex permittivity of soil layers, $r_l^{t,s}$s can be calculated using a ray-tracing method. In the proposed method, a flying robot taking photos of transmitter and receiver or a LIDAR mounted on the transmitter can be used to detect relative location of the transmitter and receiver.

Assuming the air-ground interface is illuminated by a plane wave with angle of incidence of $\theta_{p,0}$ as shown in Figure 6.2, the direction of propagation for the constant phase planes in the lower medium (one-layer lossy soil), $\theta_{p,1}$, is calculated by

$$\theta_{p,1} = \tan^{-1}\left(\frac{k_0 \sin\theta_{p,0}}{Im(\gamma_1 \cos\theta_1)}\right), \tag{6.2}$$

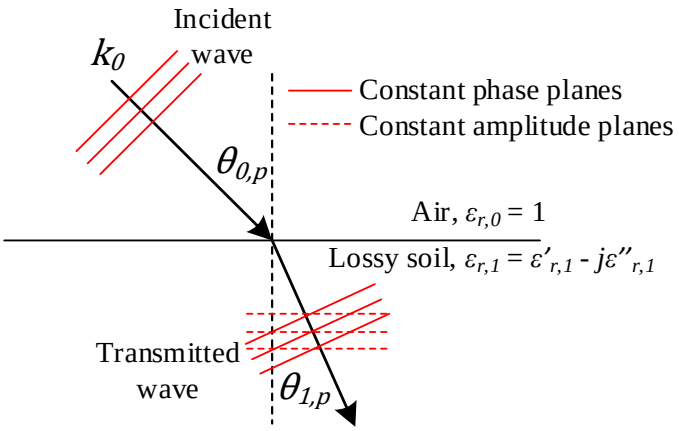

Figure 6.2. Transmission at air-lossy ground interface.

where k_0 is the phase propagation constant in air and γ_1 is the complex propagation constant of the lower medium. k_0 and γ_1 are defined by

$$k_0 = \frac{2\pi}{\lambda_0} \tag{6.3a}$$

$$\lambda_1 = j\frac{2\pi}{\lambda_0}\sqrt{\varepsilon_{r,1}}\,. \tag{6.3b}$$

In (6.3), λ_0 is the free-space wavelength and ε_1 is the complex relative permittivity of the lower medium. In (6.2), $\cos\theta_1$ is a complex value and is calculated by

$$\cos\theta_1 = \sqrt{1 - \frac{1}{\varepsilon_{r,1}}\sin^2\theta_{0,p}} \tag{6.4}$$

In practice, the permittivity profile of soil is unknown and must be estimated. This can be done by assuming a permittivity profile for the soil and then applying an optimization algorithm modifying the permittivity profile to sharpen the image.

6.3. Frequency of Operation

To achieve high range resolution, frequency bandwidth of the transmitted signal must be large. However, due to the large attenuation in soil at high frequencies, operation at high

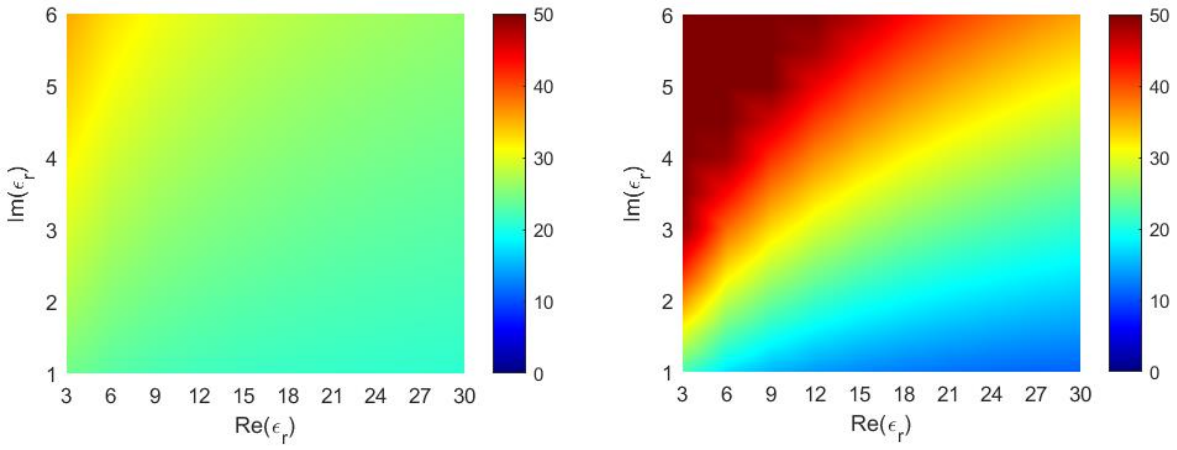

Figure 6.3. Attenuation in one-layer soil at depth of 1 m for different values of real and imaginary parts of soil permittivity. (a) At 100 MHz. (b) At 500 MHz.

frequencies to increase the bandwidth is not feasible. In subsurface imaging, the maximum frequency of operation must be determined according to the maximum buried depth of targets. To investigate the effect of soil complex permittivity on the amplitude of signals traveling to the maximum depth, a one-layer soil model (half-space) and a horizontal infinitesimal dipole (transmitter) is considered. Figure 6.3 shows the one-way attenuation at depth of 1 m (a typical buried depth for pipelines) at 100 MHz and 500 MHz for different values of the real and imaginary parts of soil permittivity. The attenuation is defined as the ratio of the amplitude of the signal at depth of 1 m (normal incidence) to the amplitude of the signal at air-ground interface while the soil layer is replaced by air. With this definition and the selected source, calculated attenuation includes loss in the soil as well as transmission coefficient at air-ground interface and path loss due to the spread of power. It can be observed that increasing the operation frequency increases the attenuation in soil. However, for a wide range of soil types and soil moisture content, the attention at 1 m is less than 35 dB for frequencies up to 500 MHz (resulting maximum two-way path loss of 70 dB). For the application of pipeline localization and leak detection, the frequency range 150–450 MHz is selected for image formation. It is noted that reducing the minimum

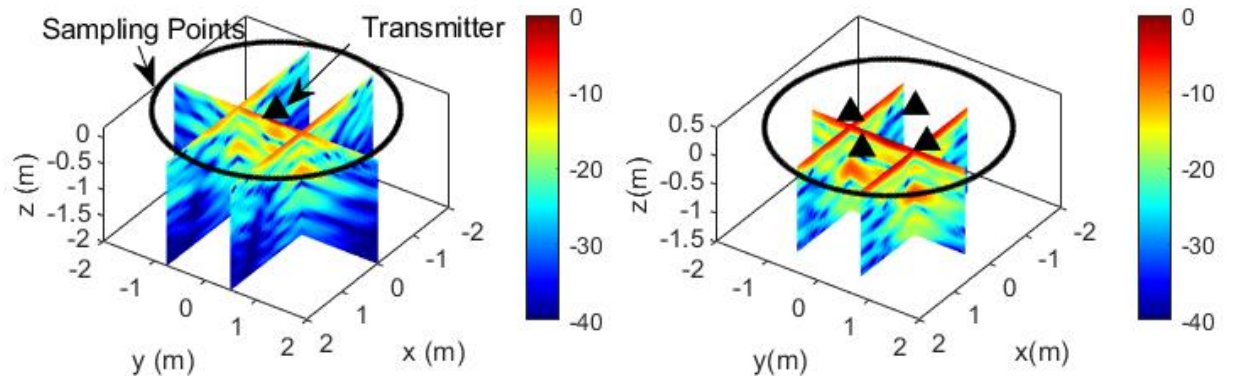

(a) (b)

Figure 6.4. Simulation results for two metallic spheres with centers at (0, 0.5 m, -0.9 m) and (0, -0.75 m, -0.9 m). (a) Imaging result (in dB) using one transmitter. (b) Imaging result using four different locations for the transmitter.

frequency to increase the bandwidth is not possible since it requires utilizing large antennas which is not practical.

6.4. Applying the Imaging Method to the Simulated Data

To evaluate performance of the proposed subsurface imaging technique, two metallic spheres with radius of 10 cm are assumed to be buried in half space z<0 with complex permittivity of $3-j0.06$ (dry soil). Assuming a Hertzian dipole transmitter and isotropic receivers at the height of 10 cm from the ground surface, the resulting scattered fields are calculated using FEKO full wave simulations at 90 sampling points equally distributed on a circle with radius of 2 m and center at the transmitter location. The image obtained by applying (6.1) to the simulated data over the band 150–450 MHz is shown in Figure 6.4(a). It can be observed that both spheres are clearly imaged at the depth of 0.8 m which is the location of the most top part of the spheres. Figure 6.4(b) shows the image formed by scattered fields that are obtained using 4 different locations for the transmitter. It can be observed that illuminating the subsurface from different locations improves the image contrast (spheres are imaged with a higher intensity). Consequently, in the imaging system realizing the proposed imaging method multiple transmitter are used. Using multiple

transmitters requires separate measurement of scattered fields due to each transmitter which significantly increases the data collection time. To measure the scattered fields due to each transmitter while all transmitters are operating simultaneously and reduce the data collection time, a technique similar to orthogonal frequency division multiplexing (OFDM) is introduced in Chapter 8.

6.5. Evaluation of the Imaging Method in a Real Scenario

To evaluate performance of the proposed imaging technique in a real scenario, a field measurement is performed in which a metallic sphere with diameter of 36 cm is buried at depth of 0.9 m in Michigan's dense soil as shown in Figure 6.5(a). Using the antenna designed for imaging system (introduced in Chapter 7) for both transmitter and receiver and a portable vector network analyzer (VNA), the scattered fields are measured over the band 150–450 MHz at 24 sampling points uniformly distributed on a square with sides of 4 m (the circular profile for sampling points locations is replaced by a rectangular profile to simplify the positioning of the antennas). Figure 6.5(b) shows the result of applying (6.1) to the measured data assuming constant complex permittivity of $4-j0.5$ for the soil. It can be observed that the sphere is clearly imaged at the depth of -0.7 m which is the location of the most top part of the sphere. Unlike GPR systems with low lateral resolution, image of the sphere is not a parabola in Figure 6.5(c). This indicates the high lateral resolution of the imaging method.

Figure 6.5(c) shows the peak to average value of the image in the range -0.5 m $< x <$ 0.5 m and -1 m $< z <$ -0.3 m at y = 0 plane versus real and imaginary part of the soil permittivity assuming one-layer soil model. According to the results, the complex permittivity of $4-j0.5$ provides the highest peak to average value (highest contrast) in the image. Considering the

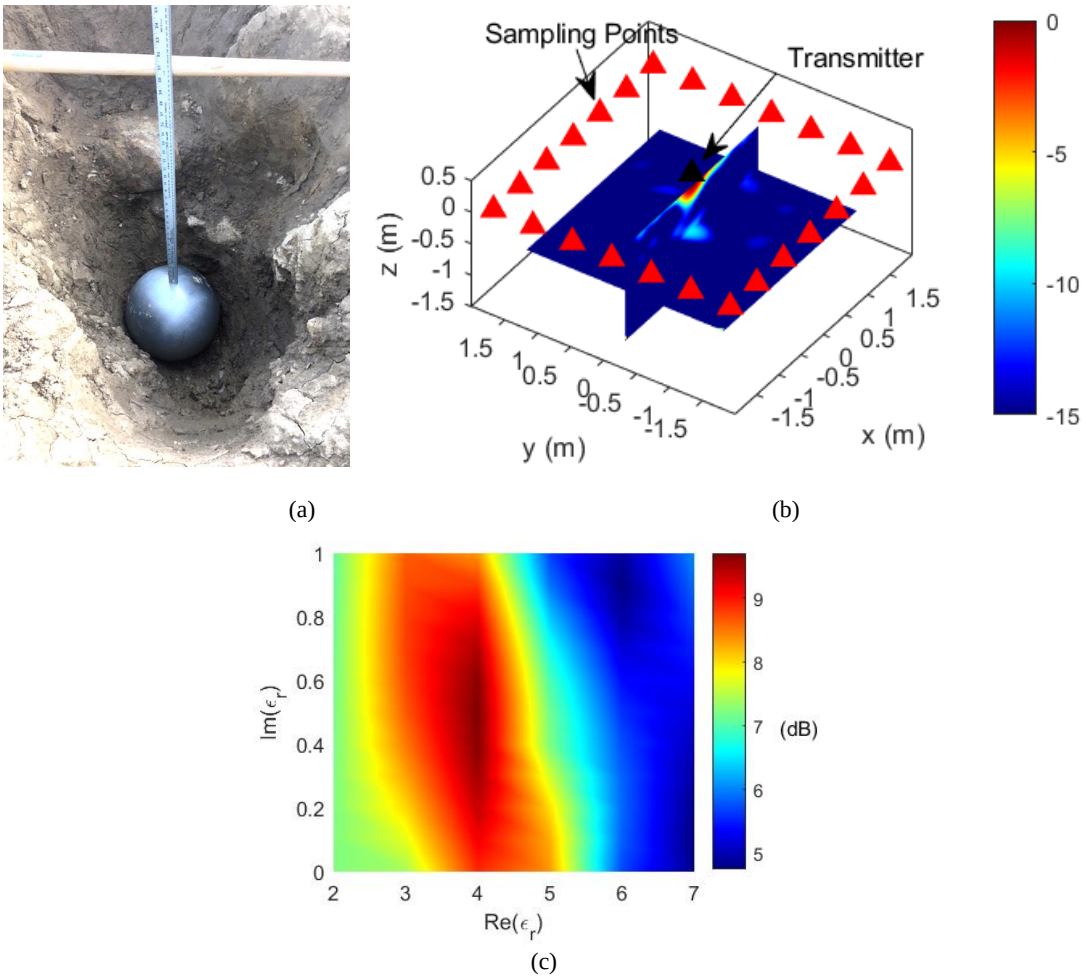

Figure 6.5. Field measurement. (a) Metallic sphere with diameter of 36 cm buried at the depth of 0.9 m. (b) Imaging result (in dB). (c) Peak to average value of the image in the range -0.5 m $< x <$ 0.5 m and -1 m $< z <$ -0.3 m at y = 0 plane versus real and imaginary part of the soil permittivity.

obtained value as the real soil permittivity, the formed image in Figure 6.5(b) provides the exact location of the object.

6.6. Conclusion

A new high resolution subsurface imaging method has been introduced to address low lateral resolution, limited field of view, and low mobility of currently available GPR systems. The method employs at least one robotic transmitter and one or more robotic receivers in a bi-static configuration to acquire scattered field from buried targets and subsurface features at limited

number of points around the transmitter. Using back-projection and a ray-tracing method, the acquired samples are coherently processed to create a large 2-D synthetic array that provides high resolution 3-D images of the subsurface. Performance of the method has been investigated through numerical simulations and a field measurement is presence of dense soil.

Chapter 7 Low Profile, Low Frequency, UWB Antenna for Imaging of Deeply Buried Targets

7.1. Introduction

In GPR systems, obtaining high range (depth) and cross range-resolution images requires a wide operation bandwidth for the system and a wide aperture for the antennas, respectively. For shallowly buried targets, the center frequency of operation can be increased to simplify the design of wideband GPR systems and obtain large aperture electrically while keeping the physical size of antennas small. However, for deeply buried targets, increasing the frequency of operation will adversely affect detection because of high signal attenuation at high frequencies in soil. Figure 7.1 shows the penetration depth, defined as one-way attenuation of 35 dB, versus frequency inside a wet soil with a fixed complex permittivity of $16.4-j2.4$ (this is a measured value for complex permittivity of a sample of Michigan's dense and wet soil as discussed in Section 7.4). It can be observed that increasing frequency of the transmitted signal reduces the penetration depth and consequently the maximum depth a given target can be detected.

Antennas are critical components of GPR systems. In addition to typical antenna parameters such as gain and radiation pattern, dispersion, direct coupling between transmitting and receiving antennas, and radiation characteristics in proximity of the ground are other important parameters for antennas in GPR systems. Horn, Vivaldi, spiral, bow-tie, and TEM horn are common types of UWB antennas employed in GPR systems [1]. Among all, bow-tie [85]–[88] and TEM horn antennas [89], [90] are suitable for impulse GPR systems where the low-dispersion

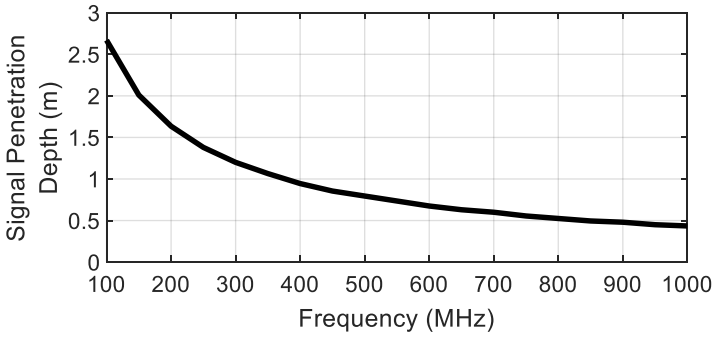

Figure 7.1. Signal penetration depth versus frequency for signal attenuation of 35 dB in wet soil with constant complex permittivity of $16.4-j2.4$. Source is a Hertzian dipole located at the height of 0.2 m above the air-ground interface [18].

(linear phase) response is required for the antennas. However, they require resistive end-loading to reduce time-domain ringing effect and achieve wideband operation [1], [85], [90], which reduces the antenna gain. Bow-tie is a low-profile antenna structure that is widely used in GPR systems. The significant backside radiation of bow-tie antennas is reduced by using cavity or reflector structures on the backside of the antenna [86]–[88]. These structures can be designed to achieve a better front-to-back ratio for the bow-tie antenna at the cost of increase in total height and reduction in the bandwidth of the antenna.

Wideband operation at low frequencies and constraints on the size and weight of the antennas for mobility, make the antenna design a challenging task for achieving high range-resolution for GPR systems intended for imaging of deeply buried targets. In this chapter, a low-profile UWB antenna operating at frequencies below 500 MHz for GPR applications is introduced.

7.2. Antenna Structure

Geometry of the proposed antenna element is shown in Figure 7.2. It resembles a bisected TEM horn antenna whose lower part is replaced by a ground plane. A shorting plate connects the end of the TEM horn to the ground plane. According to Figure 7.2, instead of a linear profile originally used in [91], exponential tapering is used here for the TEM horn section in both x and

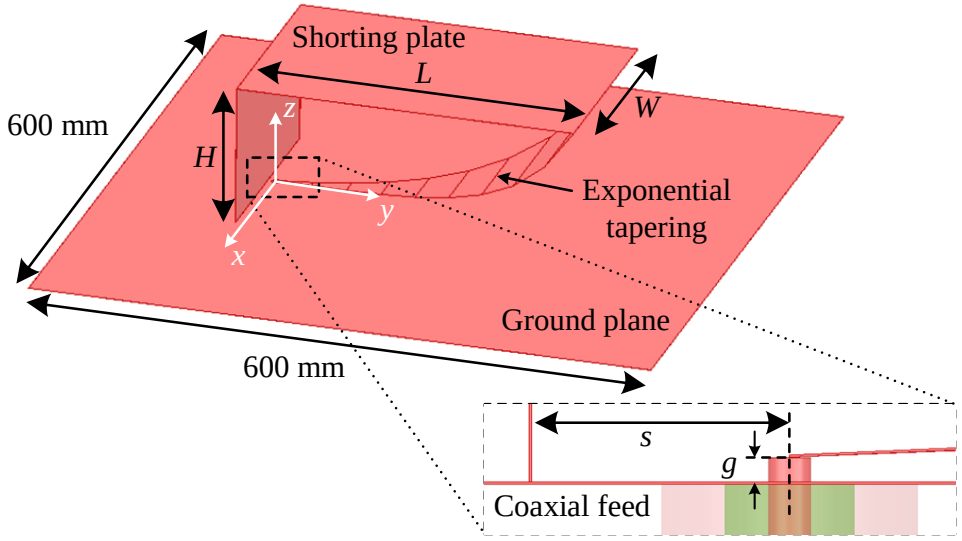

Figure 7.2. Modified ENVELOP antenna structure (optimized for maximum -10 dB impedance bandwidth) [18]. The exponential tapered section is approximated by 10 linear sections with equal lengths along y.

z directions to increase the impedance bandwidth. Assuming the origin is located at the feed point on the ground plane, the tapering functions is parameterized as

$$x = \pm\left(\frac{W}{2}\right)\left(\frac{e^{B_x t} - 1}{e^{B_x} - 1}\right) \tag{7.1a}$$

$$y = (L - s)t \tag{7.1b}$$

$$z = (H - g)\left(\frac{e^{B_z t} - 1}{e^{B_z} - 1}\right) + g, \tag{7.1c}$$

where t is varied from 0 to 1 and B_x and B_z define the taper profile in x and z direction, respectively. With the defined profile in (7.1), varying B_x and B_z does not change the tapered section and shorting plate total height (H) and width (W). According to Figure 7.2, L is the total length of the shorting plate along y, g is the gap between the tapered section and ground plane at the feed point, and s is the distance between the feed point and the shorting plate. To simplify fabrication of the antenna, a piecewise linear approximation with 10 sections is used for the tapered

section as shown in Figure 7.2. In this figure, the nth section's vertices (n = 1, 2, 3 …, 10) are defined by (7.1) while t is equal to $(n-1)/10$ and $n/10$.

Figure 7.2 shows the geometry of the antenna structure that provides the highest -10 dB impedance bandwidth for a specified dimension for the ground plane. The ground plane size is limited to be 600 mm × 600 mm for accommodating a pair of coupled antennas. The values for geometrical parameters are L = 325 mm, W = 200 mm, H = 150 mm, B_x = 2, B_z = 4, g = 0.81 mm (= 32 mil), and s = 8 mm. The antenna and the ground plane are formed by copper sheets with the thickness of 70 μm. The antenna is simulated in ANSYS HFSS full-wave 3D EM simulator. For all simulations in this chapter, the antenna is placed at the distance of 10 cm from the ground (dry soil) with the complex permittivity of $3.5-j0.0374$ (according to [92], the complex permittivity of dry soil is approximately independent of temperature and frequency; its real part varies in the range 2–4; and its imaginary part is less than 0.05).

Figure 7.3(a) shows the simulated reflection coefficient for the antenna in Figure 7.2 in presence of the ground. The -10 dB impedance bandwidth of antenna covers the range 180–500 MHz. Figure 7.3(b) shows the simulated realized gain pattern at 300 MHz in which the main lobe is skewed from the boresight direction and therefore the antenna is not perfect for GPR applications. In Section 7.3, a structure composed of two coupled modified ENVELOP antennas is utilized to correct for the radiation pattern and also improve the impedance bandwidth.

7.3. Coupled Modified ENVELOP Antennas

To improve the bandwidth and correct for the radiation pattern of the single antenna shown in Figure 7.2 an array of two modified ENVELOP antennas is utilized. Geometry of the proposed antenna structure is shown in Figure 7.4 in which the second antenna is a rotated copy (around z-

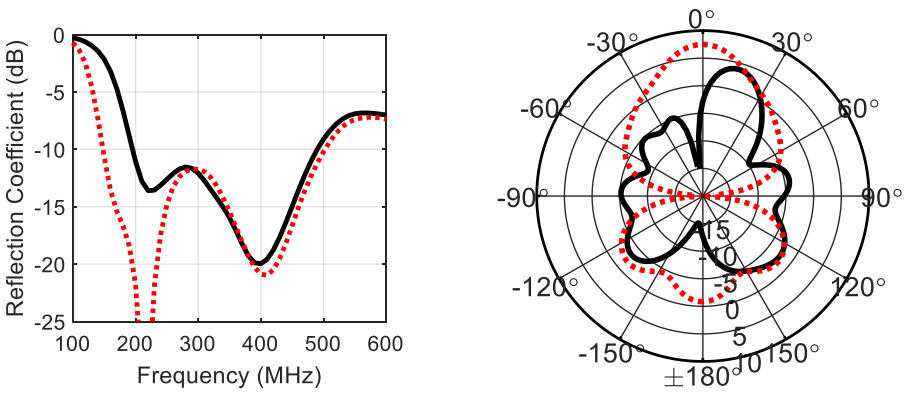

(a) (b)

Figure 7.3. Simulation results for the antenna in Figure 7.2 (solid line) and Figure 7.4 (dotted line) [18]. (a) Reflection coefficient (dB). (b) Realized gain (dBi) in yz-plane at 300 MHz.

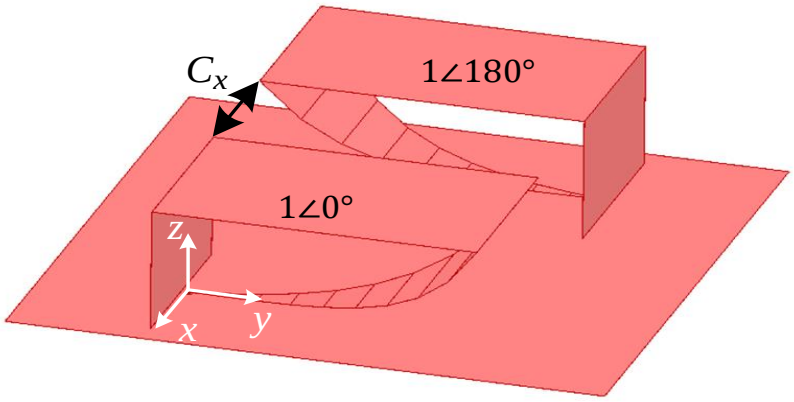

Figure 7.4. Coupled modified ENVELOP antennas [18].

axis) of the first antenna. Separation between two antennas is denoted by C_x. The antenna elements are excited with the same amplitude and 180° phase difference to allow for the flow of current in the same direction on both modified ENVELOP antenna elements. Depending on the separation, different levels of magnetic coupling between the two elements occurs that can be used to compensate for capacitive reactance of the input impedance and obtain better impedance match and wider impedance bandwidth. In this configuration, it is expected that the combined pattern be symmetric in yz-plane and the direction of maximum radiation be normal to the ground plane. Modeling the antenna as a two-port network, the reflection coefficient seen from each port for out-of-phase excitation is defined by $20\log_{10}(|S_{11} - S_{12}|)$. Figure 7.3(a) shows the simulation result

for reflection coefficient of the antenna shown in Figure 7.4 when placed near a half-space dry soil medium. Comparison between the results shown in Figure 7.3(a) shows that the -10 dB impedance bandwidth of the new antenna is increased. According to Figure 7.3(b) (realized gain pattern in yz-plane at 300 MHz), the antenna in Figure 7.4 exhibits a larger gain (comparing to the antenna in Figure 7.2) with the main lobe in the direction normal to the ground plane. As a result, the antenna in Figure 7.4, can provide a wide impedance bandwidth and the required directive pattern by GPR applications.

7.4. Antenna Fabrication and Measurement Results

The antenna structure shown in Figure 7.4 with the optimum parameters L = 325 mm, W = 200 mm, H = 150 mm, B_x = 2, B_z = 4, g = 0.81 mm (= 32 mil), s = 8 mm, and C_x = 150 mm and ground plane size of 600 mm × 600 mm is fabricated. The antenna is optimized for widest -10 dB impedance bandwidth in the presence of dry soil at the distance of 10 cm from the shorting plate surface. FR-4 substrate with dielectric thickness of 60 mil, relative permittivity of 4.3, and copper thickness of 70 μm is used for the ground plane and RO4003 substrate with dielectric thickness of 32 mil, relative permittivity of 3.55, and copper thickness of 70 μm is used for the tapered section and shorting plate.

The parametric analyses for the reflection coefficient and realized gain are shown in Figure 7.5 for the antenna in Figure 7.4. According to Figure 7.5(a) and Figure 7.5(b), increasing B_x or decreasing B_z increases the impedance bandwidth. However, large values for B_x or small values for B_z, increases the reflection coefficient at mid-band frequencies. According to Figure 7.5(c), increasing L shifts the impedance bandwidth to lower frequencies. Parametric analyses for H in Figure 7.5(d) show that increasing H widens the impedance bandwidth. However, in a low-profile

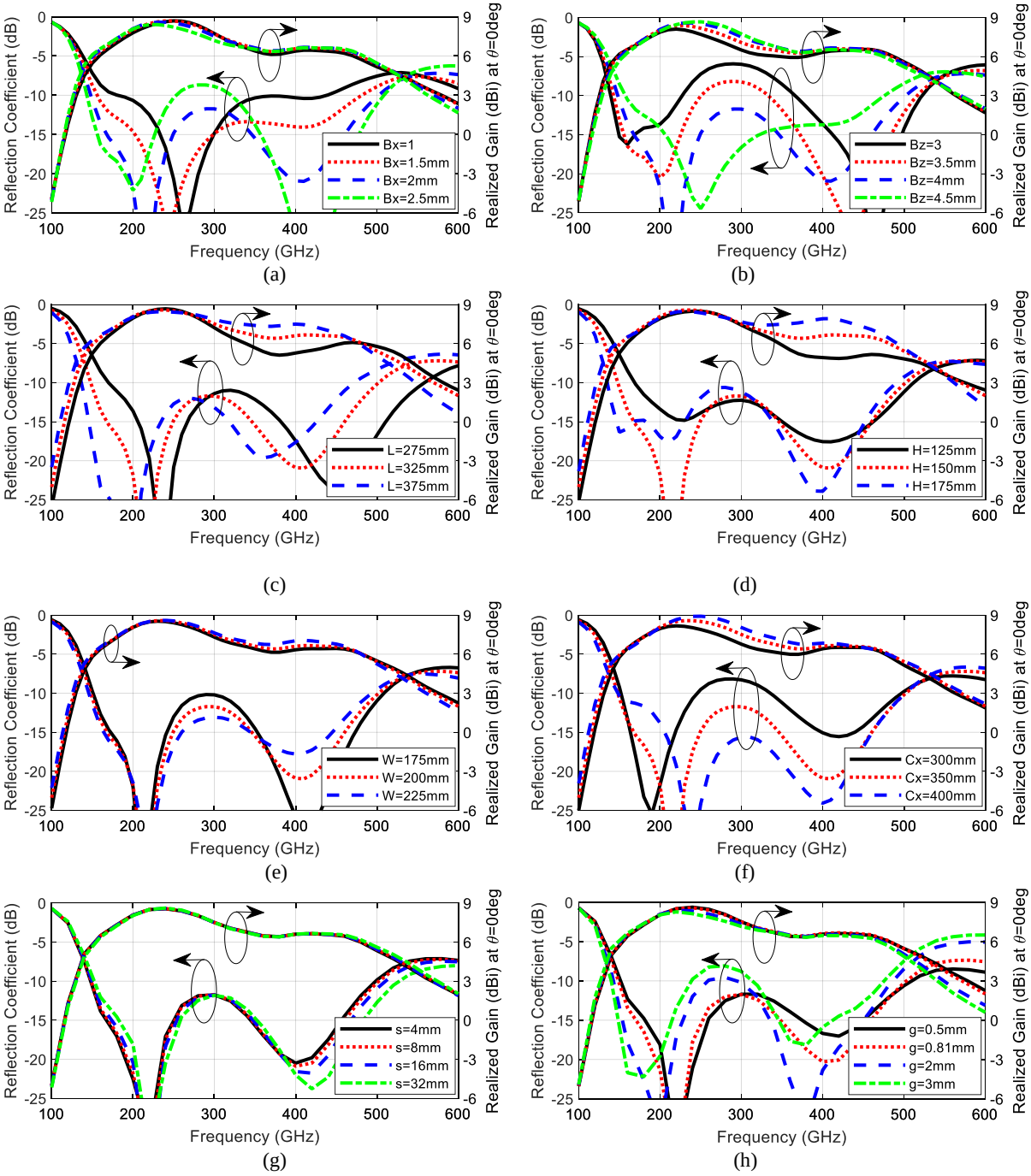

Figure 7.5. Reflection coefficient and realized gain (at θ = 0°) for the antenna in Figure 7.4 for different values of (a) B_x, (b) B_z, (c) L, (d) H, (e) W, (f) C_x, (g) s, and (h) g [18].

antenna, H cannot be a large value. As shown in Figure 7.5(e), increasing W improves matching and gain over the impedance bandwidth. According to Figure 7.5(f), increasing C_x improves gain and matching over the impedance bandwidth. However, for a fixed size for the ground plane, C_x

is limited. Increasing s widens the impedance bandwidth and slightly shifts that to the higher frequencies (Figure 7.5(g)). Large g shifts impedance bandwidth to lower frequencies while increases the reflection coefficient at mid-band frequencies (Figure 7.5(h)).

For the final antenna structure, size of the ground plane and H are determined by the limitations on the size of the antenna. The parameter g is selected to be equal to the thickness of tapered section substrate to make adjusting the gap at feed location simple and more accurate (the required gap is obtained if bottom of the dielectric of the tapered section substrate touches the ground plane). s in the range 4–16 mm results in approximately the same performance for the antenna (Figure 7.5(g)) but larger values for s makes mounting the connector easier in antenna fabrication.

Figure 7.6 shows the antenna CAD model and the fabricated antenna. Two vertical support structures (fabricated using RO4003 substrates with the same piecewise linear profile as the tapered section) are placed at the bottom of the tapered section for mechanical stability. These supporting structures are glued on the backside of the tapered section and soldered to the ground plane to make the antenna structure rigid. The antenna feed structure is shown in Figure 7.6(a). An SMA coaxial feed is connected to the tip of the tapered section at a height equal to the thickness of the substrate (g) above the ground plane. A 3-dB power divider with out-of-phase outputs (Mini-Circuits ZAPDJ2-5W-521S+) is utilized to feed the two ports of the antenna. Measurement results for the divider and the associate coaxial cables show maximum amplitude difference and maximum output phase difference deviation from 180° equal to 0.1 dB and 3°, respectively, in the range 140–510 MHz. Total height of the antenna excluding the connectors is 153 mm.

The simulated and measured reflection coefficient of the antenna in free space is shown in Figure 7.7(a). According to the simulation results for the antenna without divider (a two-port

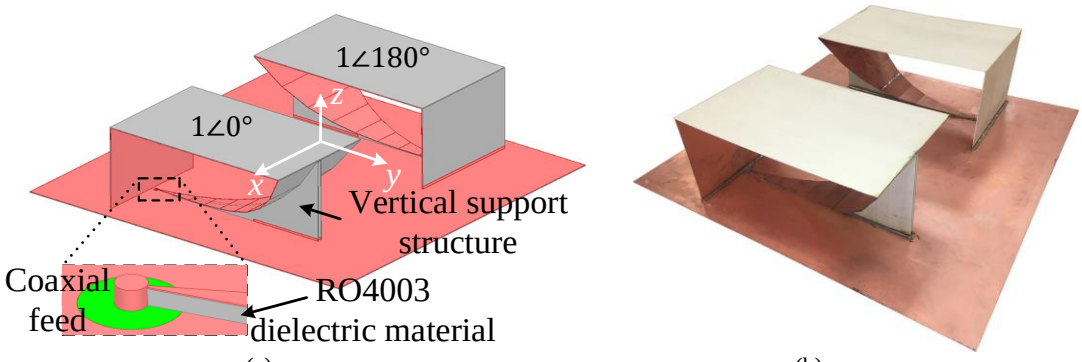

(a) (b)

Figure 7.6. (a) CAD model of the final antenna and the feed, RO4003 dielectric materials is indicated by gray color. (b) Fabricated antenna [18].

network), the reflection coefficient ($20\log_{10}(|S_{11} - S_{12}|)$) is less than -10 dB in the range 175–450 MHz. Since for the antenna with divider, the reflection coefficient includes the reflection from the divider as well as the antenna ports, according to Figure 7.7(a), the measurement result for the antenna including the divider (one port network) does not follow the simulation result. To remove the effect of reflection from the power divider and extract the reflection from the antenna ports, time domain gating is applied to the measurement results and the resulting reflection coefficient is shown in Figure 7.7(a) (dashed line) which is close to the simulation result. To evaluate performance of the antenna in proximity of a soil medium, the antenna (including the divider) is placed at the distance of 10 cm above concrete, wet soil covered by grass, and wet soil covered by sand as shown in Figure 7.7(b). Measurement results in Figure 7.7(c) show that the antenna exhibits wider impedance bandwidth in proximity of the ground. In all cases, the reflection coefficient is less than -9.5 dB over the band 140–510 MHz.

The antenna is measured in anechoic chamber of the University of Michigan at frequencies above 200 MHz. Figure 7.8 shows the measured and simulated realized gain of the antenna in free space and simulated realized gain in the presence of dry soil. Simulation results show that the antenna provides larger realized gain in presence of dry soil at frequencies less than 400 MHz and its simulated realized gain is more than 4.9 dBi within the range 140–510 MHz. The maximum

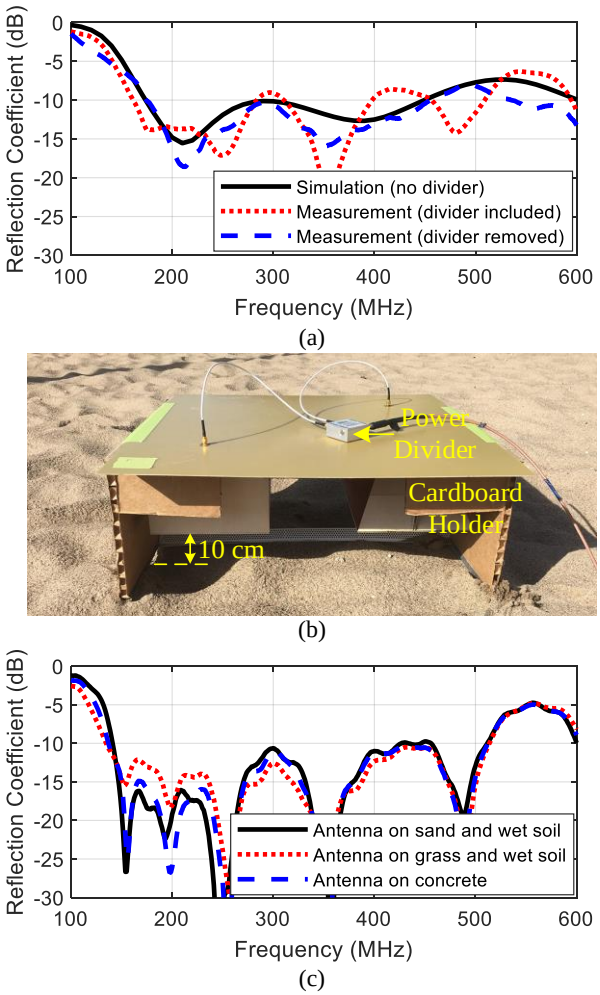

Figure 7.7. (a) Simulation and measurement results for the antenna in free space. (b) Antenna placed on wet soil covered by sand for reflection coefficient measurements. (c) Measurement results for the antenna placed on the ground [18].

difference between the simulation and measurement results in free space in Figure 7.8 is 1.6 dB which is mainly due to the errors in gain values of the reference antenna used in measurements.

Figure 7.9 shows the measured realized gain patterns in free space and simulated realized gain patterns in the presence of dry soil in xz and yz-planes at 200, 300, and 400 MHz. According to the results, the antenna provides higher gain in presence of dry soil per design. The higher soil dielectric provides a better match for power transfer to the lower medium and as a result higher bandwidth and gain can be achieved.

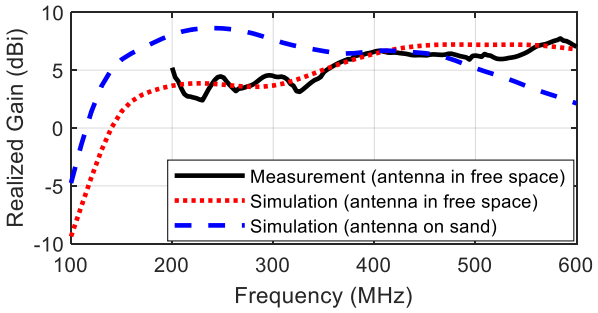

Figure 7.8. Simulated and measured realized gain of the fabricated antenna [18].

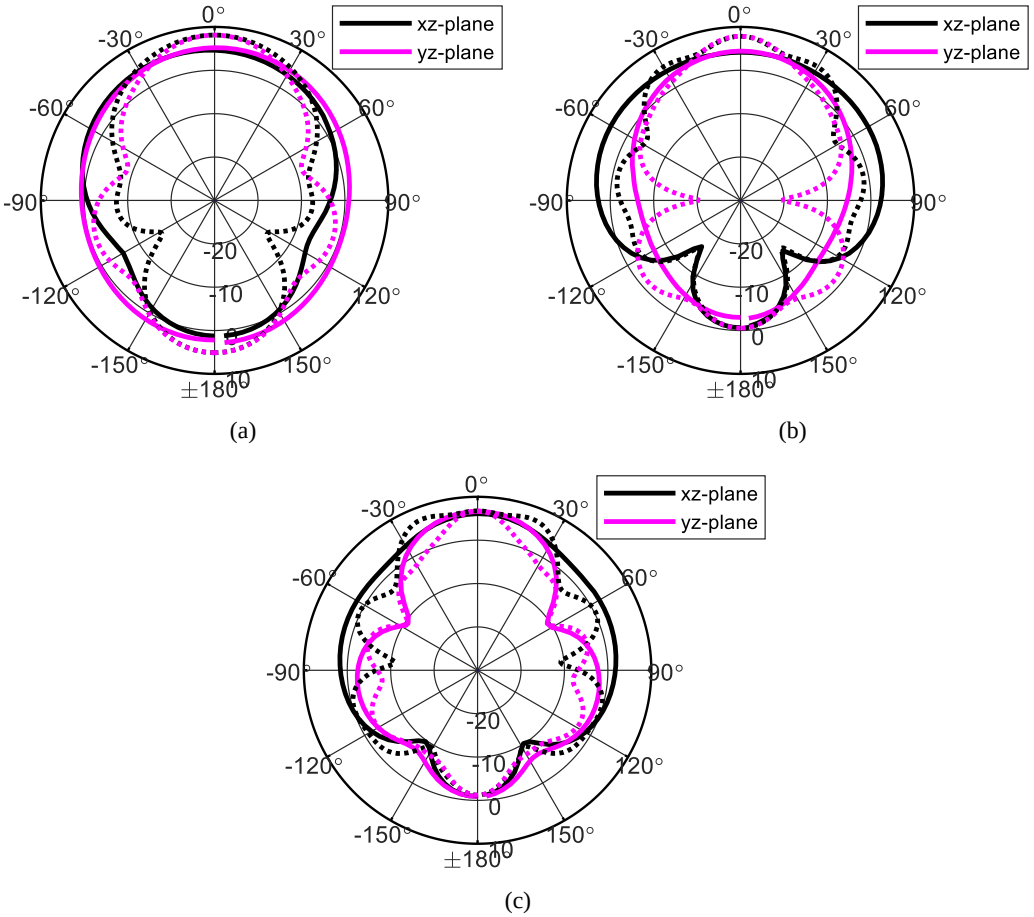

Figure 7.9. Measured and simulated realized gain pattern (dBi) in *xz* and *yz*-planes at (a) 200 MHz, (b) 300 MHz, and (b) 400 MHz (solid line: measured in free space, dotted line: simulated for the antenna placed at the height of 10 cm from dry soil) [18].

The low frequency of operation for the antenna enables more penetration depth for the signals in lossy soils and as a result the antenna can be used for imaging of deeply buried targets or targets buried in soil with high losses. To evaluate performance of the antenna in GPR applications, a metallic plate is buried in wet lossy soil, with measured gravimetric moisture

content of 18.92% and estimated dielectric constant of $16.4-j2.4$ at 300 MHz [93], [94]. Figure 7.10(a) shows the configuration of the antennas for measurement as well as the metallic plate (0.61 m × 0.762 m) buried at the depth of 0.6 m. The antennas are separated by 0.2 m (center to center distance of 0.8 m) to reduce the direct coupling. The reflected signal is measured within the range 150–450 MHz and utilized for image formation. In this measurement, the theoretical range-resolution (considering 3-dB points) in free space and in the soil medium with relative dielectric constant of $16.4-j2.4$ is 0.435 m and 0.107 m, respectively. The imaging result is shown in Figure 7.10(b). It can be observed that the plate is imaged at the depth of 0.57 m. The imaging result at the location of the center of the plate shown in Figure 7.10(c) indicates that the obtained range-resolution is 0.101 m which is close to the theoretical value. By applying a ray-tracing method, the path for the signal reflected from the plate can be determined. According to the ray-tracing (described in Chapter 6) result shown in Figure 7.10(d), time delay for the direct signal from transmitter to receiver, the signal reflected from air-ground interface, and the signal reflected from the plate is 2.67, 2.75, and 18.53 ns, respectively. According to the obtained time delay values, the direct signal and the signal reflected from the air-ground interface cannot be resolved since their free space path length difference is below the range-resolution. The calculated time delay difference between the direct signal and the signal reflected from the plate is 15.86 ns which is in accordance with the image presented in Figure 7.10(b) (the measured time delay difference between the direct signal and the signal received from the plate is 15.2 ns).

Assuming that the transmitted power and target size remain constant, the depth at which the target provides the same scattered field amplitude as the one obtained in the measurement (at 450 MHz at which the attenuation is maximum) is calculated using HFSS simulations. According

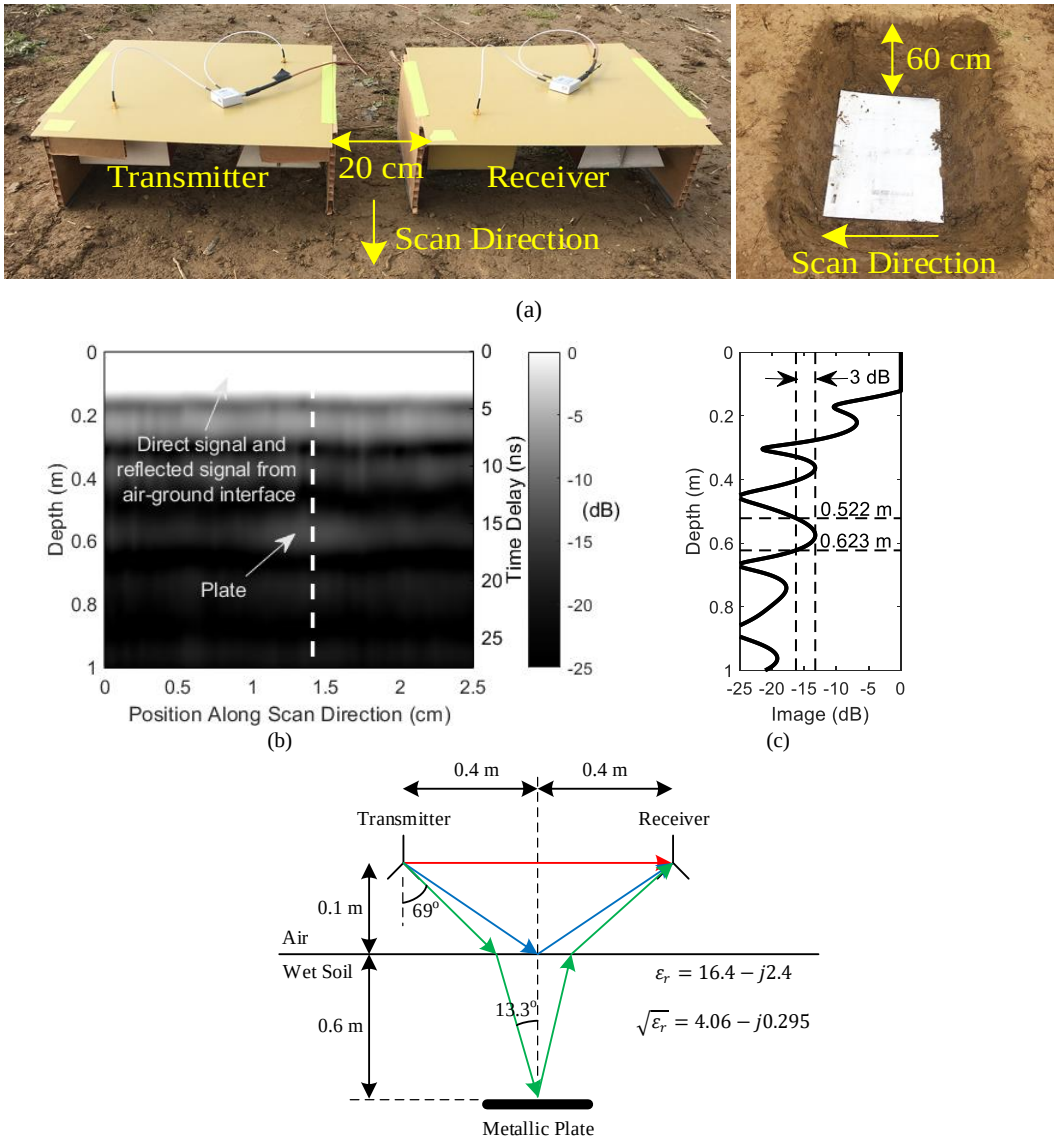

Figure 7.10. Evaluation of performance of the antenna in a GPR application [18]. (a) Configuration of the antennas and buried metallic plate in wet soil. (b) Imaging result (time delay is shifted such that the delay for the direct signal is zero) for all positions along the scan direction. (c) Image at the location of the plate along the dashed line shown in (b). (d) Ray-tracing result for different signals received at the receiver.

to simulation results the detection depth is increased to 0.8 m and 2.8 m for soil complex permittivity of $5-j1$ and $3.5-j0.0374$, respectively.

7.5. Conclusion

A new low profile, low frequency, UWB antenna for GPR applications has been introduced. The antenna is formed by an array of two modified ENVELOP antennas to provide directive radiation pattern normal to the antenna ground over a wide bandwidth. When placed above the ground, the reflection coefficient of the antenna in less than -9.5 dB and its realized gain is more than 4.9 dBi over the frequency range 140–510 MHz. Total height of the fabricated antenna excluding the connectors is 153 mm. The low frequency of operation of the antenna enables imaging of deeply buried targets or imaging in soil with high losses. The performance of the proposed antenna has been evaluated through a field measurement on wet soil with high losses.

Chapter 8 Radar System Realizing High Resolution Subsurface Imaging Using Distributed Robotic Sensors

8.1. Introduction

In this chapter, a radar system realizing the method introduced in Chapter 6 for subsurface imaging is presented and its performance is shown through simulations.

The first step in design of imaging system is selection of operation bandwidth and the center frequency of operation. Operation bandwidth is determined by the required range resolution. Center frequency of operation is mainly determined by maximum buried depth for the targets. In general, lower frequency of operation increases the maximum detection depth but it requires larger physical size for the antennas that limits mobility. In the system design, assuming buried depth of 1 m for the targets, the frequency of operation has been selected to be in the range 150−450 MHz (according to the Section 6.3).

Configuration of transmitters and receivers in the imaging method requires a bi-static radar system. According to the imaging results in Chapter 6, illuminating the imaging area from different locations using multiple transmitters enhances the image contrast and reduces the background noise. However, the method requires separate measurements for each transmitter (at each time, only one transmitter should be active). Separate measurement of scattered fields for each transmitter location increases the required time for data collection. To measure the scattered fields due to each transmitter location while all transmitters are operating simultaneously, a technique similar to OFDM can be utilized assuming stepped frequency continuous wave (SFCW)

architecture for the radar system and by employing multiple transmitters with small constant frequency difference at each frequency step.

8.2. Imaging System Employing Multiple Transmitters

Figure 8.1 shows the block diagram of the imaging radar with N transmitters. In each transmitter, a DDS generates a stepped frequency signal in the range 150–450 MHz with 5 MHz steps resulting in aliasing-free range of 30 m in free space. At each frequency step, the frequencies of transmitters output signal are separated by Δf. At mth frequency step, the output frequency of the nth transmitter is $f_m + (n-1)\Delta f$ ($n = 1, 2, 3, \ldots, N$). At receiver, signals from the transmitters are down-converted by an LO signal with frequency of $f_m - \Delta f$ at mth frequency step, resulting IF signals with frequency of Δf, $2\Delta f$, $3\Delta f$, …, and $N\Delta f$. These signals are sampled by an analog to digital converter (A/D) with sampling rate of $2(2N\Delta f)$. Applying fast Fourier transform (FFT) with $2(2N)$ points to $2(2N)$ samples results in extraction of the phase and amplitude of the receive signal due to each transmitter as illustrated in Figure 8.1. The resulting $(n+1)$th FFT sample provides the phase and amplitude of the received signal due to nth transmitter.

According to Figure 8.1 down-conversion is performed in two steps in analog domain (down-conversion of the received signal by $f_m - 1$ MHz) and digital domain (down-conversion by 1 MHz $-\Delta f$ = 0.99 MHz) to avoid degradation of signals due to flicker noise in analog domain.

To synchronize the bi-static transmitters and receiver, reference clock signal for DDS and command for start of frequency sweep are transmitted to transmitters and receivers. Delay between start of frequency sweep at transmitters and receiver and delay in start of A/D sampling are two sources of error in phase measurements. The former introduces a shift in range of detected targets and the latter introduces a constant phase shift in the measured phase of the scattered signals at

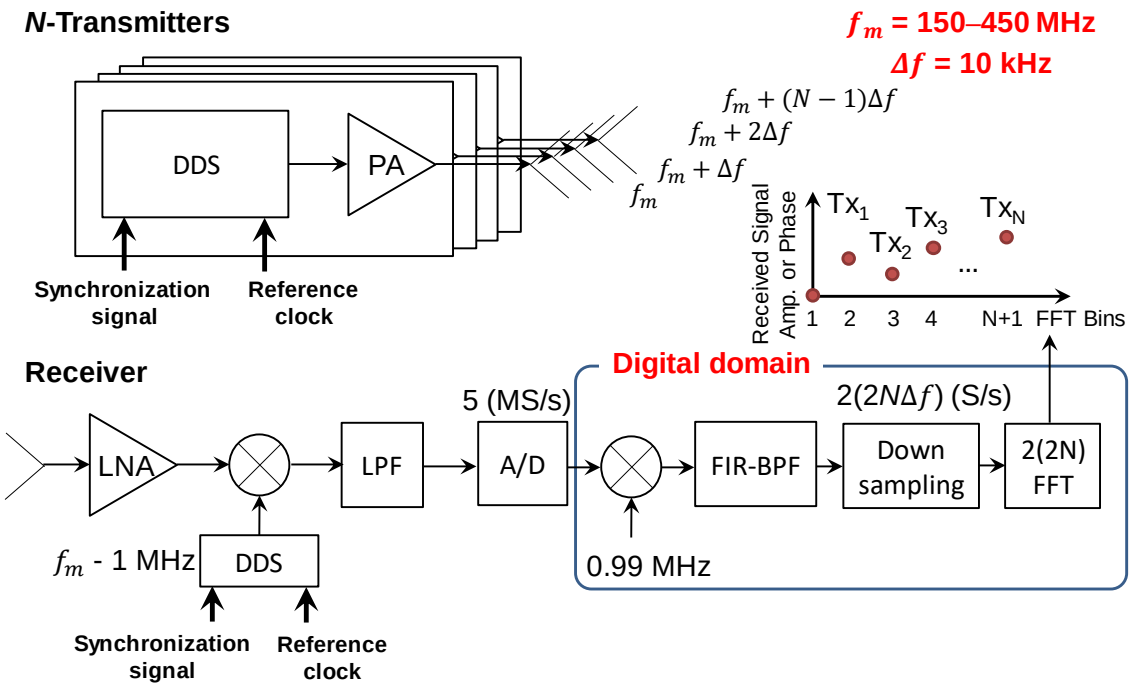

Figure 8.1. Block diagram of the imaging system with N transmitters.

different frequencies. Using the direct signal from transmitter to receiver and knowing the distance between the transmitter and receiver, the shift in the range of targets can be detected and removed as discussed in the next section.

8.3. Received Signal Model

For system realization, the stepped frequency signal is generated by a DDS that generates a chirp signal with large time steps (i.e. at each frequency step, frequency of the generated chirp signal remains constant for a large period of time). In this case, the phase shift due to A/D start time error remains constant for all frequency samples. This makes the error correction possible.

At a receiver, the received signal at mth frequency sample in a system employing N transmitters is modeled by

$$S_{r,m} = \sum_{n=1}^{N} A_m^n e^{j\phi_m^n} e^{j2\pi(f_m+(n-1)\Delta f)(t-t_{d,n})} \tag{8.1}$$

where A_m^n and ϕ_m^n are the amplitude and phase of the received scattered signal due to the nth transmitter and $t_{d,n}$ is the time delay in start of the chirp signal at the nth transmitter. After two steps of down-conversion (equivalent to down-conversion by $f_m - \Delta f$) and low pass filtering, the IF signal is

$$S_{IF} = \sum_{n=1}^{N} A_m^n e^{j\phi_m^n} e^{j2\pi n\Delta f t} \times e^{-j2\pi(f_m+(n-1)\Delta f)t_{d,n}} \times e^{j2\pi(f_m-\Delta f)t_{d,LO}}. \tag{8.2}$$

In (8.2), $t_{d,LO}$ is the delay in start of the frequency sweep at the receiver. Assuming an A/D with sampling rate of F_s (samples/s) starts sampling of the IF signal t_{AD} seconds after start of frequency sweep at the receiver, samples of the IF signal is

$$S_{IF}(k) = S_{IF}(t)|_{t=\frac{k}{F_s}+t_{d,LO}+t_{AD}}$$

$$= \sum_{n=1}^{N} A_m^n e^{j\phi_m^n} e^{j2\pi n\Delta f\left(\frac{k}{F_s}+t_{d,LO}+t_{AD}\right)} \times e^{-j2\pi(f_m+(n-1)\Delta f)t_{d,n}} \times e^{j2\pi(f_m-\Delta f)t_{d,LO}}. \tag{8.3}$$

The extracted signal at nth OFDM channel (= S_m^n = signal due to nth transmitter at mth frequency sample) is

$$S_m^n = \left(A_m^n e^{j\phi_m^n}\right)\left(e^{-j2\pi\Delta f\left((n-1)t_{d,n}-(n-1)t_{d,LO}-nt_{AD}\right)}\right)\left(e^{-j2\pi f_m\left(t_{d,n}-t_{d,LO}\right)}\right) \tag{8.4}$$

The first term is actual response. The second term is a constant phase shift that does not affect the image due to each pair of transmitter and receiver but prevents coherent addition of images for all pairs of transmitter and receiver in SAR imaging. The phase shift in the third term is linearly increased with frequency and is equivalent to a shift in the range of target (r_{shift})

$$e^{-j2\pi f_m\left(t_{d,n}-t_{d,LO}\right)} = e^{-j2\pi f_m(2r_{shift})/c_0} \tag{8.5a}$$

$$r_{shift} = \frac{(t_{d,n} - t_{d,LO})c_0}{2}. \quad (8.5b)$$

For correction of the shift in the range in the image formed for nth pair of transmitter and sampling point, first, the image is calculated using back-projection and S_{mn}s (m = 1, 2, …, M, where M is the number of frequency steps). In the image, the first peak is the signal received from the transmitter. The difference between the actual range to the transmitter and the detected one in the image is r_{shift}. After determining r_{shift}, to remove the shift in the signal received from the nth transmitter,

$$S_m^{n,shifted} = S_m^n . e^{j2\pi(f_m)\frac{2r_{shift}}{c_0}} = \left(A_m^n e^{j\phi_m^n}\right)\left(e^{-j2\pi\Delta f\left((n-1)t_{d,n}-(n-1)t_{d,LO}-nt_{AD}\right)}\right) \quad (8.6)$$

must be calculated for m = 1, 2, …, M.

To determine and remove the second term in (8.6), the image is formed at the location of transmitter using back-projection and $S_m^{n,shifted}$s. The remaining phase in the image of the transmitter is an estimation of the second term in (8.6). Denoting the remaining phase by φ_n, the corrected S_m^n is calculated by

$$S_m^{n,corrected} = S_m^{n,shifted} e^{-j\varphi_n} \quad (8.7)$$

$S_m^{n,corrected}$s are used for image formation.

For SAR image formation, $S_m^{n,corrected}$ is calculated for all the receivers (sampling points) and using back-projection method described in Chapter 6 the final SAR image is calculated (it is noted that in this Chapter, n indicates the transmitter while in Chapter 6, n indicates receiver location or sampling point).

The flow chart for error correction and image formation is shown in Figure 8.2.

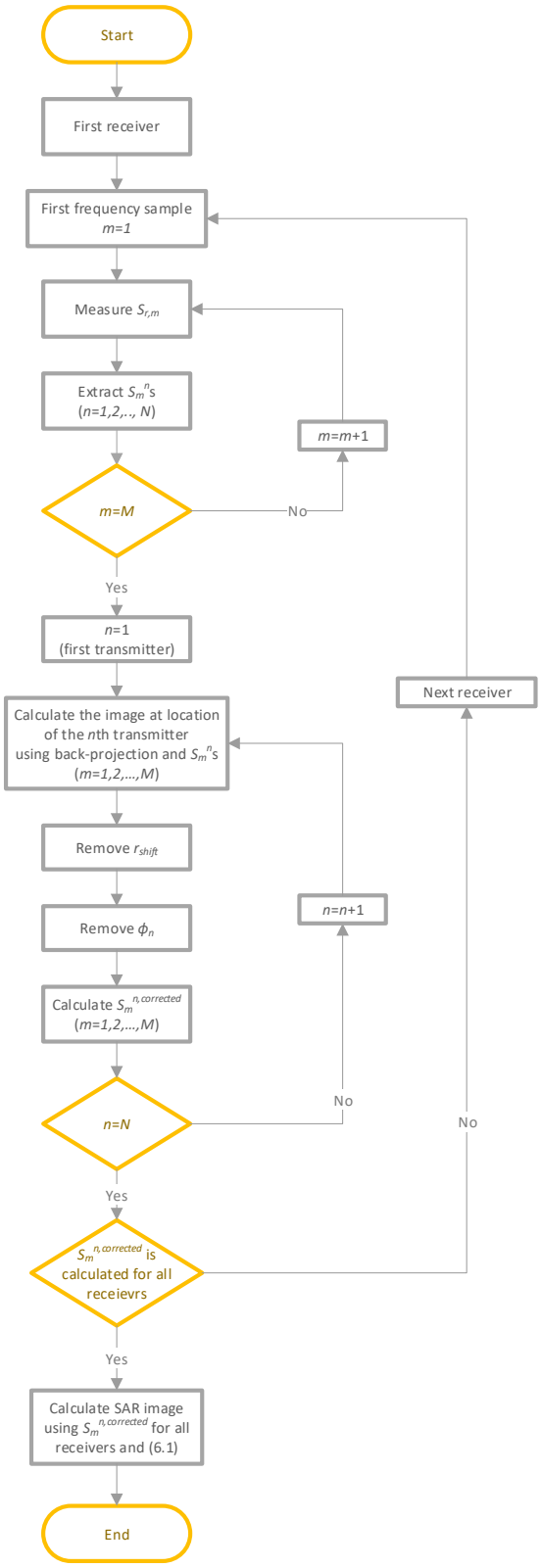

Figure 8.2. Flow chart of the error correction and image formation using an imaging system with N transmitters and M frequency steps.

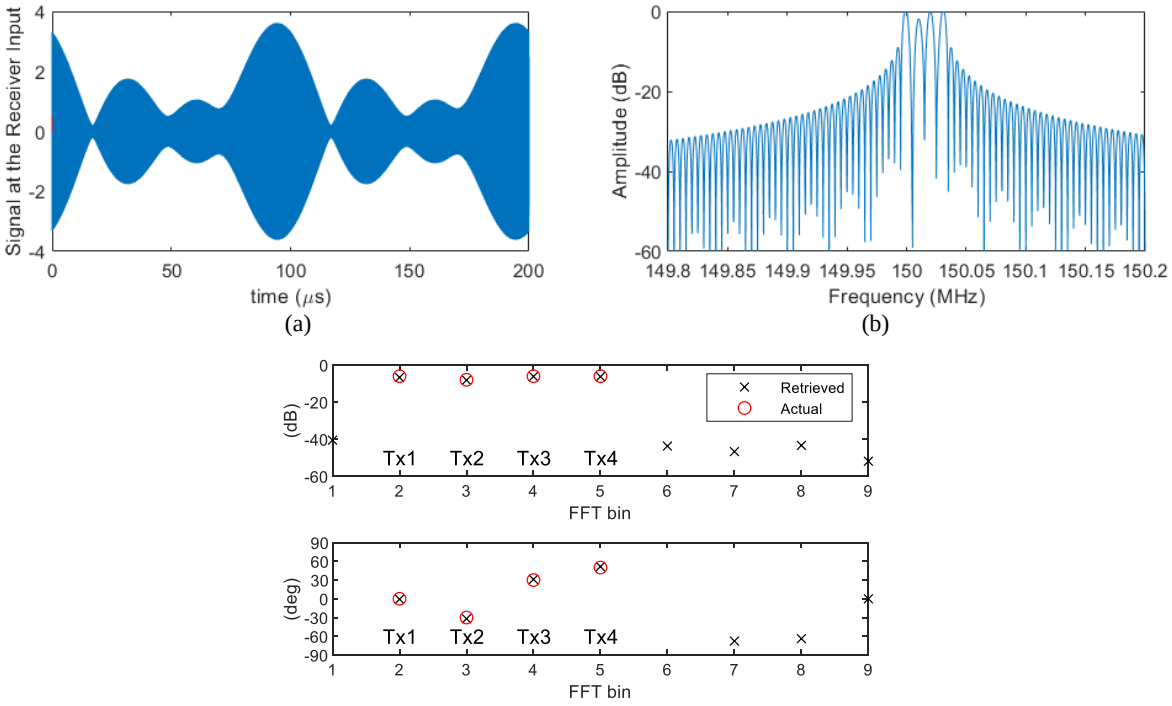

Figure 8.3. A sample of signal at the receiver input (no noise) in a system with 4 transmitters. (a) Signal in time domain. (b) Signal in frequency domain. (c) Actual and retrieved phases and amplitudes of signals due to each transmitter.

8.4. Evaluation of the System Performance

To evaluate the performance of signal phase and amplitude detection while all transmitters are operating simultaneously, four transmitters operating at the first frequency step (f_m = 150 MHz) are considered. Figure 8.3(a) and Figure 8.3(b) show a sample of received signal at the receiver input in time domain and frequency domain, respectively, while the transmitters' frequencies are separated by 10 kHz (= Δf) and actual phases and amplitudes of the signals due to each transmitter are the values shown in Fig. 8.3(c) (indicated by circles). The detected phases and amplitudes are also shown in Fig. 8.3(c). The results show accurate detection of amplitudes and phases of the signals when noise is not present.

To evaluate the performance of the system in presence of noise. The same signal as Figure 8.3 but with SNR of 3 dB is assumed to be present at the input of the receiver (noise power is

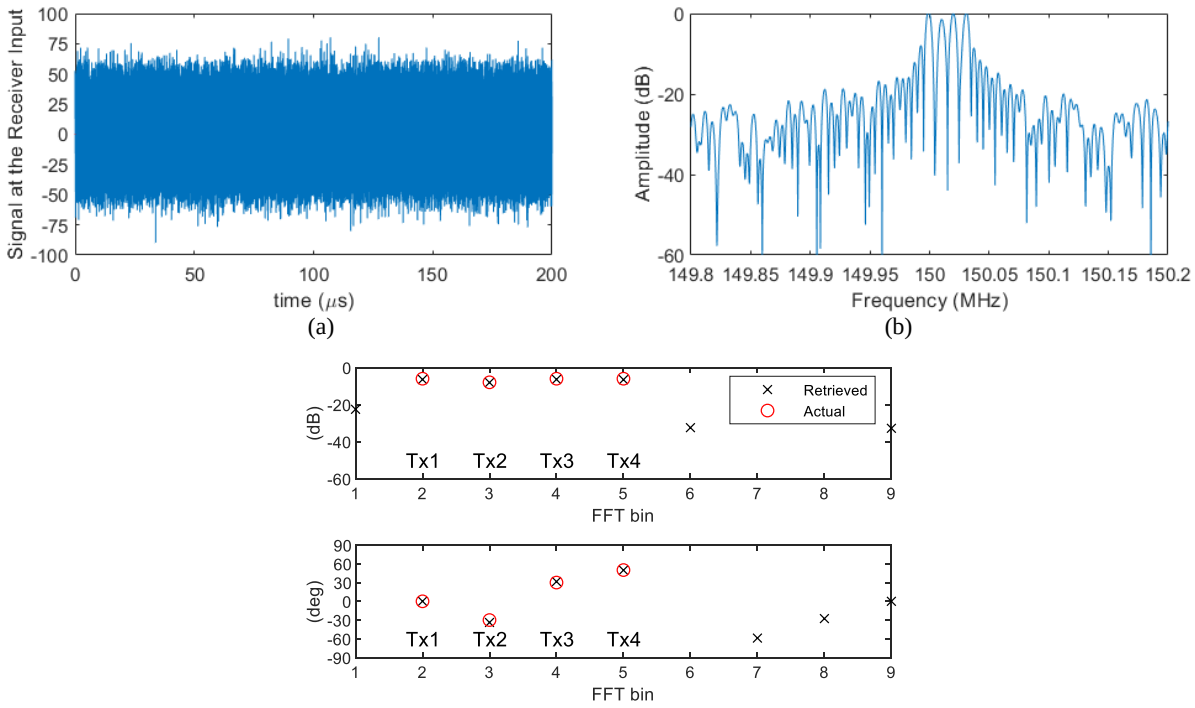

Figure 8.4. A sample of signal at the receiver input (SNR = 3 dB, noise power is measured in the range 149−154 MHz) in a system with 4 transmitters. (a) Signal in time domain. (b) Signal in frequency domain. (c) Actual and retrieved phases and amplitudes of signals due to each transmitter.

measured in the range 149−154 MHz). The signal in time domain and frequency domain is shown in Figure 8.4(a) and Figure 8.4(b), respectively. Detected phase and amplitude for signals from different transmitters are shown in Figure 8.4(c). The results show maximum error of 1 dB in the detected amplitude and maximum error of 5° in the detected phase.

8.5. Conclusion

A radar system has been introduced in this chapter that realizes high resolution subsurface imaging using distributed robotic sensors. As required by the imaging method, the system is able to accommodate multiple transmitters while the data collection time is not affected. Using a technique similar to OFDM and SFCW architecture for the radar system, the signal due to each transmitter is separated while all transmitters are operating simultaneously. Random delay in start

of signal generation at transmitters and receiver and start of sampling in A/D are two sources of error in phase measurements. It has been shown that by forming the image at location of the transmitter using direct coupling between transmitter and receiver, the errors can be corrected for coherent processing of all data. Numerical simulations of the designed system show that the system can accurately separate response of different transmitters even in presence of noise.

Chapter 9 Conclusion and Recommendations for Future Work

9.1. Research Summary

The main objective of this research is devising new techniques to address low mobility, low cross-range resolution, limited field of view, and time-consuming data collection process in currently available through-the wall and subsurface imaging systems that utilize EM waves to detect visually obscured objects and map buildings' interiors and subsurface features.

In conventional through-the-wall imaging systems, high cross-range resolution is achieved by utilizing large antenna arrays or large 1-D synthetic arrays formed by directive antennas. Large antenna arrays limit the mobility and directive antennas limit the field of view of the system. In the proposed new imaging technique for through-the-wall imaging, directive antennas are replaced by omnidirectional antennas and a large 2-D synthetic array is formed by limited number of moving bi-static transmitters and receivers that provides high cross-range resolution images with 360° field of view. In the presented technique increasing the cross-range resolution does not affect the system mobility.

Currently available GPR systems for subsurface imaging are usually low cross-range resolution imaging systems that employ monostatic transceivers with small aperture size antennas. To achieve high cross-range resolution, large antenna arrays with narrow beam are utilized. The low frequency of operation for efficient penetration of EM waves into the ground requires large physical size for the antenna arrays and as a result, high resolution systems are usually mounted

on vehicles and have limited mobility. In the new subsurface imaging technique presented in this research, a large 2-D array is synthesized by coherent processing of scattered fields sampled at different locations using small number of moving bi-static transmitters and receivers. The formed synthesized array provides 3-D images of subsurface. In the new technique, the large antenna arrays for obtaining high cross-range resolution are eliminated and enhancing the cross-range resolution does not affect mobility of the system. The large field of view enabled by the new technique significantly reduces the time required for data collection.

9.2. Contributions

In the following subsections, the contributions made in this research are detailed.

9.2.1. Development of All-Directions Through-the-Wall Imaging Method

All-directions through-the-wall imaging is a new through-the-wall imaging technique that utilizes small number of bi-static omnidirectional transmitters and receivers with high mobility to collect scattered fields at different locations within the imaging area. The acquired samples are coherently processed using back-projection and a beam-forming technique to form a large 2-D synthetic aperture and create high cross-range resolution images with 360° field of view.

Using omnidirectional antennas, the scattered fields are sampled on circles with the center at the transmitter location to eliminate the ambiguity in detection of objects locations.

Direct coupling from transmitter and multiple interactions of transmitted waves with walls are received at the receiver resulting saturation of the receiver and appearance of spurious images. To reduces the effect of these undesired signals at the receiver, omnidirectional antennas with orthogonal circular polarizations are used for transmitter and receiver. In this case, direct coupling

from transmitter to receiver and signals experiencing double reflections are further attenuated by polarization isolation of the antennas.

Proper synchronization between bi-static transmitter and receivers is another challenge that has been addressed by using FMCW architecture for the imaging system.

9.2.2. Design of a New Wideband Omnidirectional Circularly Polarized Antenna for All-Directions Through-the-Wall Imaging

A novel wideband omnidirectional circularly polarized antenna has been designed, fabricated, and tested for all-directions through-the-wall imaging application. In the proposed antenna structure, for the first time, field distribution similar to circular waveguide TE_{21} mode is excited using wideband SLA elements to generate a linearly polarized wave at the far-field of the antenna whose polarization tilt angle rotates in azimuth direction. It is shown that excitation of the second circular TE_{21} mode with the same amplitude and 90° phase difference and spatial rotation of 45° results in circular polarization radiation.

The two circular TE_{21} modes are generated using 16 monopole SLA elements. The required excitation phases and amplitudes are generated by a feed network on the backside of the antenna ground plane including wideband low-pass/high-pass phase shifters and Wilkinson power dividers.

Measurement results of the antenna show 64% (1.11−2.17 GHz) of 3-dB AR bandwidth and 58% (1.11−2.02 GHz) of operation bandwidth (3-dB AR and 10-dB impedance bandwidth). The achieved AR and operation bandwidth are the highest among the proposed structures for wideband omnidirectional circularly polarized antennas.

Besides eliminating the undesired signals at the receiver, the circularly polarized omnidirectional antennas enable imaging of objects with large aspect ratio and arbitrary orientation.

9.2.3. Development of an Image Formation Technique for All-Directions Through-the-Wall Imaging Using Bi-Static FMCW Transceivers

To simplify synchronization of bi-static transmitters and receivers, FMCW architecture is used for the imaging system. In this case, start of chirp signals at transmitter and receivers must be synchronized. The synchronization error and random and deterministic delays in circuits prevent coherent processing of all sampling points which is required by all-directions through-the-wall imaging method. In this research, the system has been accurately modeled considering synchronization errors and delays in circuits and a method utilizing direct coupling from transmitter to receiver has been proposed to compensate the errors and delays. In addition, an image formation technique compatible with FMCW signals has been developed.

A bi-static FMCW transmitter and receiver have been designed and fabricated. Using the fabricated radar system and circularly polarized omnidirectional antennas, all-directions through-the-wall imaging has been tested in real scenarios. The results indicate the capability of the method in providing high resolution images with 360° field of view using small number of collected samples.

9.2.4. Development of a Method for Background Noise Reduction and Range-Resolution Enhancement in Through-the-Wall Imaging

In through-the-wall imaging, multipath and unsuppressed sidelobes of the point spread

function of the imaging algorithm produce background noise is the image. A novel method has been proposed to reduce the background noise. The method utilizes GPOF method to detect locations of reflections. Forming the image (using back-projection) at only the detected points results images with significantly reduced backgrounds noise.

It is shown that the method also improves the range resolution even in presence of noise.

9.2.5. Development of a Method for Detection of Walls in High-Resolution Through-the-Wall SAR Imaging

It has been shown that the walls and large flat surfaces that do not exhibit single phase center are imaged as discrete points when a large aperture is entirely used for image formation. A simple method applicable to both monostatic and multi-static SAR imaging has been developed to discriminate walls and large flat surfaces from limited size objects. The method also detects the location and orientation of walls surfaces in the imaging area. It has been shown that the signals reflected from a wall boundary are approximately equivalent to the signals that are received from a limited size fictitious object located behind the wall and at the location of the transmitter mirrored with respect to the wall. Assuming that a wall surface is present in the imaging area, the image can be calculated at the location of these fictitious objects. A large intensity for the obtained image indicates that the assumed wall surface is real.

The performance of the method has been evaluated through applying it to the measured data.

9.2.6. Development of a New High Resolution Subsurface Imaging Method Using Small Number of Robotic Transmitters and Receivers

Based on the presented method for through-the-all imaging, a new method for high-resolution subsurface imaging has been proposed. The method enables 3-D imaging of subsurface with high cross-range resolution in a short period of time while maintains high mobility for the imaging system. It utilizes bi-static transmitters and receivers to sample the scattered and reflected signals from buried targets and subsurface discontinuities at different location. By coherent processing of the sampled signals, it creates a large 2-D synthetic array that provides high resolution 3-D images. High resolution 3-D images make it simple to interpret the image and detect and classify buried targets and underground features. Performance of the imaging method has been evaluated through a field measurement.

To reduce spurious images and enhance image contrast, the method utilizes multiple transmitters to illuminate the subsurface from different locations. A technique similar to OFDM is utilized to separate signal due to each transmitter while all transmitters are operating simultaneously. A system realizing the imaging method has been designed and its performance has been evaluated through simulations in presence of noise.

9.2.7. Design of a Low Frequency, Low Profile, Wideband Antenna for High Resolution Imaging of Deeply Buried Targets or Targets Buried in Soil with High Losses

A wideband antenna operating in the range 140−510 MHz has been designed, fabricated and tested. The low frequency of operation of the antenna enables imaging of deeply buried targets or targets buried in dense and wet soil with high losses. The antenna is low profile with total height

(excluding connectors) of 153 mm (= $0.072\lambda_0$ where λ_0 is the free space wavelength at 140 MHz). Low profile antennas enable higher mobility for GPR systems.

The antenna structure is based on the low profile wideband ENVELOP antenna. However, in this work, to improve the operation bandwidth of the antenna for a given constant height, an exponential profile is used instead of a linear profile for the ENVELOP element. To obtain a main beam normal to the ground surface as required by subsurface imaging applications, an array of two ENVELOP antennas with differential feeding is used. The magnetic coupling between the antennas reduces the lower frequency of the operation and improves the operation bandwidth.

Applicability of the antenna in GPR imaging has been tested through a field measurement on wet and dense soil with high losses.

9.3. Future Work

The future work based on the research presented in this dissertation is outlined in the following subsections.

9.3.1. Applying the Method Presented for Detection of Reflecting Points in Through-the-Wall Imaging to Subsurface Imaging

In Chapter 5, a method based on GPOF method has been introduced for detection of reflecting points in through-the-wall imaging scenarios. It has been shown that forming the image at the detected points enhances range resolution (even in the case of low SNRs) and reduces the background noise. In subsurface imaging application where signal bandwidth is narrower (comparing to through-the wall imaging), a range resolution enhancement method can significantly improve detection of closely spaced buried targets and subsurface features without

adding to the system complexity. A specific application of the method is in detection of shallowly buried land mines where resolving the image due to the air-ground interface and the land mines is challenging due to limited range resolution.

9.3.2. Design of a Wideband Circularly Polarized Antenna for Subsurface Imaging Applications

As shown in Chapter 4, using circular polarization in through-the-wall imaging enables imaging of objects with large aspect ratio and arbitrary orientation. In conventional GPR imaging, using circularly polarized antennas enables reliable detection and imaging of buried targets with large aspect ratio such as low diameter pipelines and cables.

One possible design is using 4 monopole SLA elements (with structure similar to the one presented in Chapter 3) mounted on a circular ground plane as shown in Figure 9.1. For obtaining circular polarization, all SLAs are coaxially fed by the same amplitude and absolute phase progression of 90° between each two adjacent elements as shown in Figure 9.1(a). This creates two orthogonal linearly polarized electric fields on the top of SLAs with 90° phase difference (indicated by green arrows in Figure 9.1(a)) resulting circularly polarized radiation. The handedness of the circular polarization is determined by the sign of the phase progression. In addition, the excitations shown in Figure 9.1(b) provide linear polarizations. It suggests that by utilizing RF switches and phase shifters in the feed network of the antenna, the polarization can be switched between linear and left-handed and right-handed circular.

As an example, an antenna with ground plane diameter of 200 mm and SLA element height of 40 mm has been simulated. The antenna is shown in Figure 9.1. The resulting Reflection coefficient (defined by (3.11)) is shown in Figure 9.2, which indicates 10-dB impedance band in

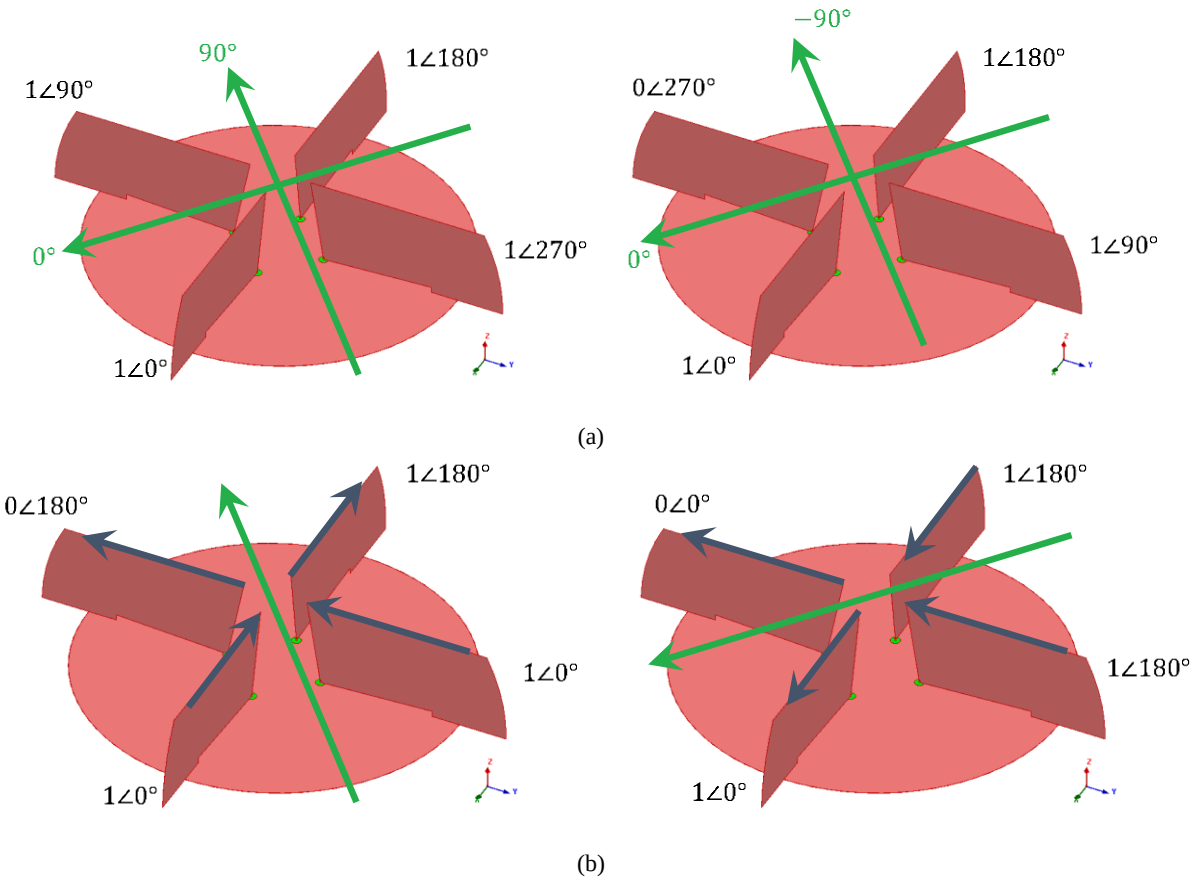

Figure 9.1. Wideband polarization-reconfigurable antenna with directive radiation pattern. (a) Excitation for CP operation. (b) Excitation for LP operation (green arrows show the generated linear polarized electric fields and blue arrows show the excited currents).

the range 1.05–2.2 GHz. The obtained LP and CP gain and orthogonal polarization (cross polarization) gain are shown in Figure 9.3.

Figure 9.4 shows the gain radiation pattern at 1.6 GHz for LP and CP excitation. The results show directive radiation pattern with high polarization isolation.

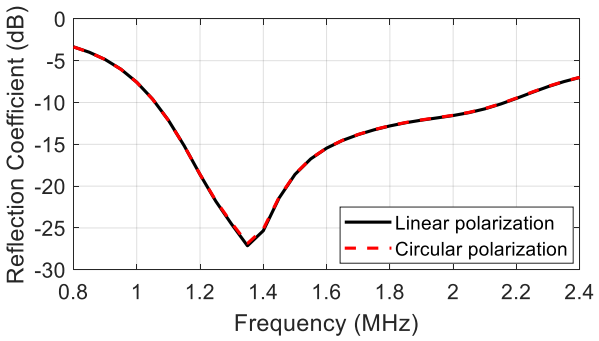

Figure 9.2. Reflection coefficient of the antenna in Figure 9.1 for CP and LP operation.

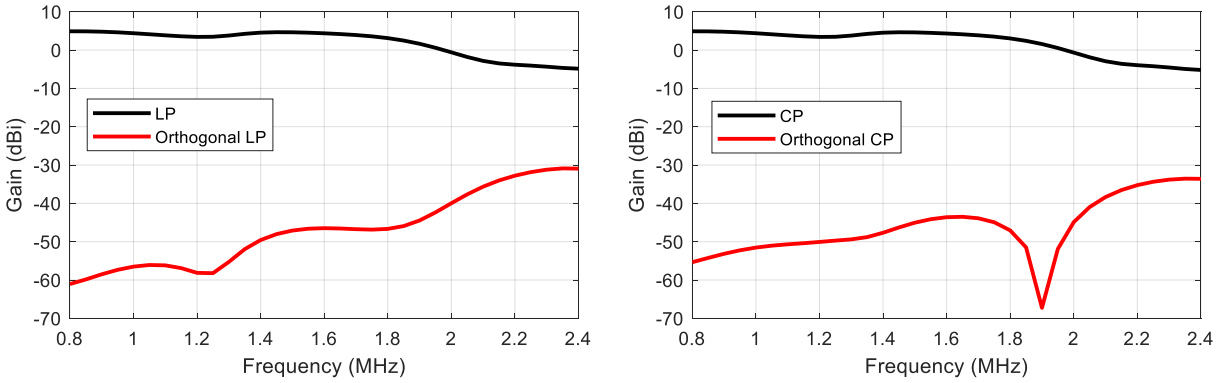

(a) (b)

Figure 9.3. Simulated gain for LP operation (a) and CP operation (b) (black line is the gain for the excited polarization and the red line is the gain for cross-polarization)

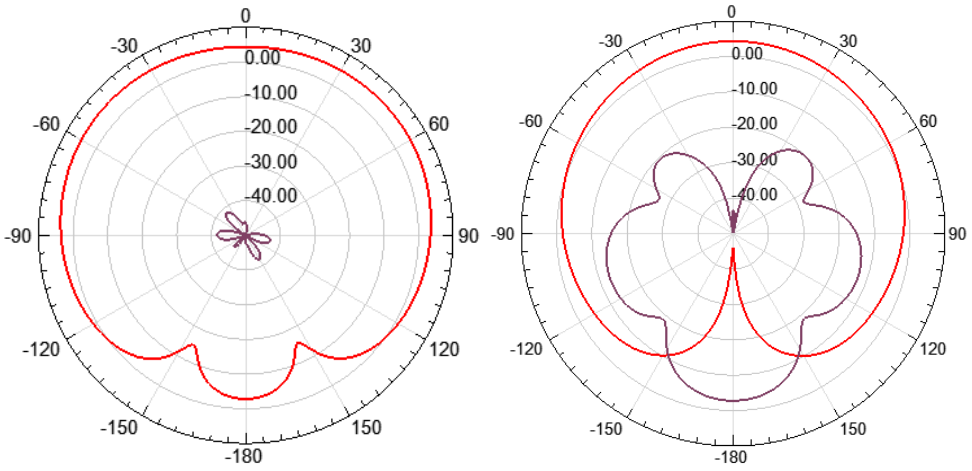

(a) (b)

Figure 9.4. Co- (red line) and cross-polarization (black line) gain radiation pattern (in dBi) at 1.6 GHz for the antenna in Figure 9.1 for CP operation (a) and LP operation (b).

9.3.3. Fabrication of the Radar System with Multiple Transmitters and Evaluation of Performance of the Proposed Subsurface Imaging Method in Presence of Different Objects with Different Shapes and Orientations

As a future work, the radar system with the block diagram shown in Figure 8.1 can be fabricated. With the fabricated radar, performance of the proposed subsurface imaging method can be evaluated in presence of targets with different shapes buried at different depth in different soil types.

Appendices

Appendix A: MATLAB Code for All-Directions Through-the-Wall Imaging Using Bi-Static FMCW Transceivers

In this appendix, MATLAB codes implementing the error correction and imaging method introduced in Chapter 4 are presented.

The following code gets the measurement data as an input and calculates the parameters t_s (`ts`), $R_c - R_o$ (`Ro_Rc`), d (`d`), and R_a (`Ra`) for all transmitter and receiver pairs and saves them in `ts_d_Ro_Rc_Ra.mat`.

The measurement data (`measurement_data.mat`) includes the following vectors/matrices

1. `xs`: an $N \times 1$ vector defining the x position of N sampling points;
2. `ys`: an $N \times 1$ vector defining the y position of N sampling points;
3. `Tx`: a 1×2 vector defining the x position (first element) and y position (second element) of the transmitter;
4. `Fs`: A/D sampling rate in Samples/s;
5. `data`: Assuming N sampling points are used for image formation and M samples of IF signal are collected for each sampling point, `data` is an $M \times N$ matrix in which nth column contains M samples of IF signal for nth pair of sampling point and transmitter.

The parameters `f0` and `gamma` define start frequency and chirp rate of the system, respectively.

```
clc
clear all
close all

f0=1.2e9; %start frequency
c=3e8;
gamma=120e3/8e-9; %chirp rate Hz/s

load('measurement_data.mat')

ts=zeros(size(xs));
d=zeros(size(xs));
Rc_Ro=zeros(size(xs));
Ra=zeros(size(xs));

for n=1:1:length(xs)

    s=data(:,n);

    NFFT=2*2^nextpow2(length(s));
    fs=Fs/2*linspace(0,1,NFFT/2+1); %frequency samples
    df=fs(2)-fs(1);
    temp=fft(s,NFFT)/length(s);
    S=2*temp(1:NFFT/2+1);

    [~,index]=max(20*log10(abs(S)));
    f_direct=fs(index);
    d(n)=sqrt((xs(n)-Tx(1))^2+(ys(n)-Tx(2))^2);

    Rc_Ro(n)=f_direct*c/(2*gamma)-(d(n)/2); %Rc-Ro
    Ra(n)=d(n)/2;

    t=((1/Fs)*(0:1:(length(s)-1))).';
    phase_Sa0=(4*pi*f0/c)*(Ra(n)+Rc_Ro(n)) + (4*pi*gamma/c)*t*(Ra(n)+...
        Rc_Ro(n)) - (4*pi*gamma/(c^2))*((Ra(n)+Rc_Ro(n))^2);

    sc=s.*exp(-j*phase_Sa0);
    temp=fft(sc,NFFT)/length(s);
    Sc=2*temp(1:NFFT/2+1);

    phi0=angle(Sc(1));
    ts(n)=phi0*c/(4*pi*gamma*(Ra(n)+Rc_Ro(n)));

end

save('ts_d_Ro_Rc_Ra.mat','ts','d','Rc_Ro','Ra')
```

The following code gets `measurement_data.mat` and `ts_d_Ro_Rc_Ra.mat` as inputs and calculates the corrected IF signals `sc` using (4.15) and image `Simage` using (4.18) at points defined by `X` and `Y`.

```
clc
clear all
close all

f0=1.2e9;
c=3e8;
gamma=120e3/8e-9;

load('measurement_data.mat')
load('ts_d_Ro_Rc_Ra.mat')

[X,Y]=meshgrid(-3.6:0.05:3.6,-3.6:0.05:3.6);
Simage=ones(size(X))*0.00001;

for n=1:1:length(xs)

    s=data(:,n);

    t=((1/Fs)*(0:1:(length(s)-1))).';
    phase_Sa=(4*pi*f0/c)*(Ra(n)+Rc_Ro(n)) +...
        (4*pi*gamma/c)*(t+ts(n))*(Ra(n)+Rc_Ro(n)) -...
        (4*pi*gamma/(c^2))*((Ra(n)+Rc_Ro(n))^2);

    sc=s.*exp(-j*phase_Sa); %corrected IF signals

    NFFT=2*2^nextpow2(length(s));
    fs=Fs/2*linspace(0,1,NFFT/2+1); %frequency samples
    temp=fft(sc,NFFT)/length(s);
    Sc=2*temp(1:NFFT/2+1);

    Rt=(sqrt((X-Tx(1)).^2+(Y-Tx(2)).^2) +...
        sqrt((X-xs(n)).^2+(Y-ys(n)).^2))/2;
    phasecoeff=exp(-j*4*pi*((Rt-Ra(n))/c)*...
        (f0 - (2*gamma*(Ra(n)+Rc_Ro(n))/c) + gamma*ts(n)));
    for nn=1:1:numel(X)
        if(sqrt((X(nn))^2+(Y(nn)^2))>0.5)
            [~,index0]=min(abs(fs-2*(Rt(nn)-Ra(n))*gamma/c));
            Simage(nn)=Simage(nn)+phasecoeff(nn)*Sc(index0);
        end
    end

end

%normalizing the image and converting to dB
temp=20*log10(abs(Simage)/max(max(abs(Simage))));

%displaying the values larger than -10 dB.
temp=temp.*(temp>=-10)+(-10)*(temp<-10);

figure(5)
surf(X,Y,temp)
shading interp
axis equal
view(0,90)
```

```
xlabel('x (m)')
ylabel('y (m)')
colormap(jet(1024))
colorbar('Location','EastOutside')
xlim([-3.6 3.6])
ylim([-3.6 3.6])
set(gca,'XTick', -3.6:1.8:3.6)
set(gca,'YTick', -3.6:1.8:3.6)
hold on
plot(xs, ys, '.w')
```

It is noted that in both codes the number of FFT points (`NFFT`) must be the same.

Appendix B: MATLAB Code for Detection of Walls and Large Flat Surfaces in Through-the-Wall Imaging Using Bi-Static FMCW Transceivers

The code presented in this appendix implements the wall detection method described in Chapter 5 for through-the-wall imaging using bi-static FMCW transceivers. The code gets `measurement_data.mat` and `ts_d_Ro_Rc_Ra.mat` (described in Appendix A) as inputs. The polar coordinate for detection of points A on the walls are defined by `R` and `theta`. For each point in the defined polar coordinate, the code first calculates the vectors $\hat{n}$ (`nhat`), $\bar{t}_n$ (`tn`), $\bar{r}_n$ (`rn`), and $\bar{t}'_n$ (`tpn`) and the parameter d_n (`dn`) (all are defined in Figure 5.8) and then it calculates $I(R,\theta)$ (`Simage`) as described in Section 5.3.2.

```
clc
clear all
close all

f0=1.2e9;
c=3e8;
gamma=120e3/8e-9;

load('measurement_data.mat')
load('ts_d_Ro_Rc_Ra.mat')

[R, theta]=meshgrid(1.6:0.05:3.6, (0:1:360)*pi/180);
X=R.*cos(theta);
Y=R.*sin(theta);
Simage=zeros(size(R));

for nn=1:1:numel(R)

    %A=[R(nn)*cos(phi(nn)), R(nn)*sin(phi(nn))]; %A points
    nhat=[-cos(theta(nn)), -sin(theta(nn))];

    for n=1:1:length(xs)
        tn=[Tx(1)-R(nn)*cos(theta(nn)), Tx(2)-R(nn)*sin(theta(nn))];
```

```
        rn=[xs(n)-R(nn)*cos(theta(nn)), ys(n)-R(nn)*sin(theta(nn))];
        tpn=tn-2*sum(nhat.*tn)*nhat;
        dn=sqrt((rn(1)-tpn(1))^2+(rn(2)-tpn(2))^2);

        s=data(:,n);

        t=((1/Fs)*(0:1:(length(s)-1))).';
        phase_Sa=(4*pi*f0/c)*(Ra(n)+Rc_Ro(n)) +...
            (4*pi*gamma/c)*(t+ts(n))*(Ra(n)+Rc_Ro(n)) -...
            (4*pi*gamma/(c^2))*((Ra(n)+Rc_Ro(n))^2);

        sc=s.*exp(-j*phase_Sa); %corrected s

        NFFT=2*2^nextpow2(length(s));
        fs=Fs/2*linspace(0,1,NFFT/2+1); %frequency samples
        temp=fft(sc,NFFT)/length(s);
        Sc=2*temp(1:NFFT/2+1);

        Rt=dn/2;
        phasecoeff=exp(-j*4*pi*((Rt-Ra(n))/c)*...
        (f0 - (2*gamma*(Ra(n)+Rc_Ro(n))/c) + gamma*ts(n)));
        [~,index0]=min(abs(fs-2*(Rt-Ra(n))*gamma/c));
        Simage(nn)=Simage(nn)+phasecoeff*Sc(index0);
    end
end

%normalizing the image and converting to dB
temp=20*log10(abs(Simage)/max(max(abs(Simage))));

%displaying the values larger than -10 dB.
temp=temp.*(temp>=-10)+(-10)*(temp<-10);

figure(5)
surf(X,Y,temp)
shading interp
axis equal
view(0,90)
xlabel('x (m)')
ylabel('y (m)')
colormap(gray(1024))
colorbar('Location','EastOutside')
xlim([-3.6 3.6])
ylim([-3.6 3.6])
set(gca,'XTick', -3.6:1.8:3.6)
set(gca,'YTick', -3.6:1.8:3.6)
grid off
box on
```

It is noted that in the code presented in this appendix, the number of FFT points (`NFFT`) must be the same as the number of FFT points in the first code presented in Appendix A.

Bibliography

[1] H. M. Jol, *Ground Penetrating Radar: Theory and Applications*, Amsterdam, Netherlands: Elsevier Science, 2009.

[2] A. P. Annan, "GPR-history, trends, and future developments," *Subsurface Sens. Technol. Appl.*, vol. 3, no. 4, pp. 253–270, Oct. 2002.

[3] A. Benedetto, F. Tosti, L. B. Ciampoli, and F. D'Amico, "GPR applications across engineering and geosciences disciplines in Italy: a review", *IEEE J. Sel. Topics Appl. Earth Obs. Remote Sens.*, vol. 9, no. 7, pp. 2952–2965, Jul. 2016.

[4] F. T. Gizzi and G. Leucci, "Global research patterns on ground penetrating radar (GPR)," *Surveys Geophysics*, vol. 39, no. 6, pp. 1039–1068, Nov. 2018.

[5] E. J. Baranoski, "Through wall imaging: historical perspective and future directions," *IEEE International Conference on Acoustics, Speech and Signal Processing*, Las Vegas, NV, 2008, pp. 5173–5176.

[6] D. D. Ferris and N. C. Currie, "Survey of current technologies for through-the-wall surveillance (TWS)," *Proc. SPIE 3577, Sensors, C3I, Information, and Training Technologies for Law Enforcement*, Jan. 1999.

[7] D. D. Ferris and N. C. Currie, "Microwave and millimeter-wave systems for wall penetration," *Proc. SPIE 3375, Targets and Backgrounds: Characterization and Representation IV*, July 1998.

[8] E. F. Greneker, "RADAR flashlight for through-the-wall detection of humans," *Proc. SPIE 3375, Targets and Backgrounds: Characterization and Representation IV*, July 1998.

[9] M. G. Amin and F. Ahmad, "Wideband synthetic aperture beamforming for through-the-wall imaging," *IEEE Signal Process. Mag.*, vol. 25, no. 4, pp. 110–113, July 2008.

[10] F. Ahmad, Y. Zhang, and M. G. Amin, "Three-dimensional wideband beamforming for imaging through a single wall," *IEEE Geosci. Remote Sens. Lett.*, vol. 5, no. 2, pp. 176–179, Apr. 2008.

[11] J. Li, Z. Zeng, J. Sun, and F. Liu, "Through-wall detection of human being's movement by UWB radar," *IEEE Geosci. Remote Sens. Lett.*, vol. 9, no. 6, pp. 1079–1083, Nov. 2012.

[12] S. S. Ram and H. Ling, "Through-wall tracking of human movers using joint Doppler and array processing," *IEEE Geosci. Remote Sens. Lett.*, vol. 5, no. 3, pp. 537–541, July 2008.

[13] © 2016 IEEE. Reprinted with permission from B. Yektakhah and K. Sarabandi, "All-directions through-the-wall radar imaging using a small number of moving transceivers," *IEEE Trans. Geosci. Remote Sens.*, vol. 54, no. 11, pp. 6415–6428, Nov. 2016.

[14] © 2019 IEEE. Reprinted with permission from B. Yektakhah and K. Sarabandi, "All-directions through-the-wall imaging using a small number of moving omnidirectional bi-static FMCW transceivers," *IEEE Trans. Geosci. Remote Sens.*, vol. 57, no. 5, pp. 2618–2627, May 2019.

[15] H. Brunzell, "Detection of shallowly burried objects using impulse radar," *IEEE Trans. Geosci. Remote Sens.*, vol. 37, no. 2, pp. 875–886, Mar. 1999.

[16] © 2017 IEEE. Reprinted with permission from B. Yektakhah and K. Sarabandi, "A wideband circularly polarized omnidirectional antenna based on excitation of two orthogonal circular TE_{21} modes," *IEEE Trans. Antennas Propag.*, vol. 65, no. 8, pp. 3877–3888, Aug. 2017.

[17] © 2019 IEEE. Reprinted with permission from B. Yektakhah and K. Sarabandi, "A method for detection of flat walls in through-the-wall SAR imaging," *IEEE Geosci. Remote Sens. Lett.*, under review.

[18] © 2019 IEEE. Reprinted with permission from B. Yektakhah, J. Chiu, F. Alsallum, and K. Sarabandi, "Low profile, low frequency, UWB antenna for imaging of deeply buried targets," *IEEE Geosci. Remote Sens. Lett.*, 2019.

[19] F. Ahmad, Y. Zhang, and M. G. Amin, "Three-dimensional wideband beamforming for imaging through a single wall," *IEEE Geosci. Remote Sens. Lett.*, vol. 5, no. 2, pp. 176−179, April 2008.

[20] L.-P. Song, C. Yu, and Q. H. Liu, "Through-wall imaging (TWI) by radar: 2-D tomographic results and analyses," *IEEE Transactions on Geosci. Remote Sensing*, vol. 43, no. 12, pp. 2793−2798, Dec. 2005.

[21] F. Soldovieri, R. Solimene, A. Brancaccio, and R. Pierri, "Localization of the interfaces of a slab hidden behind a wall," *IEEE Transactions on Geosci. Remote Sensing*, vol. 45, no. 8, pp. 2471−2482, Aug. 2007.

[22] J.-T. Gonzalez-Partida, P. Almorox-Gonzalez, M. Burgos-García, B.-P. Dorta-Naranjo, and J. I. Alonso, "Through-the-wall surveillance with millimeter-wave LFMCW radars," *IEEE Transactions on Geosci. Remote Sensing*, vol. 47, no. 6, pp. 1796−1805, June 2009.

[23] H. Wang, R. M. Narayanan, and Z. O. Zhou, "Through-wall imaging of moving targets using UWB random noise radar," *IEEE Antennas Wireless Propag. Lett.*, vol. 8, pp. 802−805, 2009.

[24] J. Li, Z. Zeng, J. Sun, and F. Liu, "Through-wall detection of human being's movement by UWB radar," *IEEE Geosci. Remote Sens. Lett.*, vol. 9, no. 6, pp. 1079−1083, Nov. 2012.

[25] W. Zhang and A. Hoorfar, "Three-dimensional synthetic aperture radar imaging through multilayered walls," *IEEE Trans. Antennas Propag.*, vol. 62, no. 1, pp. 459–462, Jan. 2014.

[26] T. Dogaru and C. Le, "SAR images of rooms and buildings based on FDTD computer models," *IEEE Trans. Geosci. Remote Sens.*, vol. 47, no. 5, pp. 1388–1401, May 2009.

[27] L. Li, W. Zhang, and F. Li, "A novel autofocusing approach for realtime through-wall imaging under unknown wall characteristics," *IEEE Trans. Geosci. Remote Sens.*, vol. 48, pp. 423–431, 2010.

[28] F. Ahmad, M. G. Amin, and S. A. Kassam, "Synthetic aperture beamformer for imaging through a dielectric wall," *IEEE Trans. Aerosp. Electron. Syst.*, vol. 41, no. 1, pp. 271–283, Jan. 2005.

[29] M. Dehmollaian, M. Thiel, and K. Sarabandi, "Through-the-wall imaging using differential SAR," *IEEE Trans. Geosci. Remote Sens.*, vol. 47, no. 5, pp. 1289–1296, May 2009.

[30] F. Soldovieri and R. Solimene, "Through-wall imaging via a linear inverse scattering algorithm," *IEEE Geosci. Remote Sens. Lett.*, vol. 4, no. 4, pp. 513–517, Oct. 2007.

[31] G. Gennarelli and F. Soldovieri, "A linear inverse scattering algorithm for radar imaging in multipath environments," *IEEE Geosci. Remote Sens. Lett.*, vol. 10, no. 5, pp. 1085–1089, 2013.

[32] F. Soldovieri, R. Solimene, A. Brancaccio, and R. Pierri, "Localization of the interfaces of a slab hidden behind a wall", *IEEE Trans. Geosci. Remote Sens.*, vol. 45, no. 8, pp. 2471–2482, Aug. 2007.

[33] Y.-S. Yoon and M. Amin, "High-resolution through-the-wall radar imaging using beamspace MUSIC", *IEEE Trans. Antennas Propag.*, vol. 56, no. 6, pp. 1763–1774, Jun. 2008.

[34] Q. Huang, L. Qu, B. Wu, and G. Fang, "UWB through-wall imaging based on compressive sensing", *IEEE Trans. Geosci. Remote Sens.*, vol. 48, no. 3, pp. 1408–1415, Mar. 2010.

[35] Q. Wu, Y. D. Zhang, F. Ahmad, and M. G. Amin, "Compressive-sensing based high-resolution polarimetric through-the-wall radar imaging exploiting target characteristics", *IEEE Antennas Wireless Propag. Lett.*, vol. 14, pp. 1043–1047, May 2015.

[36] G. Wang and M. G. Amin, "Imaging through unknown walls using different standoff distances," *IEEE Trans. Signal Process.*, vol. 54, no. 10, pp. 4015−4025, Oct. 2006.

[37] R. Solimene and A. Cuccaro, "Front wall clutter rejection methods in TWI," *IEEE Geosci. Remote Sens. Lett.*, vol. 11, no. 6, pp. 1158−1162, June 2014.

[38] M. Thiel and K. Sarabandi, "Advanced through-the-wall radar imaging using spectral and wall estimation techniques," *IEEE Antennas and Propagation Society International Symposium*, Toronto, ON, 2010.

[39] M. Amin and K. Sarabandi, "Special issue on remote sensing of building interior," *IEEE Trans. Geosci. Remote Sens.*, vol. 47, no. 5, pp. 1267–1268, May 2009.

[40] R. J. Burkholder and K. E. Browne, "Coherence factor enhancement of through-wall radar images," *IEEE Antennas Wireless Propag. Lett.*, vol. 9, pp. 842–845, 2010.

[41] C. A. Balanis, "Arrays: linear, planar, and circular," in *Antenna Theory: Analysis and Design*, 3rd ed., Wiley, 2005.

[42] C. A. Balanis, "Reflection and transmission," in *Advanced Engineering Electromagnetics*, 1st ed., Wiley, 1989.

[43] "EM.CUBE. ver. 15.1," EMAG Technol. Inc., Ann Arbor, MI, USA, 2015.

[44] Y. M. Pan, S. Y. Zheng, and B. J. Hu, "Wideband and low-profile omnidirectional circularly polarized patch antenna," *IEEE Trans. Antennas Propag.*, vol. 62, no. 8, pp. 4347−4351, Aug. 2014.

[45] Y. M. Pan and K. W. Leung, "Wideband omnidirectional circularly polarized dielectric resonator antenna with parasitic strips," *IEEE Trans. Antennas Propag.*, vol. 60, no. 6, pp. 2992−2997, June 2012.

[46] Y. M. Pan and K. W. Leung, "Wideband circularly polarized dielectric bird-nest antenna with conical radiation pattern," *IEEE Trans. Antennas Propag.*, vol. 61, no. 2, pp. 563−570, Feb. 2013.

[47] B. C. Park and J. H. Lee, "Omnidirectional circularly polarized antenna utilizing zeroth-order resonance of epsilon negative transmission line," *IEEE Trans. Antennas Propag.*, vol. 59, no. 7, pp. 2717−2721, July 2011.

[48] W. W. Li and K. W. Leung, "Omnidirectional circularly polarized dielectric resonator antenna with top-loaded Alford loop for pattern diversity design," *IEEE Trans. Antennas Propag.*, vol. 61, no. 8, pp. 4246−4256, Aug. 2013.

[49] B. Li and Q. Xue, "Polarization-reconfigurable omnidirectional antenna combining dipole and loop radiators," *IEEE Antennas Wireless Propag. Lett.*, vol. 12, pp. 1102−1105, 2013.

[50] W. Lin and H. Wong, "Circularly polarized conical-beam antenna with wide bandwidth and low profile," *IEEE Trans. Antennas Propag.*, vol. 62, no. 12, pp. 5974−5982, Dec. 2014.

[51] W. Lin and H. Wong, "Polarization reconfigurable wheel-shaped antenna with conical-beam radiation pattern," *IEEE Trans. Antennas Propag.*, vol. 63, no. 2, pp. 491−499, Feb. 2015.

[52] Y. Shi and J. Liu, "Wideband and low-profile omnidirectional circularly polarized antenna with slits and shorting-vias," *IEEE Antennas Wireless Propag. Lett.*, vol. 15, pp. 686−689, 2016.

[53] Y. M. Cai, S. Gao, Y. Yin, W. Li, and Q. Luo, "Compact-size low-profile wideband circularly polarized omnidirectional patch antenna with reconfigurable polarizations," *IEEE Trans. Antennas Propag.*, vol. 64, no. 5, pp. 2016−2021, May 2016.

[54] Y. Yu, Z. Shen, and S. He, "Compact omnidirectional antenna of circular polarization," *IEEE Trans. Antennas Propag.*, vol. 11, pp. 1466−1469, 2012.

[55] D. Yu, S. X. Gong, Y. T. Wan, Y. L. Yao, Y. X. Xu, and F. W. Wang, "Wideband omnidirectional circularly polarized patch antenna based on vortex slots and shorting vias," *IEEE Trans. Antennas Propag.*, vol. 62, no. 8, pp. 3970−3977, Aug. 2014.

[56] X. Cai and K. Sarabandi, "Broadband omni-directional circularly polarized antenna based on vertically and horizontally polarized elements," *IEEE International Symposium on Antennas and Propagation*, Fajardo, 2016, pp. 1793−1794.

[57] X. Quan, R. Li, and M. M. Tentzeris, "A broadband omnidirectional circularly polarized antenna," *IEEE Trans. Antennas Propag.*, vol. 61, no. 5, pp. 2363−2370, May 2013.

[58] K. L. Lau and K. M. Luk, "A wideband circularly polarized conical-beam patch antenna," *IEEE Trans. Antennas Propag.*, vol. 54, no. 5, pp. 1591−1594, May 2006.

[59] J. Wu and K. Sarabandi, "Compact omnidirectional circularly polarized antenna," *IEEE Trans. Antennas Propag.*, vol. 65, no. 4, pp. 1550−1557, Apr. 2017.

[60] N. Behdad and K. Sarabandi, "A compact antenna for ultrawide-band applications," *IEEE Trans. Antennas Propag.*, vol. 53, no. 7, pp. 2185−2192, July 2005.

[61] A. Elsherbini and K. Sarabandi, "Very low-profile top-loaded UWB coupled sectorial loops antenna," *IEEE Antennas Wireless Propag. Lett.*, vol. 10, pp. 800−803, 2011.

[62] M. Converters, C. F. Yu, and T. H. Chang, "High-performance circular TE_{21} TE_{01} and TE_{41} mode converters," *Joint 31st International Conference on Infrared Millimeter Waves and 14th International Conference on Teraherz Electronics*, Shanghai, 2006, pp. 84−84.

[63] Z. Allahgholi Pour and L. Shafai, "A novel impedance matched mode generator for excitation of the TE_{21} mode in compact dual-mode circular waveguide feeds," *IEEE Antennas Wireless Propag. Lett.*, vol. 10, pp. 427−430, 2011.

[64] W. G. Carrara, R. S. Goodman, and R. M. Majewski, *Spotlight Synthetic Aperture Radar*. Boston, MA: Artech House, 1995.

[65] A. Ribalta, "Time-domain reconstruction algorithms for FMCW-SAR," *IEEE Geosci. Remote Sens. Lett.*, vol. 8, no. 3, pp. 396–400, May 2011.

[66] G. P. Cardillo, "On the use of the gradient to determine bistatic SAR resolution", *Proc. IEEE AP-S Int. Symp.*, pp. 1032−1035, May 1990.

[67] R. W. Hamming, "Exponential approximation," in *Numerical Methods for Scientists and Engineers (Dover Books on Mathematics)*, 2nd ed., Dover Publication, New York, 1973.

[68] Y. Hua and T. K. Sarkar, "Generalized pencil-of-function method for extracting poles of an EM system from its transient response," *IEEE Trans. Antennas and Propagat.*, vol. 37, no. 2, pp. 229–234, Feb. 1989.

[69] T. K. Sarkar and O. Pereira, "Using the matrix pencil method to estimate the parameters of a sum of complex exponentials," *IEEE Antennas and Propagation Magazine*, vol. 37, no. 1, pp. 48−55, Feb. 1995.

[70] M. R. Balthasar, M. Leigsnering, and A. M. Zoubir, "Compressive classification for through-the-wall radar imaging," *20th European Signal Processing Conference (EUSIPCO)*, Bucharest, 2012, pp. 2288–2292.

[71] J. J. M. de Wit and W. L. van Rossum, "Extraction of building features from stand-off measured through-wall radar data," *IEEE J. Sel. Topics Appl. Earth Observ. Remote Sens.*, vol. 9, no. 1, pp. 149–158, Jan. 2016.

[72] W. Rossum and J. de Wit, "Overcomplete dictionary design for building feature extraction," in *Compressive Sensing for Urban Radar*, CRC Press, 2014.

[73] S. Xin, L. Biying, L. Pengfei, and Z. Zhimin, "A multiarray refocusing approach for through-the-wall imaging," *IEEE Geosci. Remote Sens. Lett.*, vol. 12, no. 4, pp. 880–884, Apr. 2015.

[74] M. Dehmollaian and K. Sarabandi, "Refocusing through building walls using synthetic aperture radar," *IEEE Trans. Geosci. Remote Sens.*, vol. 46, no. 6, pp. 1589–1599, Jun. 2008.

[75] D. J. Daniels, "A review of landmine detection using GPR," *European Radar Conference*, Amsterdam, 2008, pp. 280−283.

[76] W. Uddin, "An overview of GPR applications for evaluation of pavement thickness and

cracking," *Proceedings of the 15th International Conference on Ground Penetrating Radar*, Brussels, 2014, pp. 925−930.

[77] L. Crocco and V. Ferrara, "A review on ground penetrating radar technology for the detection of buried or trapped victims," *International Conference on Collaboration Technologies and Systems (CTS)*, Minneapolis, MN, 2014, pp. 535−540.

[78] *Ground-Penetrating Radar Soil Suitability Maps*, United States Department of Agriculture. [Online]. Available: https://www.nrcs.usda.gov/wps/portal/nrcs/detail/soils/survey/geo/?cid= nrcs 142p2_053622.

[79] M. G. Fernandez, Y. A. Lopez, B. G. Valdes, Y. R. Vaqueiro, F. L. Andres, and A. P. Garcia "Synthetic aperture radar imaging system for landmine detection using a ground penetrating radar on board a unmanned aerial vehicle," *IEEE Access*, vol. 6, pp. 45100−45112, 2018.

[80] C. J. Li and H. Ling, "High-resolution, downward-looking radar imaging using a small consumer drone," *IEEE International Symposium on Antennas and Propagation*, Fajardo, 2016, pp. 2037−2038.

[81] K. Gu, G. Wang, and J. Li, "Migration based SAR imaging for ground penetrating radar systems," *IEE Proceedings - Radar, Sonar and Navigation*, vol. 151, no. 5, pp. 317−325, 2004.

[82] A. C. Gurbuz, J. H. McClellan, and W. R. Scott, "A compressive sensing data acquisition and imaging method for stepped frequency GPRs," *IEEE Trans. Signal Process.*, vol. 57, no. 7, pp. 2640−2650, July 2009.

[83] W. Zhang and A. Hoorfar, "A generalized approach for SAR and MIMO radar imaging of building interior targets with compressive sensing," *IEEE Antennas Wireless Propag. Lett.*, vol. 14, pp. 1052−1055, 2015.

[84] W. Zhang and A. Hoorfar, "MIMO Ground Penetrating Radar Imaging Through Multilayered Subsurface Using Total Variation Minimization," *IEEE Trans. Geosci. Remote Sens.*, vol. 57, no. 4, pp. 2107−2115, Apr. 2019.

[85] B. Wu, Y. Ji, and G. Fang, "Analysis of GPR UWB half-ellipse antennas with different heights of backed cavity above ground," *IEEE Antennas Wireless Propag. Lett.*, vol. 9, pp. 130–133, 2010.

[86] S. Qu, J. Li, Q. Xue, and C. H. Chan, "Wideband cavity-backed bowtie antenna with pattern improvement," *IEEE Trans. Antennas Propag.*, vol. 56, no. 12, pp. 3850–3854, Dec. 2008.

[87] S. Qu, J. Li, Q. Xue, C. H. Chan, and S. Li, "Wideband and Unidirectional Cavity-Backed Folded Triangular Bowtie Antenna," *IEEE Trans. Antennas Propag.*, vol. 57, no. 4, pp. 1259–1263, Apr. 2009.

[88] M. Serhir and D. Lesselier, "Wideband reflector-backed folded bowtie antenna for ground penetrating radar," *IEEE Trans. Antennas Propag.*, vol. 66, no. 3, pp. 1056–1063, Mar. 2018.

[89] A. Ahmed, Y. Zhang, D. Burns, D. Huston, and T. Xia, "Design of UWB antenna for air-coupled impulse ground-penetrating radar," *IEEE Geosci. Remote Sens. Lett.*, vol. 13, no. 1, pp. 92–96, Jan. 2016.

[90] J. Shao, G. Fang, J. Fan, Y. Ji, and H. Yin, "TEM horn antenna loaded with absorbing material for GPR applications," *IEEE Antennas Wireless Propag. Lett.*, vol. 13, pp. 523–527, 2014.

[91] A. Elsherbini and K. Sarabandi, "ENVELOP antenna: a class of very low profile UWB directive antennas for radar and communication diversity applications," *IEEE Trans. Antennas Propag.*, vol. 61, no. 3, pp. 1055–1062, Mar. 2013.

[92] F. T. Ulaby and D. G. Long, *Microwave Radar and Radiometric Remote Sensing,* Ann Arbor, USA: University of Michigan Press, 2014.

[93] N. R. Peplinski, F. T. Ulaby, and M. C. Dobson, "Dielectric properties of soils in the 0.3-1.3-GHz range," *IEEE Trans. Geosci. Remote Sens.*, vol. 33, no. 3, pp. 803–807, May 1995.

[94] N. R. Peplinski, F. T. Ulaby, and M. C. Dobson, "Corrections to "dielectric properties of soils in the 0.3-1.3-GHz range"," *IEEE Trans. Geosci. Remote Sens.*, vol. 33, no. 6, pp. 1340, Nov. 1995.